universität innsbruck

Investigation of magnetic solitons in binary dipolar Bose-Einstein condensates

Rene Röhrs, 11807966
Innsbruck, 7. April 2025

Master's thesis

submitted to the University of Innsbruck, Faculty of Mathematics, Computer Science and Physics in partial fulfilment of the requirements for the academic degree

Master of Science

Master's Programme Physics
Supervisor: Dr. Russell Bisset
Institute for Experimental Physics
Faculty of Mathematics, Computer Science and Physics

Abstract

In this thesis, we investigate polarised solitary waves, known as magnetic solitons and dark-antidark solitons, in binary (two-component) Bose-Einstein condensates in the miscible phase. These solitons have been recently realised in experiments and are predicted to form bound states. We calculate the interaction potentials between magnetic solitons with the same and opposite polarisation, uncovering the mechanisms underlying bound state formation. By considering two superimposed counter-propagating magnetic solitons with opposite polarisation, we analytically calculate the dissociation energy of the bound states and find good agreement with full numerical simulations. Furthermore, we show that the oscillation period of bound states depends on the maximum soliton separation. We subsequently extend these results to dark-antidark solitons. For binary dipolar Bose-Einstein condensates, we derive the dispersion relation of elementary excitations and find that, in the presence of a spin-roton, spin-density modulations form around dark-antidark solitons. These modulations lead to additional local maxima and minima in the inter-soliton potentials, enabling the formation of additional bound state regions. Additionally, we compare the collision characteristics of magnetic solitons in non-dipolar systems with dark-antidark solitons in dipolar–nondipolar condensate mixtures and explore the collisions between bound states in the non-dipolar case.

Acknowledgements

I would like to thank my supervisor Dr. Russell Bisset for the great supervision and for providing the opportunity to attend the Dipolar Quantum Matter conference in Durham. Thanks to Dr. Natalia Masalaeva, Ashwath Madhusudan, Leonardo Bellinato Giacomelli, Elena Poli, Dr. Pramodh Senarath Yapa, Dr. Thomas Bland for helpful and fruitful discussions.
Special thanks to my parents and friends in Innsbruck for always being supportive.

Contents

1. Introduction

Solitons are localised excitations that move through a medium without dispersing. They retain their shape over long distances and emerge unscathed from collisions with other solitons, except for a shift in position and phase. The first recorded observation of a soliton was made by John Scott Russell in 1834, when he observed a wave travelling upstream along a water channel while maintaining its shape over a long distance [1].
Solitons emerge in non-linear systems, where nonlinearity balances the dispersive effects. Zabusky and Kruskal were the first to numerically simulate solitons in the context of the Korteweg–de Vries (KdV) equation, demonstrating their particle-like behaviour [2]. Shortly after, Gardner et. al. showed that solitons emerge from the same equation as an exact solution via the inverse scattering transform method [3]. Systems described by non-linear partial differential equations for which the inverse scattering transform is applicable are often referred to as integrable systems and yield true solitons as exact solutions [4]. True solitons are theoretically well understood and have been experimentally realised in many different research areas, including optical fibres [5–7] and some many-body systems, such as Bose-Einstein condensates [8].
A Bose-Einstein condensate (BEC) is an ultracold state of matter that exhibits quantum mechanical phenomena on a macroscopic scale. A BEC can form when a dilute Bose gas is cooled to temperatures of a few hundred nanokelvin. At such low temperatures a second-order phase transition occurs, and the bosons begin to macroscopically occupy the same single-particle ground state (see, *e.g.*, Ref. [9]). BECs are highly controllable and are widely used to study fundamental concepts in physics, including condensed matter physics [9], quantum statistics [10] and cosmology [11, 12], with controllable temperature effects.
Since interacting many-body systems are notoriously difficult to solve exactly, they are often described using mean-field approximations. The Gross-Pitaevskii equation (GPE), a non-linear Schrödinger equation, is a standard mean-field description for condensates and assumes low temperature, where a significant fraction of the particles occupy the same condensate state [13]. The particles can then be described by an order parameter, a classical field obeying the GPE instead of the full many-body description. This is analogues to the description of the electro-magnetic field obeying the Maxwell equations for many photons in the same quantum state. The GPE provides an accurate description for a large dilute BEC with weak interactions at low temperatures.
The GPE is non-linear and thus supports many exotic excitations, such as quantised vortices [14], solitonic vortices [15, 16], dark solitons [8], and bright solitons [17]. True solitons are only supported in the homogeneous, quasi-one-dimensional (quasi-1D) limit,

where the GPE reduces to the quasi-one-dimensional non-linear Schrödinger equation. Beyond the quasi-1D limit, the integrability of the GPE breaks down, and true solitons are no longer supported. Nonetheless, the GPE supports solitary wave solutions with properties similar to those of dark or bright solitons. However, the higher dimensionality may allow these solitary waves to, *e.g.*, form snake instabilities due to radial excitations, causing them to decay into vortices [18].
Another way to break integrability is to add long-range interactions, such as dipole-dipole interactions (DDIs), in addition to the local contact interaction. Dipolar interactions give rise to fundamentally novel phenomena, including a roton-maxon dispersion relation [19–24], liquid-like droplets [25–30] and supersolidity [31–33]. In a quasi-1D BEC with DDIs, solitons can form density modulations around their centre, which have been predicted to give rise to bound states between two black solitons [34, 35] and two bright solitons [36, 37].
Since integrability breaks down in the presence of DDIs, these solitary waves are not true solitons and experience radiative loss in the form of phonon and roton excitations. Nonetheless, the literature tends to name them solitons regardless, since, far from the roton instability, the radiative loss is negligible and they behave similar to dark or bright solitons.
After the experimental realisation of BECs in 1995 by Cornell, Wieman [38], and Ketterle [39], multi-component BECs with homonuclear mixtures [40] and heteronuclear mixtures [41–44] were quick to follow. The inter-component interactions introduce additional degrees of freedom, giving rise to a range of phenomena, including phase separation [45], skyrmions [46], vortex-vortex pairs [47] and vector solitons [48, 49]. Intriguingly, for vector solitons, there have been interesting bound states predicted, including breathing patterns of dark-bright solitons [50], kink-antikink configurations [51], beating of dark-dark solitons [52]) and Flemish strings for spin-1 BECs [53]. The realisation of these bound states is now within reach, as demonstrated by the recent experimental production of vector solitons, such as dark-bright solitons [54], dark-antidark solitons [55–58] and magnetic solitons [59, 60].
Two-component (binary) BECs are only integrable in the case of equal intra-component and inter-component interactions (commonly referred to as the Manakov regime [61]), which means that only in this regime are vector solitons true solitons. However, outside this regime, vector solitons still behave very similarly to true solitons.

1.1. Focus of this thesis

In this thesis, we explore magnetic soliton bound states in non-dipolar binary BECs and extend the analysis to dark-antidark soliton bound states. Later, we consider binary dipolar BECs, where we predict additional types of soliton-soliton bound states.
Through numerical calculations, we evaluate the interaction potentials between solitons with the same or opposite polarisation, demonstrating repulsive and attractive behaviour respectively, shedding light on the mechanism behind the formation of bound states. By considering two superimposed counter-propagating magnetic solitons with opposite polarisation, we analytically determine the bound state dissociation energy and can confirm

our findings with full numerical simulations. For binary dipolar BECs, we uncover a connection between the spin roton in the dispersion relation and periodic modulations in the soliton-soliton interaction potential, which enable the formation of at least three distinct bound state regions. Finally, we study soliton collisions, observing that in the absence of dipolar interactions, slow-moving solitons with the same polarisation bounce off one another, while those with opposite polarisation pass through one another. However, in the presence of dipolar interactions, solitons consistently bounce, independent of their polarisation.

1.2. Thesis outline

This thesis is structured as follows.

In Chapter 2, we review preliminary concepts for studying magnetic solitons in both non-dipolar and dipolar BECs. We begin by reviewing Bose-Einstein condensation, then introduce the theoretical description of dilute condensates, followed by an extension to binary condensates. We then consider the fundamentals of dark solitons in single-component BECs and vector solitons in binary BECs, reviewing the theory of dark-bright and dark-antidark solitons, with a particular focus on magnetic solitons, a special case of dark-antidark solitons that arises near the transition to the immiscible regime. Subsequently, we review the description of dilute BECs in dipolar condensates and then dark solitons in single-component dipolar BECs.

In Chapter 3, we review recent research developments that motivate this thesis. We examine relevant experiments that create dark-antidark and magnetic solitons, and consider theoretical predictions of bound states between these solitons. We also review theoretical work predicting bound states between dark solitons in single-component dipolar BECs. By combining these two concepts of bound-state formation, we motivate our investigation presented in Chapter 6.

In Chapter 4, we outline the derivation of the mean-field description, the GPE, for elongated binary dipolar condensates. We review the derivation of the coupled 3D GPEs from the Lagrangian density. Subsequently, we reduce the coupled GPEs to a quasi-1D description by assuming cigar-shaped confinement of both components.

In Chapter 5, we examine the numerical methods used to solve the coupled GPEs. We convert the coupled GPEs to their dimensionless form, and then describe the numerical solver. Next, we outline the imprinting methods used to generate the initial states of two dark-antidark solitons or magnetic solitons.

In Chapter 6, we present the main results of this thesis. We demonstrate that bound states between magnetic solitons in binary BECs are possible if the solitons have opposite polarisation. We then calculate the inter-soliton potential, which explains the dynamics between the solitons. Next, we analytically calculate the dissociation energy of the bound states and consider the oscillation period, which depends on the maximum soliton separation of the bound states. We extend these considerations to the general case of dark-antidark

solitons. Furthermore, we consider dark-antidark solitons in binary dipolar BECs, and derive the Bogoliubov dispersion relations. Next, we find that the presence of a spin roton in the dispersion relation causes density modulations around the centre of the soliton and leads to the formation of additional bound states. We again calculate the inter-soliton potential to understand the forces acting between the solitons. Finally, we explore collisions between dark-antidark solitons. We begin by considering collisions between magnetic solitons in the non-dipolar case and also consider collisions between bound states. We then examine the dipolar case, where the collisions differ fundamentally.

In Chapter 7, we summarise the key findings of this thesis. We then provide an outlook for future research that could expand these findings and support their realisation in experiments.

2. Foundations

In the following, we first introduce the phenomena of Bose-Einstein condensation (BEC) and then develop the Hamiltonian description of a dilute two-component condensate with short-ranged interactions. We do this by considering the ideal Bose gas, introducing contact interactions and then extending the formalism to a two-component system. We then consider solitons in BECs. We discuss the theoretical description of dark solitons and multi-component solitons, called vector solitons. Later, we introduce dipole-dipole interactions (DDI), which, along with contact interactions, govern the interactions between particles in dipolar BECs. Finally, we consider dark solitons in dipolar BECs.

2.1. Bose-Einstein condensation (BEC)

A Bose-Einstein condensate is an exotic state of matter with macroscopic quantum mechanical properties, where a macroscopic number of particles occupy the same single-particle state. The theoretical description was developed in the early 1920's, when Satyendra Nath Bose made an *error* in one of his lectures, trying to show his students inconsistencies at the time between theory and experimental results on the photoelectric effect and the ultraviolet catastrophe. This *error*, which introduces the indistinguishability of particles, lead him to show instead that theory and experimental results were in agreement. After careful considerations Bose tried to publish his findings on quantum statistics of phonons, which found strong resistance until he sent them to Albert Einstein, who published them on his behalf [62]. In subsequent papers, Einstein extended Bose's concept of photon indistinguishability to matter particles, which are now known as bosons. This resulted in the theory we now refer to as Bose-Einstein statistics.
A major result of Bose-Einstein statistics is the Bose-Einstein distribution [9],

$$N_i = \frac{1}{e^{(E_i-\mu)/k_BT} - 1}, \tag{2.1}$$

predicting the mean number of bosons N_i occupying the i-th single-particle state with an energy E_i, where μ is the chemical potential, k_B is the Boltzmann constant and T is the temperature. The total number of particles N is then the sum over all single-particle states

$$N = N_0 + \sum_{i\neq 1} N_i = N_0 + N_T, \tag{2.2}$$

where N_0 is the occupation number of the lowest energy state and $N_T = \sum_{i\neq 1} N_i$ is known as the occupation number of the thermal cloud. According to Eq. (2.1), μ must be smaller

than the lowest energy state E_0, meaning that for a given T, the thermal population N_T saturates at a finite value $N_C(\mu = E_0, T)$. Thus, increasing the total particle number N, which increases μ, beyond N_C while keeping T fixed, places all excess particles $N - N_C$ into the lowest energy state, also known as the condensate state. As $\mu \to E_0$, the condensate state exhibits macroscopic occupation ($N_0 \sim N$) and a second-order phase transition occurs. This is referred to as the Bose-Einstein condensation (BEC) phase [9]. This can also be achieved by reducing T, while keeping N fixed. For lower T, the thermal cloud saturates at a lower particle number N_C. Accordingly, for a given N, there exists a temperature T_C for which $N_C(\mu = E_0, T_C) = N$. For $T < T_C$, the system enters the BEC phase.
An inherent feature of the BEC transition, like other second-order phase transitions, is the presence of an order parameter, resulting from the formation of a off-diagonal long-ranged order (LRO) from an unordered thermal state. Phase coherence throughout the condensate causes the LRO and can be understood by considering the de-Broglie wavelength of a particle given by [63]

$$\lambda = \frac{h}{\sqrt{2\pi m k_B T}}, \tag{2.3}$$

where m is the mass of the particle and $\hbar$ is the Planck constant. According to Eq. (2.3), the de-Broglie wavelength of the particles in a Bose gas increases as the temperature decreases. At the critical temperature T_C, λ becomes comparable to the average separation between the particles $d = (N/V)^{1/3} = n^{1/3}$ and the single-particle wavefunctions start to overlap, resulting in quantum degeneracy. For Bosons, a macroscopic matter wave begins to form which is described by the order parameter [9]

$$\Psi_0(\mathbf{r}, t) = |\Psi_0(\mathbf{r}, t)| e^{i\phi(\mathbf{r},t)}, \tag{2.4}$$

where $\phi(\mathbf{r}, t)$ represents the phase of the condensate.
After the theoretical prediction of BECs in 1925, it took another 70 years to realise this exotic state of matter in dilute gases of rubidium [38], lithium [64] and sodium [39]. E. A. Cornell, C. E. Wieman, and W. Ketterle were awarded the 2001 Nobel Prize in Physics for their pioneering work on Bose-Einstein condensation. The major hurdle was to cool down the atoms to nanokelvin temperatures, which was only possible after the development of laser cooling [65–67] and evaporative cooling methods [68–70]. The development of laser cooling and trapping methods led to S. Chu, C. Cohen-Tannoudji, and W. D. Phillips being awarded the 1997 Nobel Prize in Physics. The realisation of BECs provided new opportunities to study many-body states and quantum degeneracy, in contrast to previously observed phenomena such as superconductivity in metals and superfluidity in helium, which offered limited insights due to the strong interactions and lack of tunability involved.

2.2. Short-range interactions in dilute binary condensates

In this section, we introduce the description of short-range interactions in dilute binary (two-component) condensates, forming the foundation for studying vector solitons in Sec. 2.3.2.

For a more detailed review, see, *e.g.*, Ref. [9]. We begin by outlining the basic formalism of second quantisation for many-body systems by considering single-component ideal Bose gases. Building on this, we incorporate short-range interactions in dilute condensates, neglecting three-body and higher-order collisions and approximating two-body contact interactions with a soft pseudo-potential. Finally, we extend the description to a dilute two-component condensate.

2.2.1. Ideal Bose gas

The theory of Bose and Einstein predicted the condensation of an ideal Bose gas without any interactions. In this simple model, the many-body Hamiltonian of N bosons is the sum of N single particle Hamiltonians $\hat{H}_{sp} = -\frac{\hbar^2\nabla^2}{2m} + V(\mathbf{r}, t)$, where $V(\mathbf{r}, t)$ is the external potential, and takes the form

$$\hat{H} = \int \hat{\Psi}^\dagger(\mathbf{r}) \hat{H}_{\mathrm{sp}} \hat{\Psi}(\mathbf{r}) d\mathbf{r} \tag{2.5}$$

in second quantisation. In this formalism, the system is described by the field operator

$$\hat{\Psi}(\mathbf{r}) = \sum_j \hat{a}_j \Phi_j(\mathbf{r}), \tag{2.6}$$

where ϕ_j are the wavefunctions of single-particle states, and $\hat{a}_i$ and $\hat{a}_i^\dagger$ are the annihilation and creation operators of a particle in state j, respectively. The field operator obeys the following commutation relations

$$[\hat{\Psi}(\mathbf{r}), \hat{\Psi}(\mathbf{r}')^\dagger] = \delta(\mathbf{r} - \mathbf{r}'), \quad [\hat{\Psi}(\mathbf{r}), \hat{\Psi}(\mathbf{r}')] = [\hat{\Psi}^\dagger(\mathbf{r}), \hat{\Psi}(\mathbf{r}')^\dagger] = 0, \tag{2.7}$$

where $\delta(\mathbf{r} - \mathbf{r}')$ is the Dirac delta function. These relations follow directly from the commutation relations of the annihilation and creation operators

$$[\hat{a}_i, \hat{a}_j^\dagger] = \delta_{ij}, \quad [\hat{a}_i, \hat{a}_j] = [\hat{a}_i^\dagger, \hat{a}_j^\dagger] = 0, \tag{2.8}$$

where δ_{ij} is the Kronecker delta function.

2.2.2. Contact interactions in the dilute gas limit

This simple model of an ideal Bose gas (see Sec. 2.2.1) provides limited insight into experimental realisations of BECs. In this subsection, we incorporate two-body contact interactions, which offer a highly successful theoretical framework for describing condensates composed of non-dipolar, dilute bosons [13].

The first correction to the ideal Bose gas is typically the inclusion of two-body interactions, which provides a description of a weakly interacting Bose gas. Considering only two-body interactions and neglecting simultaneous three- or higher-order particle interactions requires that the diluteness condition

$$r_0 \ll d, \tag{2.9}$$

is fulfilled, where $d = n^{1/3}$ is the average separation between the atoms in the three-dimensional case and r_0 is the range of interaction forces. The dilute Bose gas can be described by the Hamiltonian in second quantisation

$$\hat{H} = \int \hat{\Psi}^\dagger(\mathbf{r})\hat{H}_{\text{sp}}\hat{\Psi}(\mathbf{r})d\mathbf{r} + \frac{1}{2}\int \hat{\Psi}(\mathbf{r}')^\dagger\hat{\Psi}^\dagger(\mathbf{r})U(\mathbf{r}'-\mathbf{r})\hat{\Psi}(\mathbf{r}')\hat{\Psi}(\mathbf{r})d\mathbf{r}'d\mathbf{r}, \tag{2.10}$$

where $U(\mathbf{r}'-\mathbf{r})$ is the two-body interaction potential.
The Hamiltonian (2.10) is difficult to solve for the true inter-atomic potential $U(\mathbf{r}'-\mathbf{r})$, which diverges for $|\mathbf{r}'-\mathbf{r}| \to 0$. In the late 1940's Bogoliubov developed the model of weakly-interacting Bose gases, introducing approximations to solve this Hamiltonian [71]. In the weakly interacting low temperature case, only low momenta scattering occurs and $|\mathbf{p}|r \ll \hbar$ holds, where $\mathbf{p}$ is the momentum. We can then substitute $U(\mathbf{r})$ with an effective soft potential $U_{\text{eff}}(\mathbf{r})$, which gives identical low momentum scattering properties. Further, we retain only the $p = 0$ term in the Fourier transform of this effective potential. The two-body interaction potential is then given by the pseudo-potential

$$U_s(\mathbf{r}) = g_s\delta(\mathbf{r}). \tag{2.11}$$

The constant g_s is referred to as the interaction coupling constant and can be determined, at long wavelengths and within the first-order Born approximation, as [72]

$$g_s = \frac{4\pi\hbar^2 a_s}{m}, \tag{2.12}$$

where a_s is the s-wave scattering length. Finally, the Hamiltonian (2.10) takes the form

$$\hat{H} = \int d\mathbf{r}\hat{\Psi}^\dagger(\mathbf{r})\left[-\frac{\hbar^2\nabla^2}{2m} + V(\mathbf{r},t) + \frac{g_s\hat{\Psi}^\dagger(\mathbf{r})\hat{\Psi}(\mathbf{r})}{2}\right]\hat{\Psi}(\mathbf{r}). \tag{2.13}$$

The Hamiltonian (2.13) provides an accurate description of three-dimensional Bose gases and supports repulsive $a_s > 0$ and attractive $a_s < 0$ contact interactions. Condensates with repulsive contact interactions are stable and support dark solitons, localised density dips, as metastable solutions. In contrast, condensates with weak attractive interactions are metastable and support bright solitons, which are stable density peaks surrounded by zero density [73, 74]. For sufficiently strong attractive interactions, condensates are unstable and undergo collapse [64, 75].
We now consider the Hamiltonian (2.13) for a weakly repulsive interacting Bose gas that is uniformly distributed within a volume V. Such a system can be constructed by applying the creation operator $\hat{a}^\dagger_{\mathbf{p}}$ a total of N times on the vacuum, generating N particles with momenta $\mathbf{p}$. The corresponding field operators are given by

$$\hat{\Psi}(\mathbf{r}) = \sum_{\mathbf{p}} \hat{a}_{\mathbf{p}}\frac{1}{\sqrt{V}}e^{i\mathbf{p}\cdot\mathbf{r}/\hbar}, \tag{2.14}$$

and

$$\hat{\Psi}^\dagger(\mathbf{r}) = \sum_{\mathbf{p}} \hat{a}^\dagger_{\mathbf{p}}\frac{1}{\sqrt{V}}e^{-i\mathbf{p}\cdot\mathbf{r}/\hbar}. \tag{2.15}$$

By inserting Eq. (2.14) and (2.15) into Eq. (2.13), and retaining terms up to second order in particle operators with $\mathbf{p} \neq 0$, while introducing the average particle density $n_0^{3D} = N/V$ and applying the Bogoliubov transformation, we obtain (see, *e.g.*, Ref. [76, 77])

$$\hat{H} = g\frac{N^2}{2V}\left[1 + \frac{128}{15\sqrt{\pi}}(a^3 n_0^{3D})^{\frac{1}{2}}\right] + \sum_{\mathbf{p}} \epsilon(p)\hat{b}_{\mathbf{p}}^{\dagger}\hat{b}_{\mathbf{p}}, \tag{2.16}$$

where we introduce the Bogoliubov dispersion relation

$$\varepsilon(p) = \left[c^2 p^2 + \left(\frac{p^2}{2m}\right)^2\right]^{1/2}, \tag{2.17}$$

with the speed of sound $c = \sqrt{g n_0^{3D}/m}$.
The first term in Eq. (2.16) gives the ground state energy of the system, and the second term describes independent elementary excitations, created and annihilated by $\hat{b}_{\mathbf{p}}^{\dagger}$ and $\hat{b}_{\mathbf{p}}$, respectively [71]. Figure 2.1 shows the dispersion relation of these excitations, exhibiting phonon-like behaviour at low momenta,

$$\varepsilon(p) \approx cp, \tag{2.18}$$

and free-particle character at high momenta,

$$\varepsilon(p) \approx \frac{p^2}{2m} + mc^2. \tag{2.19}$$

Equations (2.18) and (2.19) can be obtained by performing a Taylor expansion to Eq. (2.17) in the limits of low momenta, $p \ll mc_s$, and large momenta, $p \gg mc_s$, respectively.

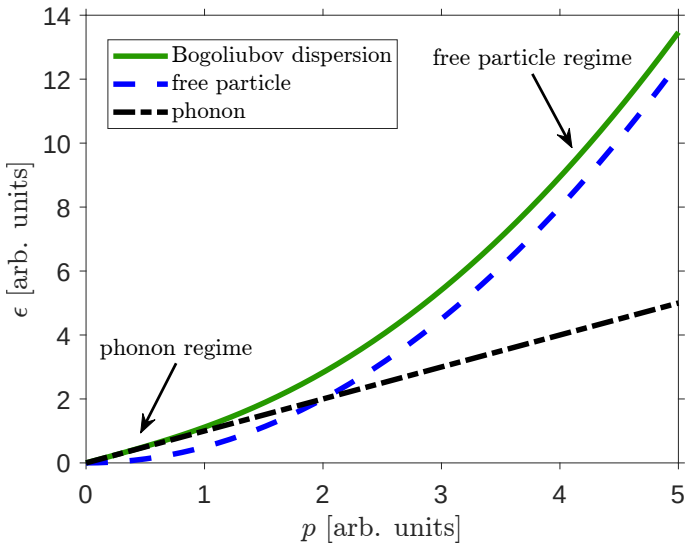

Figure 2.1.: Bogoliubov dispersion relation for elementary excitations in a weakly interacting Bose gas [see Eq. (2.17)], for phonons [see Eq. (2.18)] and for free particles [see first term in Eq. (2.19)]. At $p \approx \sqrt{2}$, the BEC undergoes a crossover from the phonon regime to the free particle regime. The axes are in arbitrary units.

2.2.3. Dilute binary BECs

A binary (two-component) BECs consists of two distinct condensates that interact with each other. The system can consist of a mixture of two different atom species or of the same atom species in different spin states. The field operators $\hat{\Psi}_1(\mathbf{r})$ and $\hat{\Psi}_2(\mathbf{r})$ describe the first and second component, respectively. In the dilute limit, the contact interactions can be described by a 2×2 matrix, with the diagonal terms a_{11} and a_{22} describing the intra-component scattering lengths of the first and second component, respectively. The off-diagonal terms a_{12} and a_{21} describe the inter-component interactions. We assume $a_{12} = a_{21}$ in the entirety of this thesis. We find the interaction coupling constant to be

$$g = \begin{pmatrix} g_{11} & g_{12} \\ g_{12} & g_{22} \end{pmatrix} = \frac{4\pi\hbar^2}{m} \begin{pmatrix} a_{11} & a_{12} \\ a_{12} & a_{22} \end{pmatrix}. \tag{2.20}$$

The Hamiltonian is given by

$$\hat{H} = \hat{H}_1 + \hat{H}_2, \tag{2.21}$$

where

$$\hat{H}_i = \int d\mathbf{r} \hat{\Psi}_i^\dagger(\mathbf{r}) \left[-\frac{\hbar^2\nabla^2}{2m} + V(\mathbf{r}, t) + \sum_{j=1}^{2} \frac{g_{ij}\hat{\Psi}_j^\dagger(\mathbf{r})\hat{\Psi}_j(\mathbf{r})}{2} \right] \hat{\Psi}_i(\mathbf{r}). \tag{2.22}$$

In the following, we focus on systems with repulsive contact interactions, where magnetic solitons and dark-antidark solitons, the primary subjects of this thesis, are supported. For repulsive intra-component contact interactions g_{11}, $g_{22} > 0$, there exist two regimes depending on g_{12}. The first regime is called the miscible regime, where

$$-\sqrt{g_{11}g_{22}} < g_{12} < \sqrt{g_{11}g_{22}} \tag{2.23}$$

holds. In this regime, the magnitude of the inter-component interactions are smaller than the intra-component interactions, and the condensates are able to coexist in the same spatial region. In the regime with $g_{12} > \sqrt{g_{11}g_{22}}$, the condensates are unable to mix and instead phase-separate into distinct regions. This is called the immiscible regime.

2.3. Solitons in BECs

Solitons are solitary wave excitations in the form of localised excitations moving through a medium without dispersing. Since their realisation in fibre optics in 1987 by Emplit et al. [78], solitons have been the subject of extensive research. A particularly intriguing area of study involves vector solitons, where solitons form in two-component systems (or, in optics, in two polarisations). Vector solitons were initially studied and experimentally observed in the context of fibre optics, including the study of bright-bright solitons [79], dark-dark solitons [80] and dark-bright solitons [81, 82], where the solitons in different polarisations are coupled incoherently. Extending the study of solitons beyond optics, BECs provide a rich platform for investigating their dynamics in superfluids.
In this section, we focus on solitons in BECs with repulsive contact interactions. We begin

by discussing dark solitons in single-component condensates, before introducing vector solitons in binary condensates. In particular, we examine dark-bright, dark-antidark, and magnetic solitons.

2.3.1. Dark solitons

This subsection reviews some general features of dark solitons in single-component condensates. For more information, the interested reader is referred to, *e.g.*, Ref. [9].
Dark solitons are caused by a localised phase gradient and manifest as localised density dips in a homogeneous background. They are divided into black (velocity $v = 0$) and grey solitons ($0 < v/c < 1$). Examples of a black and two grey solitons are shown in Fig. 2.2. The blue dotted line shows a black soliton, which has a phase-jump of π at $x = 0$. At this point the kinetic energy per particle $E_{kin}/N = \infty$ and the density has to be $n(0) = 0$. Thus, the black soliton cuts the BEC in half and no particle flow between the two regions occurs. Grey solitons result from a phase difference $\Delta\phi < \pi$, and the density dip does not reach zero. The finite phase change induces a flow of the superfluid in the direction from smaller to larger phase[1], which is from right to left for the grey solitons marked by the yellow and red dashed lines in Fig. 2.2. The superfluid flow causes the soliton to move to the right, similar to an electron-hole in a conductor moving opposite to the current direction. Since the density trough is deeper for a steeper phase gradient, less superfluid can flow beneath it, causing the soliton to move more slowly.

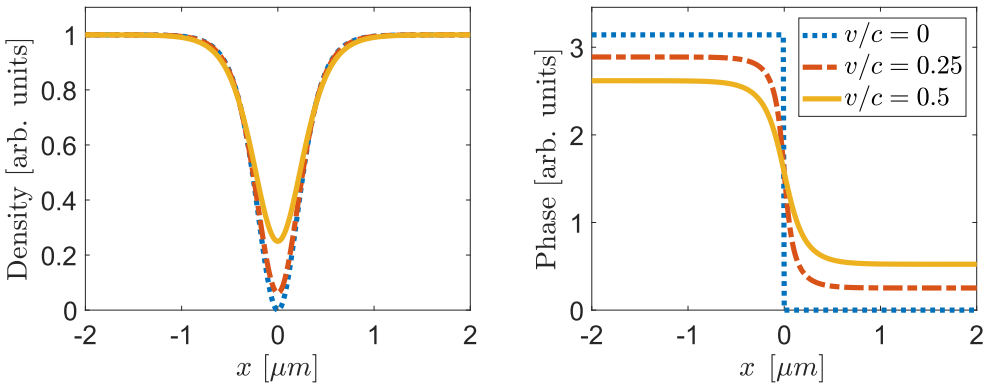

Figure 2.2.: Density (left) and phase (right) distributions of dark solitons with various velocities (see legend), plotted using Eq. (2.25). The density is normalised to the background density n_0.

Dark solitons are stable in quasi-1D BECs. In the mean-field description, such a system is governed by the quasi-1D Gross-Pitaevskii equation (GPE)

$$i\hbar\partial_t\psi(x,t) = \left(-\frac{\hbar^2}{2m}\partial_x^2 + \frac{1}{2}m\omega_x^2x^2 + \frac{g_s|\psi(x,t)|^2}{2\pi l^2}\right)\psi(x,t), \tag{2.24}$$

where $\psi(x,t)$ is the 1D wavefunction of the condensate, $l = \sqrt{\frac{\hbar}{m_0\omega_\rho}}$ is the characteristic length of the radial trap, and ω_x is the frequency of the harmonic trap in x direction.

[1]The superfluid velocity relates to the phase as $\mathbf{v}_s = \frac{\hbar}{m}\nabla\phi$.

Note that this form of interactions is only valid in the regime where scattering is three dimensional, *i.e.*, $a_s \ll l$. The frequency ω_ρ determines the radial confinement of the condensate and is much larger than ω_x for a quasi-1D geometry. The GPE (2.24) is integrable and supports analytic solutions of dark solitons

$$\psi(x-vt) = \sqrt{n_0}\left(i\frac{v}{c} + \sqrt{1-\frac{v^2}{c^2}}\tanh\left[\frac{x-vt}{\sqrt{2}\xi}\sqrt{1-\frac{v^2}{c^2}}\right]\right), \tag{2.25}$$

where v is the velocity of the soliton and $\xi = \hbar/\sqrt{2mgn_0}$ is the healing length, which characterises the length scale over which the condensate recovers from a perturbation. The background density $n_0 = N/L$ represents the average particle number per unit length L. The total phase change $\Delta\phi$ across the condensate is

$$\Delta\phi = \phi(\infty) - \phi(-\infty) = -2\arccos\frac{v}{c}, \tag{2.26}$$

and the density profile of the soliton is

$$n(x-vt) = |\psi(x-vt)|^2 = n_0 - \delta n(x-vt) \tag{2.27}$$

with

$$\delta n(x-vt) = n_0\left(1-\frac{v^2}{c^2}\right)\cosh^{-2}\left(\frac{x-vt}{\sqrt{2}\xi}\sqrt{1-\frac{v^2}{c^2}}\right). \tag{2.28}$$

We can see that the point with the lowest density is at the centre of the soliton with $n(0) = n_0 v^2/c^2$ and the width is proportional to $\xi/\sqrt{1-v^2/c^2}$.
Finally, we can consider the energy of a single soliton

$$E_{\mathrm{ds}}(v) = \frac{4}{3}\hbar c n\left(1-\frac{v^2}{c^2}\right)^{3/2}, \tag{2.29}$$

which underlines the character of solitons as quasiparticles with negative effective mass, as the black soliton has the largest energy and dark solitons accelerate when losing energy.

2.3.2. Vector solitons

In multi-component interacting BECs, a soliton excitation can manifest in all components, even if the initial excitation originates in only one component. These multi-component excitations are known as vector solitons. Depending on the nature of the interactions, vector solitons can take on various forms within each component, leading to additional degrees of freedom, *e.g.*, the spin density $n_s = n_1 - n_2$ for two-component systems. This can lead to interesting new phenomena, including stability against transverse decay [49, 54] and the formation of bound states [51, 53, 55, 56, 60, 83, 84]. Recent research on vector solitons in binary BECs has attracted growing attention, marked by the experimental realisation of dark-bright solitons [54], dark-antidark solitons [52, 57] and magnetic solitons [59, 60]. This subsection reviews some general features of these vector solitons in binary condensates.

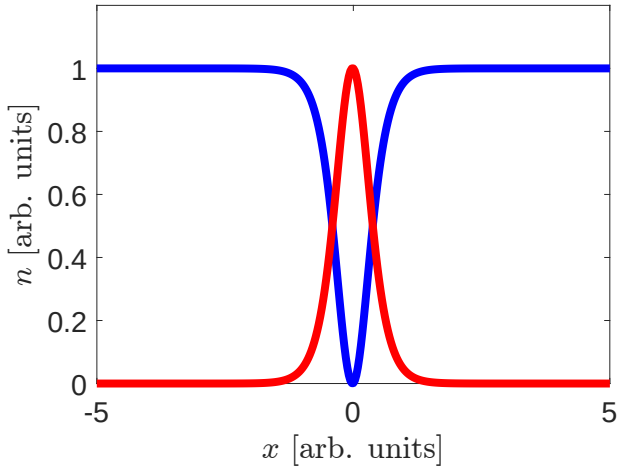

Figure 2.3.: Density distribution versus position of a dark-bright soliton plotted using Eq. (2.31). The first component has a dark soliton at its centre (blue line) and is filled by the bright soliton of the second component (red line). The ratio of particle numbers is $N_2/N_1 = 0.05$.

For dark-bright solitons, we also review Refs. [54, 85]; for dark-antidark solitons, we review Ref. [57]; and for magnetic solitons, we review Refs. [49, 86].
In the following, we refer to the component in which a vector soliton forms a density dip as the dark component, and to the other component as the bright component for dark-bright solitons, or as the antidark component for dark-antidark and magnetic solitons.

Dark-bright solitons

Dark-bright solitons (DBs) appear in binary BECs with highly imbalanced components (*e.g.* $N_1 \gg N_2$), both in the immiscible regime ($g_{12} > \sqrt{g_{11}g_{22}}$) and in the miscible regime, near the transition to immiscibility ($g_{12} \approx \sqrt{g_{11}g_{22}}$). They exhibit a density trough similar to a dark soliton in the dark component. The particles of the bright component populate this trough to minimise the interaction energy. For sufficiently large imbalances between the components, the trough can be populated by all particles of the bright component, resulting in a bright-like soliton in this component. The density distribution of a DB is shown in Figure 2.3.
One can easily achieve a DB in a binary BEC with two distinguishable components of Bose-condensed atoms. Such a system can be described by the following dimensionless coupled quasi-1D Gross-Pitaevskii equations (GPEs)

$$\begin{aligned} i\partial_t\tilde{\psi}_1 &= \left(-\frac{1}{2}\partial_{\tilde{x}}^2 + \tilde{V}_1(\tilde{x}) + \left|\tilde{\psi}_1\right|^2 + \tilde{g}_{12}\left|\tilde{\psi}_2\right|^2 - \tilde{\mu}\right)\tilde{\psi}_1, \\ i\partial_t\tilde{\psi}_2 &= \left(-\frac{1}{2}\partial_{\tilde{x}}^2 + \tilde{V}_2(\tilde{x}) + \left|\tilde{\psi}_2\right|^2 + \tilde{g}_{21}\left|\tilde{\psi}_2\right|^2 - \tilde{\mu} - \tilde{\Delta}\right)\tilde{\psi}_2, \end{aligned} \tag{2.30}$$

where $\tilde{\psi}_i$ is the dimensionless wavefunction of the i-th component with corresponding dimensionless trapping potential $\tilde{V}_i$, and $\tilde{\mu}_1 = \tilde{\mu}$ and $\tilde{\mu}_2 = \tilde{\mu} + \tilde{\Delta}$ are the dimensionless chemical potentials. The dimensionless inter-component interactions are given by $\tilde{g}_{12} =$

a_{12}/a_{11} and $\tilde{g}_{21} = a_{12}/a_{22}$. Note that Eq. (2.30) is rescaled in a way that $\tilde{g}_{11} = \tilde{g}_{22} = 1$. For binary BECs of ^{23}Na in different spin states, as well as those of ^{87}Rb, the inter-component interactions are naturally close to unity, allowing us to assume the system is in the Manakov regime ($g_{11} = g_{22} = g_{12}$) [61]. In this regime, the coupled quasi-1D GPEs (2.30) are integrable, and for $\tilde{V}_i(x) = 0$, the DB solutions are given by

$$\begin{aligned}\tilde{\psi}_1 &= i\sqrt{\tilde{\mu}}\sin\alpha + \sqrt{\tilde{\mu}}\cos\alpha\tanh\left[\tilde{\kappa}(\tilde{x} - \tilde{t}\tilde{\kappa}\tan\alpha)\right],\\ \tilde{\psi}_2 &= \sqrt{\frac{N_2\tilde{\kappa}}{2}}e^{i(\tilde{\Omega}_2\tilde{t}+\tilde{\kappa}\tan\alpha+\tilde{\phi})}\mathrm{sech}\left[\tilde{\kappa}(\tilde{x} - \tilde{t}\tilde{\kappa}\tan\alpha)\right],\end{aligned} \tag{2.31}$$

where $N_2 = \int |\psi_2|^2 dx$ is the particle number in the second component, α is an angle describing the soliton's velocity. The inverse length of the soliton is

$$\tilde{\kappa} = \sqrt{\tilde{\mu}\cos^2\alpha + (N_2/4)^2)} - N_2/4, \tag{2.32}$$

and the frequency shift of the second component is

$$\tilde{\Omega}_2 = \tilde{\kappa}^2(1 - \tan^2\alpha)/2 - \tilde{\Delta}. \tag{2.33}$$

For more information, the interested reader is referred to Ref. [85].
One of the early experimental realisations of dark-bright solitons was demonstrated by Becker *et al.* in 2008 [54], as shown in Fig. 2.4. They produced BECs in a cigar shaped geometry with an optical dipole trap with trapping frequencies of $\omega_{z,\mathrm{hor,vert}} = 2\pi \times \{5.9, 85, 133\}$Hz. The BECs consisted of $\sim 5 \times 10^4$ ^{87}Rb atoms in the $5^2S_{1/2}$, $|F = 1, m_F = 0\rangle$ state, onto which a dark soliton was imprinted. Simultaneously, a coherent Raman pulse transferred a small portion of the atoms to the $|F = 2, m_F = 0\rangle$ state in the region where the dark soliton formed in the $|F = 1, m_F = 0\rangle$ component. The authors predicted that dark-bright solitons, compared to their scalar counterparts, would remain stable far beyond the 1D regime. This was attributed to the fact that the length scale of DBs is of order of the spin-healing length, which diverges at the transition to the immiscible regime. Consequently, transverse excitations that could lead to decay into vortices are suppressed.
For more information on dark-bright solitons beyond the Manakov regime, see *e.g.*, Refs. [87–89].

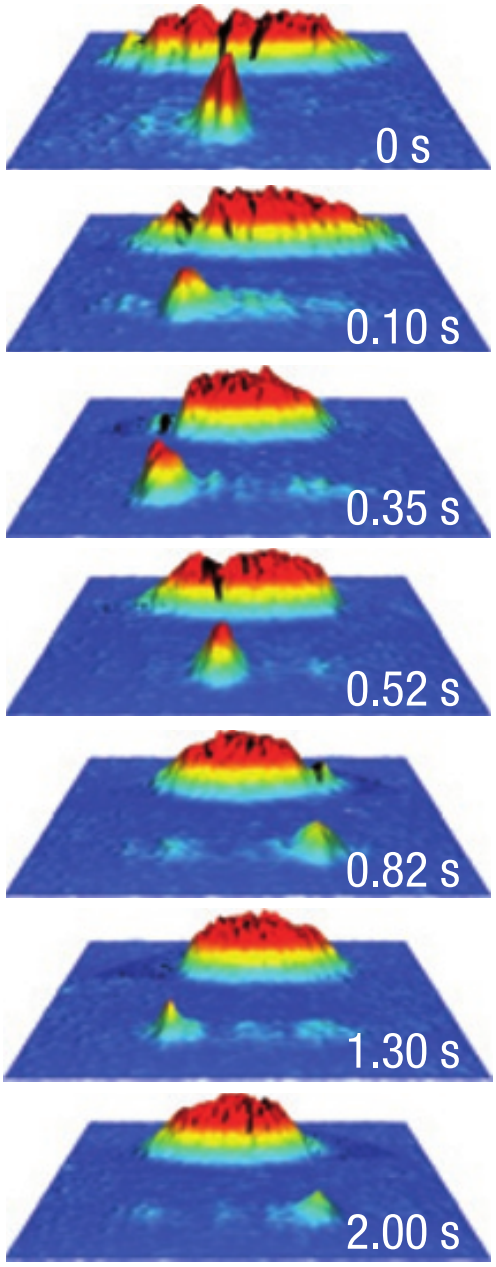

Figure 2.4.: Oscillation of a dark-bright soliton. Double absorption images are used to show the two components separately. The atoms in the front are in the $|F = 2, m_F = 0\rangle$ state and the atoms in the back are in the $|F = 1, m_F = 0\rangle$ state. Taken from Ref. [54].

Dark-antidark solitons

Danaila *et al.* [57] developed theory for dark-antidark solitons (DADs) in binary BECs in the miscible regime ($0 < g_{12} \lesssim \sqrt{g_{11}g_{22}}$). DADs appear as a density dip in one component (the dark component), resembling a dark soliton, and as a density peak on a miscible, homogeneous background in the other (the antidark component), similar to an antidark soliton. This is possible if the imbalances between the components are small, *i.e.* $n_0^{(1)} g_{11} \approx n_0^{(2)} g_{22}$, where $n_0^{(i)} = N_i/L$ is the average particle number in component i per

unit length L. In contrast, dark-bright solitons confine the atoms of the bright component exclusively within the density dip of the dark component.
DADs are described in 1D binary BECs by the coupled 1D GPEs

$$i\hbar\partial_t\psi_i = \left(-\frac{\hbar^2}{2m}\partial_x^2 + \sum_j g_{ij}^{\mathrm{1D}} n_j + \frac{1}{2}m\omega_x^2 x^2\right)\psi_i, \tag{2.34}$$

where $n_j = |\psi_j|^2$ is the 1D density, g_{ij}^{1D} is the 1D coupling constant. However, the coupled 1D GPEs (2.34) are generally not integrable, and exact DAD solutions exist only for $g_{12} \approx \sqrt{g_{11}g_{22}}$, which are referred to as magnetic soliton (see Sec. 2.3.2 Magnetic solitons). Accordingly, DADs are not true solitons in general, but they behave very similarly to true solitons.
Examples of stationary DADs are shown in Fig. 2.5 for different inter-component interactions g_{12}. The magnitude of the density peak, which occurs in the antidark component (red lines in Fig. 2.5), and the width of the DAD grow with g_{12}. Near the immiscibility transition ($g_{12} \approx \sqrt{g_{11}g_{22}}$), the density peak reaches the same magnitude as the depth of the density trough for $N_1 = N_2$. This is called a magnetic soliton. Far from the transition ($g_{12} \ll \sqrt{g_{11}g_{22}}$), the density peak gradually fades, becoming indistinguishable from the background density.
We can characterise a DAD by a localised phase gradient ϕ_1 across the dark component (blue lines in Fig. 2.5). In contrast, the antidark component is characterised by ϕ_2, which is influenced by ϕ_1, the population imbalance between the components, and the inter-component coupling constant g_{12} relative to $\sqrt{g_{11}g_{22}}$ (not shown).
Compared to the dark solitons, DADs are better characterised by their magnetisation (also called polarisation)

$$s_i = \frac{n_1(x_i)}{n_{1,\,\mathrm{max}}} - \frac{n_2(x_i)}{n_{2,\,\mathrm{max}}}, \tag{2.35}$$

where x_i is the position of soliton i, at which one component has a density minimum (maximum) and the other component has a maximum (minimum). The quantity $n_{1,\,\mathrm{max}}$ is the maximum density of component 1 for an isolated dark-antidark soliton with the antidark part in component 1; analogously, $n_{2,\,\mathrm{max}}$ refers to the maximum density of component 2 if the antidark part were in component 2. The definition of Eq. (2.35) guaranties $-1 \leq s_i \leq 1$.

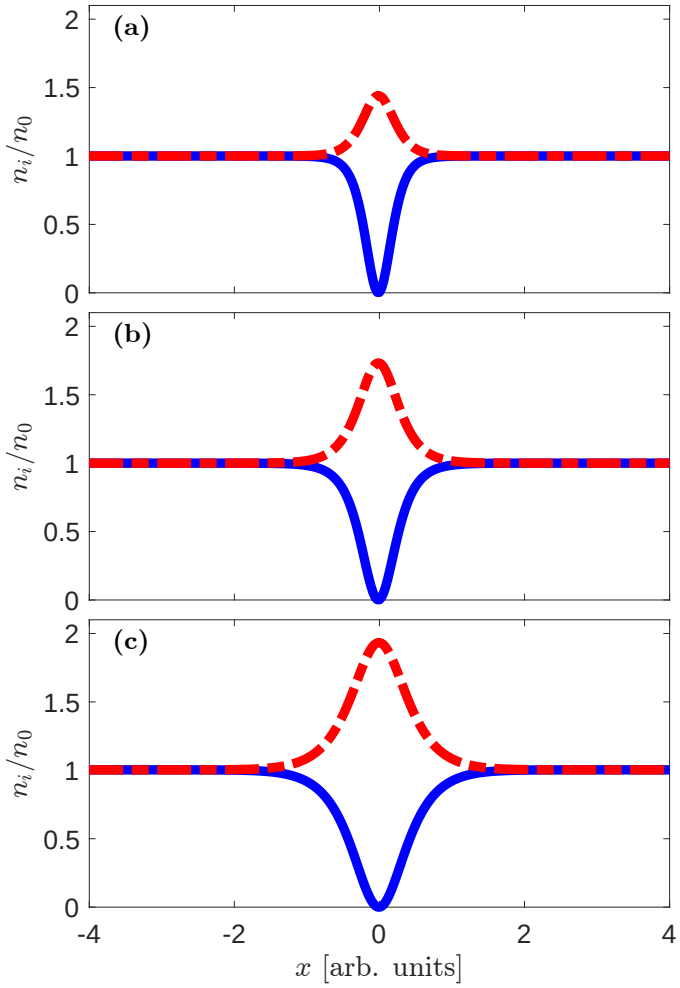

Figure 2.5.: Density profiles of dark-antidark solitons with (a) $g_{12} = 0.5g$ and (b) $g_{12} = 0.75g$ for balanced components ($g_{11} = g_{22} = g$ and $n_0^{(1)} = n_0^{(2)} = n_0$). (c) shows a magnetic soliton with $g_{12} = 0.95g$. The blue line shows the density of the first (dark) component and the dashed red line shows the second (antidark) component. Parameters: average integrated density per component $n_0 = N/2L = 50\,\mu\text{m}^{-1}$; total particle number $N = 3000$; interactions $a_{11} = a_{22} = 100\,a_0$; radial confinement $\omega = 2\pi \times 2667\,\text{Hz}$.

In Ref. [57], Danaila *et al.* provided pioneering experimental evidence of a DAD, as shown in Fig. 2.6. They created cigar-shaped BECs of 8×10^5 ^{87}Rb atoms in the $|1, -1\rangle$ hyperfine state and applied a microwave pulse that transferred approximately 50% of the atoms into the $|2, -2\rangle$ state. The trap frequencies were $\{\omega_x, \omega_y, \omega_z\} = 2\pi \times \{1.4, 176, 174\}$ Hz and the scattering lengths were $\{a_{11}, a_{12}, a_{22}\} = \{100.4, 98.98, 98.98\}a_0$, where a_{11} is the intra-component scattering length for the $|1, -1\rangle$ atoms, a_{22} is the intra-component scattering length for the the $|2, -2\rangle$ atoms, and a_{12} is the inter-component scattering length. Here, a_0 is the Bohr radius. The atoms in the $|1, -1\rangle$ state were transferred uniformly across the condensate to the $|2, -2\rangle$ state. Due to $a_{11} > a_{22}$, the ground-state density distribution of the $|2, -2\rangle$ atoms was narrower and higher compared to the density distribution of the $|1, -1\rangle$ atoms. After the microwave pulse, the $|2, -2\rangle$ atoms began to move towards the

centre, creating a localised phase gradient, which in turn led to a DAD.

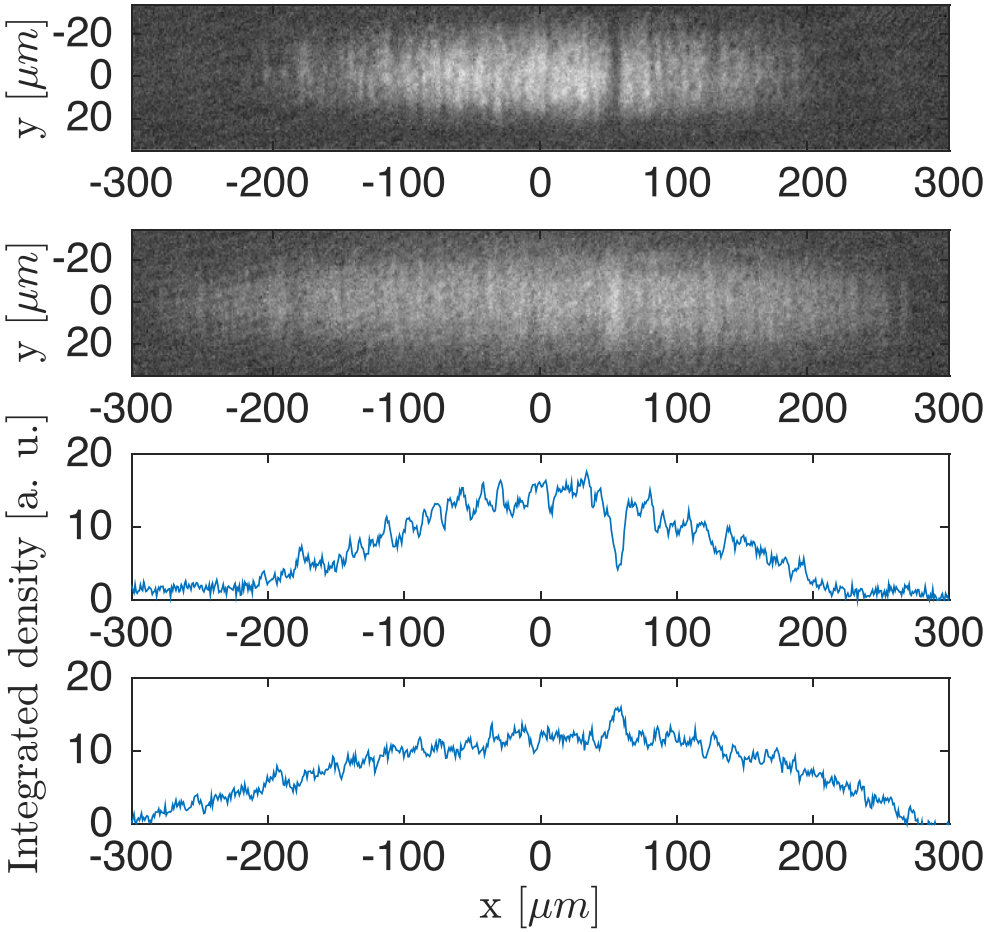

Figure 2.6.: Evidence of a dark-antidark soliton. The first (second) panel shows the absorption images of the atoms in state $|2,-2\rangle$ ($|1,-1\rangle$) after 10 ms of expansion. The third (fourth) panel shows the corresponding integrated density of the $|2,-2\rangle$ ($|1,-1\rangle$) state. Evidence of a dark-antidark soliton can be seen at $x \approx 50\,\mu$m. Taken from Ref. [57].

Magnetic solitons

Magnetic solitons (MSs) are dark-antidark solitons that arise in balanced binary BECs within the miscible regime ($n_0^{(1)} g_{11} = n_0^{(2)} g_{22}$ and $m_1 = m_2$), near the transition to the immiscible regime. In this regime, the inequality

$$0 < \delta g = \sqrt{g_{11} g_{22}} - g_{12} \ll \sqrt{g_{11} g_{22}}, \tag{2.36}$$

holds. Within such a system, the MS appears as a localised density dip in the dark component and a localised density peak in the antidark component, such that the total density, $n(x) = n_1(x) + n_2(x)$, is approximately constant.
In non-dipolar binary BECs, where Eq. (2.36) is fulfilled, magnetic solitons are analytic

solitons to the coupled 1D GPEs (2.34). The wavefunctions are given by

$$\begin{pmatrix}\psi_1(x,t)\\ \psi_2(x,t)\end{pmatrix} = \begin{pmatrix}\sqrt{n_1(x,t)}e^{i\phi_1(x,t)}\\ \sqrt{n_2(x,t)}e^{i\phi_2(x,t)}\end{pmatrix}, \tag{2.37}$$

where $n_i(x)$ denotes the density and $\phi_i(x)$ the phase of component i, with $i \in \{1,2\}$. Introducing the relative phase

$$\phi_A = \phi_1 - \phi_2, \tag{2.38}$$

the total phase $\phi_B = \phi_1 + \phi_2$, and the spin polarisation distribution $\cos\theta = (n_1 - n_2)/n$, the wavefunctions can be rewritten as

$$\begin{pmatrix}\psi_1\\ \psi_2\end{pmatrix} = \sqrt{n}\begin{pmatrix}\cos(\theta/2)e^{i(\phi_B+\phi_A)/2}\\ \sin(\theta/2)e^{i(\phi_B-\phi_A)/2}\end{pmatrix}. \tag{2.39}$$

Inserting Eq. (2.39) into Eq. (2.34), and following the steps laid out in Ref. [49], one obtains three coupled equations

$$\begin{aligned}\partial_\zeta\phi_B =& -\cos\theta\partial_\zeta\phi_A,\\ \partial_\zeta\phi_A =& \tilde{v}\frac{\cos\theta}{\sin^2\theta},\\ \partial_\zeta^2\theta =& \tilde{v}^2\frac{\cos\theta}{\sin^3\theta} - \sin\theta\cos\theta,\end{aligned} \tag{2.40}$$

where $\tilde{v} = v/c_s$ is the velocity of the soliton v divided by the speed of sound $c_s = \sqrt{n\delta g/2m}$, $\zeta = (x - vt)/\xi_s$ represents the dimensionless position of the soliton, and $\xi_s = \hbar/\sqrt{2mn\delta g}$ is the spin-healing length. It describes the characteristic length scale of spin excitations (out-of-phase density modulations) that occur only in the spin density $n_s(x) = n_1(x) - n_2(x)$, while keeping the total density n constant.
For $g_{11} = g_{22} = g$, magnetic soliton solutions of the coupled equations (2.40) take the form

$$n_{1,2}(\zeta) = \frac{n}{2}(1 \pm \cos\theta) = \frac{n}{2}\left[1 \pm \frac{\sqrt{1-\tilde{v}^2}}{\cosh\zeta\sqrt{1-\tilde{v}^2}}\right], \tag{2.41}$$

with relative phase

$$\cot\phi_A(\zeta) = -\sinh\left(\zeta\sqrt{1-\tilde{v}^2}\right)/\tilde{v}. \tag{2.42}$$

Intriguingly, MSs exhibit a total phase gradient of π in ϕ_A for all values of $0 \leq \tilde{v} < 1$. This is in contrast to the single-component case, where only black solitons ($v = 0$) display a total phase gradient of π. An example of the density profile of an MS with $v = 0$ is shown in Fig. 2.5(c).
For an MS, the magnetisation (2.35) is equivalent to

$$s_i = \frac{n_1(x_i) - n_2(x_i)}{n}. \tag{2.43}$$

The energy of MSs can be evaluated via

$$E_{\mathrm{MS}} = \frac{n\hbar c_s}{4} \int d\zeta \left[(\partial_\zeta \theta)^2 + \sin^2\theta (\partial_\zeta \phi_A)^2 + \cos^2\theta \right]. \tag{2.44}$$

Plugging Eq. (2.41) and (2.42) into Eq. (2.44) gives the energy

$$E_{\mathrm{MS}}(\tilde{v}) = n\hbar c_s \sqrt{1-\tilde{v}^2} \tag{2.45}$$

for an isolated soliton, with effective mass m^*

$$m^* = \frac{1}{\tilde{v} c_s^2} \frac{dE_{\mathrm{MS}}}{d\tilde{v}} = -\frac{n\hbar}{c_s} \left(1-\tilde{v}^2\right)^{-1/2}. \tag{2.46}$$

A Taylor expansion reveals that we can describe slow moving solitons as quasiparticles with negative effective mass $m^* = -n\hbar/c_s$.

2.4. Dipole-dipole interactions

In dipolar BECs composed of particles with strong dipole moments, such as erbium [90] and dysprosium atoms [91] (magnetic) or sodium–caesium molecules (electric) [92, 93], particles interact via dipole-dipole interactions (DDI), alongside contact interactions. In this section, we review the theoretical description of polarised dipolar BECs, following Ref. [94], considering only particles with magnetic dipole moment. Subsequently, in Sec. 2.4.1, we examine solitons in dipolar BECs.

A particle at position $\mathbf{x}_1$ with a permanent magnetic dipole moment $\boldsymbol{\mu}$ along the unit vector $\mathbf{e}_1$ exerts a force on a second identical particle at $\mathbf{x}_2$ aligned along $\mathbf{e}_2$, depending on their relative position $\mathbf{r} = \mathbf{x}_2 - \mathbf{x}_1$ [see Fig. 2.7(a)]. The DDI potential of the two particles reads

$$U_{\mathrm{dd}}(\mathbf{r}) = \frac{\mu_0 \mu^2}{4\pi} \frac{(\mathbf{e}_1 \cdot \mathbf{e}_2) r^2 - 3(\mathbf{e}_1 \cdot \mathbf{r})(\mathbf{e}_2 \cdot \mathbf{r})}{r^5}, \tag{2.47}$$

where $r = |\mathbf{r}|$, $\mu = |\boldsymbol{\mu}|$ and μ_0 is the permeability of vacuum.

If the particles are polarised along the unit vector $\mathbf{e}_1$, *e.g.*, by an external magnetic field $\mathbf{B}$, the DDI potential can be fully characterised by the magnetic dipole moment μ, the distance r, and the angle ϑ between $\mathbf{e}_1$ and $\mathbf{r}$ [see Fig. 2.7(b)]. Then Eq. (2.47) becomes

$$U_{\mathrm{dd}}(\mathbf{r}) = \frac{\mu_0 \mu^2}{4\pi} \frac{1 - 3\cos\vartheta}{r^3}. \tag{2.48}$$

Introducing the dipole length $a_{\mathrm{dd}} = m\mu_0\mu^2/12\pi\hbar^2$, we can rewrite Eq. (2.48) as

$$U_{\mathrm{dd}}(\mathbf{r}) = \frac{3g_{\mathrm{dd}}}{4\pi} \frac{1 - 3\cos\vartheta}{r^3}, \tag{2.49}$$

where $g_{\mathrm{dd}} = 4\pi\hbar^2 a_{\mathrm{dd}}/m$ is the dipole coupling constant. We observe that the DDIs are long-ranged and anisotropic. In side-by-side configurations, particles repel each other,

whereas in head-to-tail configurations, they attract each other.

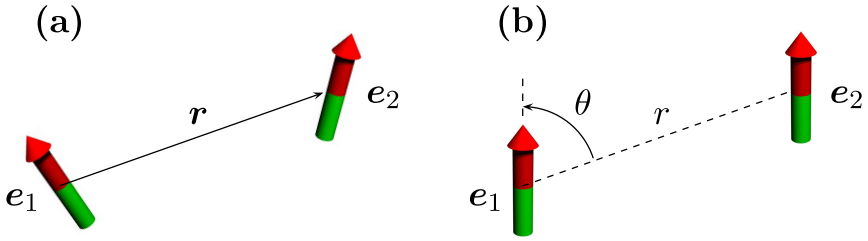

Figure 2.7.: Visualisation of dipole-dipole interaction between two particles. (a) The particles have random orientation. (b) The particles are polarised along $\mathbf{e}_1 = \mathbf{e}_2$. Taken from Ref. [94].

The contact interactions and the DDIs can be treated separately, allowing the total potential $U_{\text{tot}}(\mathbf{r})$ to be expressed as the sum of the pseudo-potential $U_s(\mathbf{r})$ (2.11) and the DDI potential $U_{\text{dd}}(\mathbf{r})$, given by

$$U_{\text{tot}}(\mathbf{r}) = g_s\delta(\mathbf{r}) + \frac{3g_{\text{dd}}}{4\pi}\frac{1-3\cos\vartheta}{r^3}. \tag{2.50}$$

Inserting Eq. (2.50) into Eq. (2.10) yields the Hamiltonian

$$\hat{H} = \int d\mathbf{r}\hat{\Psi}^\dagger(\mathbf{r})\left[-\frac{\hbar^2\nabla^2}{2m} + V(\mathbf{r},t) + \int d\mathbf{r}'\hat{\Psi}^\dagger(\mathbf{r}')U_{\text{tot}}(\mathbf{r}'-\mathbf{r})\hat{\Psi}(\mathbf{r}')\right]\hat{\Psi}(\mathbf{r}). \tag{2.51}$$

2.4.1. Solitons in dipolar BECs

This subsection reviews some general features of dark solitons in dipolar condensates. For more information, the interested reader is referred to, *e.g.*, Ref. [34, 35].
In a dipolar BEC, the quasi-1D GPE is given by

$$i\hbar\partial_t\psi(x) = \left(-\frac{\hbar^2}{2m}\partial_x^2 + \frac{1}{2}m\omega_x^2x^2 + \frac{g_sn(x)}{2\pi l^2} + \int dx'\ \Phi^{\text{1D}}(x-x')|\psi(x')|^2\right)\psi(x), \tag{2.52}$$

where $l = \sqrt{\hbar/m\omega_\rho}$ is the characteristic length scale of the harmonic trap potential with trap frequency $\omega_\rho \equiv \omega_y = \omega_z$ in the $y-z$ plane and Φ^{1D} is the 1D dipolar pseudo-potential given by

$$\Phi^{\text{1D}}(u) = \frac{3g_{dd}}{4\pi}\frac{1+3\cos 2\theta}{8l^3}\left[2u - \sqrt{2\pi}\left(1+u^2\right)e^{u^2/2}\text{erfc}\left(\frac{u}{\sqrt{2}}\right) + \frac{8}{3}\delta(u)\right], \tag{2.53}$$

where $u = x/l$. The quasi-1D GPE (2.52) is not integrable due to the long-ranged DDIs. Accordingly, true solitons are no longer supported. However, solitary wave solutions still exist, which behave very similar but collide inelastically. In this case a better term for these excitations are solitary waves. Regardless, in the following, we use the term solitons for these soliton-like excitations for simplicity.
The density profile of dark solitons in dipolar BECs depends on the orientation of the dipoles. When the dipoles are aligned perpendicular to the tube axis (here, the x-axis),

density modulations form around the central density dip of the dark soliton due to the head-to-tail attraction and side-by-side repulsion of the dipoles. Since the soliton creates a density trough at its centre, the dipoles next to the trough feel less repulsive DDIs from that area and tend to form a region of high density around it. This, in turn, leads to a region of lower density next to the high-density region, reducing the energy cost due to side-by-side repulsion. However, this low-density area is less deep than the central trough of the soliton. We refer to the alternating high-density and low-density areas as ripples. The strength of the ripples can be quantified by the ratio $\varepsilon_{dd} = a_{\mathrm{dd}}/a_s$ between the dipole and the s-wave scattering length. Figure 2.8 shows examples of the density profiles of black solitons for various ε_{dd}. We can see that the blue line ($\varepsilon_{dd} = 2$) shows large density peaks around the central trough of the soliton and small density dips next to the peaks. For $\varepsilon_{dd} = 1$, the density of the soliton shows small peaks around the trough and quickly becomes indistinguishable from the density of the non-dipolar soliton ($\varepsilon_{dd} = 0$).

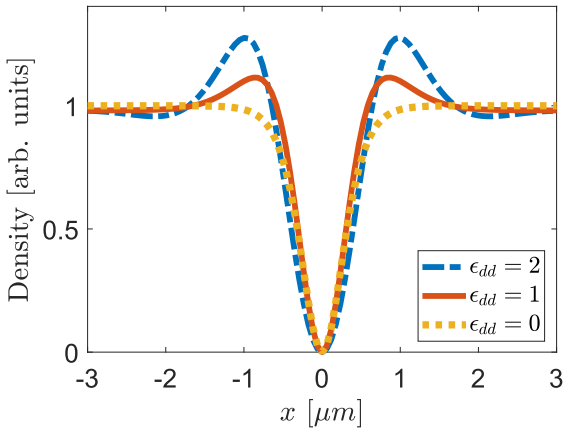

Figure 2.8.: Examples of the density distributions of black solitons with different $\varepsilon_{dd} = a_{dd}/a_s$. For the yellow dashed and the red line, $a_s = 130a_0$, and for the blue dashed line, $a_s = 65a_0$.

3. Recent research developments

In this chapter, we review recent experimental and theoretical research developments of solitons in non-dipolar binary BECs and single component dipolar BECs. In Sec. 3.1, we examine recent vector soliton experiments with dark-antidark solitons and magnetic solitons. These solitons are predicted to form bound states [51–53, 55, 56, 83, 84] and represent a primary focus of this thesis. In Sec. 3.2, we review theoretical work on dark solitons in dipolar BECs, predicting the formation of bound states around an equilibrium separation. In Sec. 3.3, we summarise the findings of the experimental and theoretical work on solitons. We then outline the main focus of this thesis: deepening our understanding of the formation of bound states between magnetic solitons and dark-antidark solitons in binary BECs and extending the theory of bound states to binary dipolar BECs.

3.1. Relevant experiments of magnetic solitons and dark-antidark solitons in binary condensates

Following the recent experimental realisations of magnetic solitons in two components [59] and three components [60] in 2020, as well as dark-antidark solitons in two components in 2016 [57], interest in vector solitons has increased significantly. In this section, we review three relevant experiments [52, 59, 60], presented in chronological order.
In the following, we omit the terms magnetic solitons and dark-antidark solitons, referring to them simply as solitons whenever the context is clear. Furthermore, we refer to solitons with $s_i < 0$ as $\downarrow$ solitons and to solitons with $s_i > 0$ as $\uparrow$ solitons.

3.1.1. Magnetic solitons

The research group led by G. Ferrari was the first to experimentally realise magnetic solitons in a two-component BEC [59]. They created BECs with 2×10^6 ^{23}Na atoms in an elongated trap with trap frequencies $\{f_y, f_\perp\} = \{8.7(1.2), 585(2)\}$ Hz. The atoms were initially in the $|1, -1\rangle$ state, and an effective Rabi frequency of 268(2) Hz transferred the atoms via two-photon microwave radiation into a condensate mixture of $|1, \pm 1\rangle$.
The solitons were generated by applying an optical dipole potential to one side of the condensate mixture, as shown in the top panel of Fig. 3.1. The two condensates accumulated opposite phases due to their opposing angular momenta and shining the light for $\tau = 70\,\mu$s imprinted a total phase difference of $\Delta\phi_{|1,\pm1\rangle} = \phi_{|1,\pm1\rangle}(y = 200\,\mu\text{m}) - \phi_{|1,\pm1\rangle}(y = -200\,\mu\text{m}) = \pm\pi$ across the centre of each respective condensate. The width of the imprinted

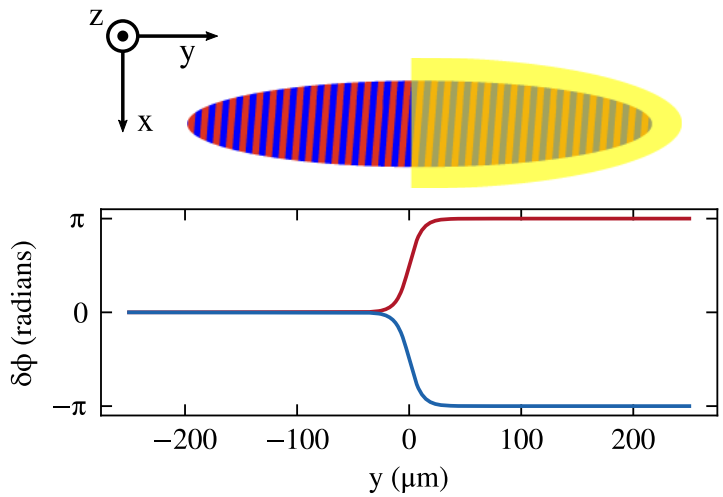

Figure 3.1.: Upper panel: Schematic representation of the spin-selective optical potential, generating magnetic solitons. Lower panel: Phase distribution of the atoms in the $|1,-1\rangle$ (blue line) and $|1,1\rangle$ (red line) states as a function of position y. Taken from Ref. [59].

phase was governed by the intensity profile of the light beam, which had an edge width (from 10% to 90%) of 2 μm. The resulting phase profile, also called the Son-Stephanov phase domain wall[1], is depicted in the lower panel of Fig. 3.1. This created two solitons stacked on top of each other, moving in opposite directions and exhibiting opposite magnetisation. The authors were able to fully characterise solitons during oscillatory motion in the trap and found a dependence of the oscillation amplitude on the peak velocity, which agrees well with the theoretical prediction in Ref. [49]. Furthermore, they investigated collisions between solitons with equal and opposite magnetisation by imprinting two phase domain walls separated by 100 μm. This resulted in the creation of two soliton pairs, each consisting of an $\uparrow$ soliton ($s = 0.86$) and a $\downarrow$ soliton ($s = -0.86$). Because of the way they were imprinted, the $\uparrow$ solitons moved toward each other, while the $\downarrow$ solitons travelled to the edges of the trap. Figure 3.2(b) shows the $\uparrow\uparrow$ collision between the two $\uparrow$ solitons. The solitons collided, and it is unclear whether they bounced off each other or passed through one another. After the collision, the solitons acquired a higher velocity ($s' = 0.62$), as indicated by their relative positions in Fig. 3.2(d). After the $\downarrow$ solitons hit the condensate edge and returned, $\uparrow\downarrow$ collisions between solitons with opposite magnetisation happened naturally, where the solitons passed through one another. This is shown in Fig. 3.2(a) with the relative positions in (c). The authors refrained from drawing conclusions on the dissipations of the $\uparrow\downarrow$ collisions due to significant noise after long evolution times.

[1]We cover Son-Stephanov phase domain walls in depth in Sec. 5.2.2.

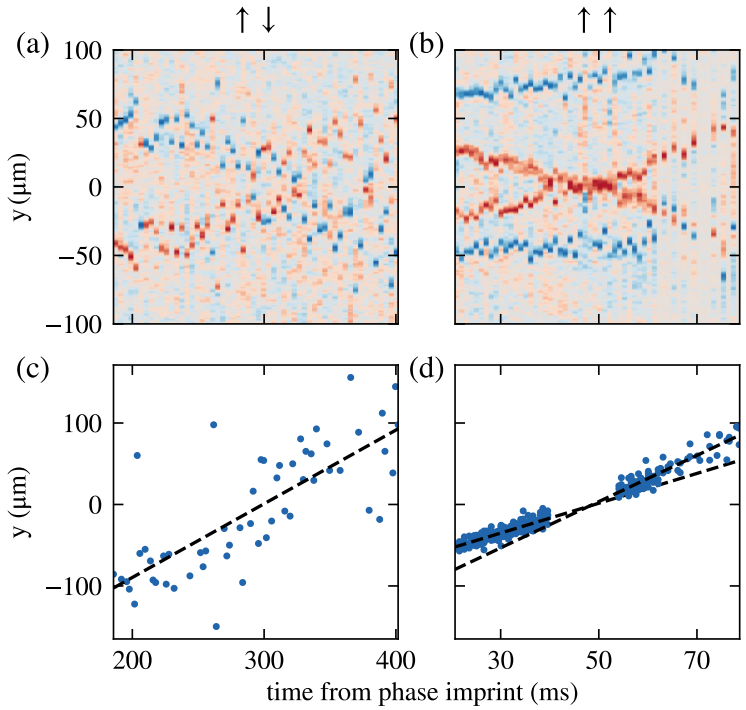

Figure 3.2.: Collisions between magnetic solitons with opposite magnetisation (a), (c) and equal magnetisation (b), (d). The time evolution of the collisions is shown in (a) and (b), where red points represent the position of ↑ solitons and blue points represent ↓ solitons. Panels (c) and (d) show the relative position of the solitons with respect to each other near the collision, corresponding to the time evolutions in (a) and (b), respectively. Taken from Ref. [59].

3.1.2. Magnetic solitons in spin-1 condensates

On the same day as Ref. [59], Chai *et al.* published their results on the experimental realisation of magnetic solitons in a spin-1 BEC [60]. The authors created BECs similar to the experiment in Ref. [59], with 2.1×10^7 ^{23}Na atoms in a cigar-shaped trap with trap frequencies $\{f_y, f_\perp\} = \{5.4, 380\}$ Hz. The atoms were initially in the $|1, 0\rangle$ state and were transferred approximately equally to the states $|1, \pm 1\rangle$ with a radio-frequency pulse of 160 μs and a magnetic shadow pulse described in the supplements of Ref. [60]. The transfer process left a residual population of less than 5% in the $|1, 0\rangle$ state. The solitons were created by imprinting a Son-Stephanov phase domain wall on the atoms in the $|1, \pm 1\rangle$ state, which resulted in a phase distribution similar to Fig. 3.1. The imprinting process was preformed by shining a magnetic shadow on the condensate mixture, produced by the placement of a thin metal edge in a circularly polarised light beam. The shadow of this metal edge, with an edge width (10% to 90%) of 8 μm, was then imaged onto the atom cloud for 120 μs to generate the Son-Stephanov phase domain wall.
The authors investigated the formation and propagation of the solitons after imprinting and compared them to numerical simulations. They investigated the relationship between the magnetisation s and the velocity v of the solitons and found good agreement with the

theoretical prediction given in Ref. [49]

$$|s| = \sqrt{1 - \frac{v^2}{c_s^2}}, \tag{3.1}$$

where c_s is the speed of sound for spin waves. Further, they considered the dynamics of two

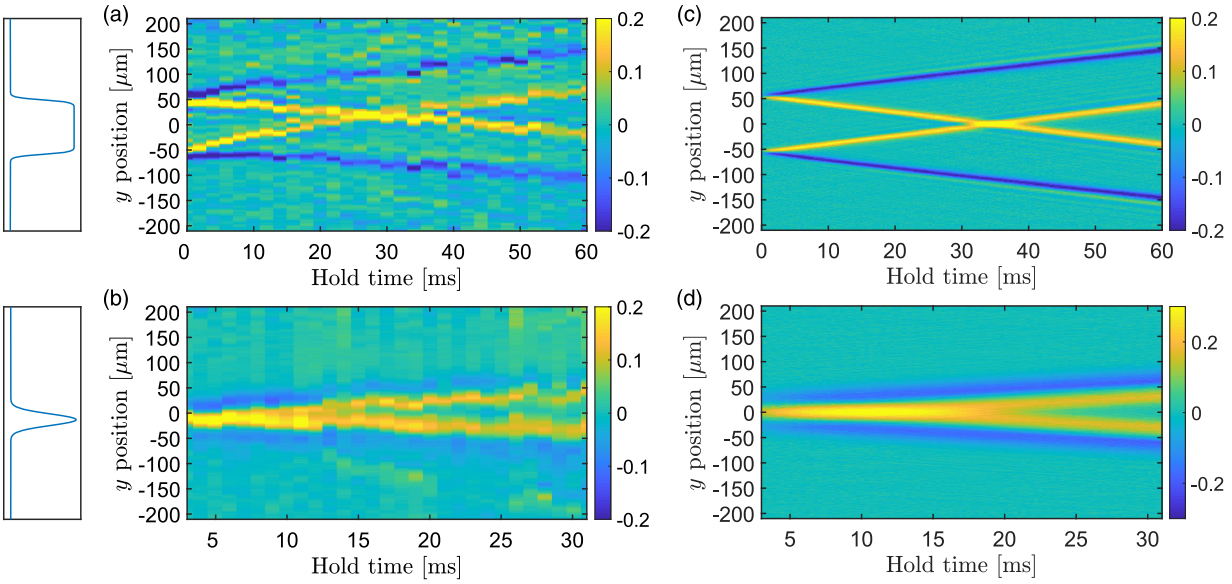

Figure 3.3.: Collisions between ↑ solitons as a function of time. (a) Two phase domain walls are imprinted 110 μm from each other, resulting in a relative phase profile as depicted in the upper left panel. Four solitons emerge and the two ↑ solitons (yellow) collide at ≈ 25 ms. (b) Two phase domain walls are imprinted almost on top of each other by a light beam imprinting a relative phase profile as depicted in the lower left panel. The resulting two ↑ solitons (yellow) collide nearly immediately. The corresponding numerical simulations of (a) and (b) are shown in (c) and (d), respectively. Taken from Ref. [60].

phase domain walls imprinted with different initial separations in Fig. 3.3. Four solitons with large velocity ($\approx 0.82 c_s$) were produced this way, with two ↑ solitons in the middle and two ↓ solitons on the outsides. In Fig. 3.3(a) the phase domain walls are well separated and the ↑ solitons pass through one another at ≈ 25 ms. The associated numerical simulation is shown in Fig. 3.3(c), predicting a collision to occur at ≈ 35 ms. In Fig. 3.3(b), the phase domain walls are imprinted nearly on top of each other, causing the two inner solitons to collide almost immediately. Figure 3.3(d) shows the associated numerical simulation.
Compared to the purely two-component experiment in Ref. [59], the experiment by Chai *et al.* involved a three-component gas, with one component being greatly suppressed. Although, the solitons showed identical behaviour in both experiments, there have been predictions for bound states between two solitons in the three-component gas called Flemish strings [53]. These Flemish strings can occur between solitons with opposite magnetisation as depicted in Fig. 3.4. The solitons are curling around each other, and if the separation after each curl decreases, the soliton pair can annihilate.

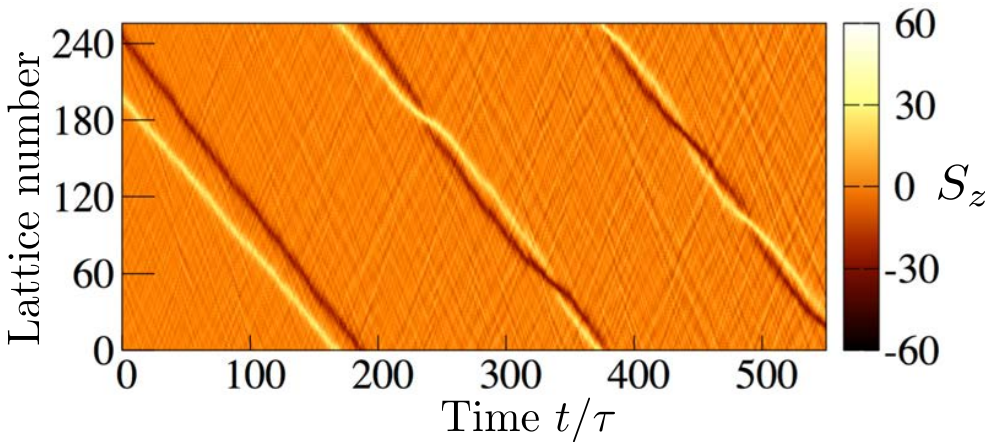

Figure 3.4.: Formation of a Flemish string. Shown is the spatio-temporal evolution of two magnetic solitons (bright yellow and dark brown) in a spin-1 BEC. S_z is the magnetisation along the z axis. Taken from Ref. [53].

3.1.3. Interacting dark-antidark solitons

In the same year as the experimental realisation of magnetic solitons [59, 60], Katsimiga *et al.* [52] realised multiple dark-antidark solitons in their experiment. Although not their first experimental realisation of DADs, this collaboration between experimentalists and theorists analysed the dynamics of solitons with equal and opposite magnetisation, and explored possible bound states between the solitons, arising from these dynamics.
The authors created BECs of 4.5×10^5 ^{87}Rb atoms in the $|1,-1\rangle$ hyperfine state. The atoms were confined in a cigar shaped trap with $\{\omega_x, \omega_y, \omega_z\} = 2\pi \times \{1.5, 140, 180\}$ Hz. An external magnetic field created a Zeeman shift and a microwave field was driving Rabi oscillations between the $|1,-1\rangle$ and $|2,-2\rangle$ state. The resulting population in the $|2,-2\rangle$ state $P_{|2,-2\rangle}(x,t)$ varied with time t and was dependent on the resonant Rabi frequency Ω and the detuning of the microwave field $\delta(x)$, and was given by

$$P_{|2,-2\rangle}(x,t) = \frac{\Omega^2}{\Omega^2 + \delta^2(x)} \sin\left[\frac{\sqrt{\Omega^2 + \delta^2(x)}}{2} t\right]. \tag{3.2}$$

The authors shined the microwave field for $t = 15$ ms on the condensate, which created a phase pattern on both components, dependent on the detuning $\delta(x)$. Figure 3.5 shows six panels, each containing absorption images of both states along with their corresponding integrated cross-sections, for $\Omega = 2\pi \times 19$ kHz, and for various values of $\delta(x)$ and evolution times. Figure 3.5(a) shows the absorption images and integrated densities after the driving field with $\delta \approx 0$ was switched off. An alternating density pattern with short-wavelength modulations is visible in both components. Subsequently, the condensate mixture evolved in the trap for 150 ms, and the resulting density distribution is shown in Fig. 3.5(b). We observe an array of multiple solitons with spatially alternating magnetisation ($\uparrow\downarrow\uparrow\downarrow\ldots$). The density after an additional evolution of 260 ms is shown in Fig. 3.5(c), where the solitons are positioned irregularly due to their differing velocities. The same times are

shown in Fig. 3.5(d)-(f) for the detuned case with $\delta = 2\pi \times 11\,\mathrm{kHz}$. The detuning allowed only for ↓ solitons (s<0) to form in the condensate mixture. Fig. 3.5(d) shows an alternating density pattern with long-wavelength modulations in both components. Fig. 3.5(f) shows persistent clusters between ↓ solitons.

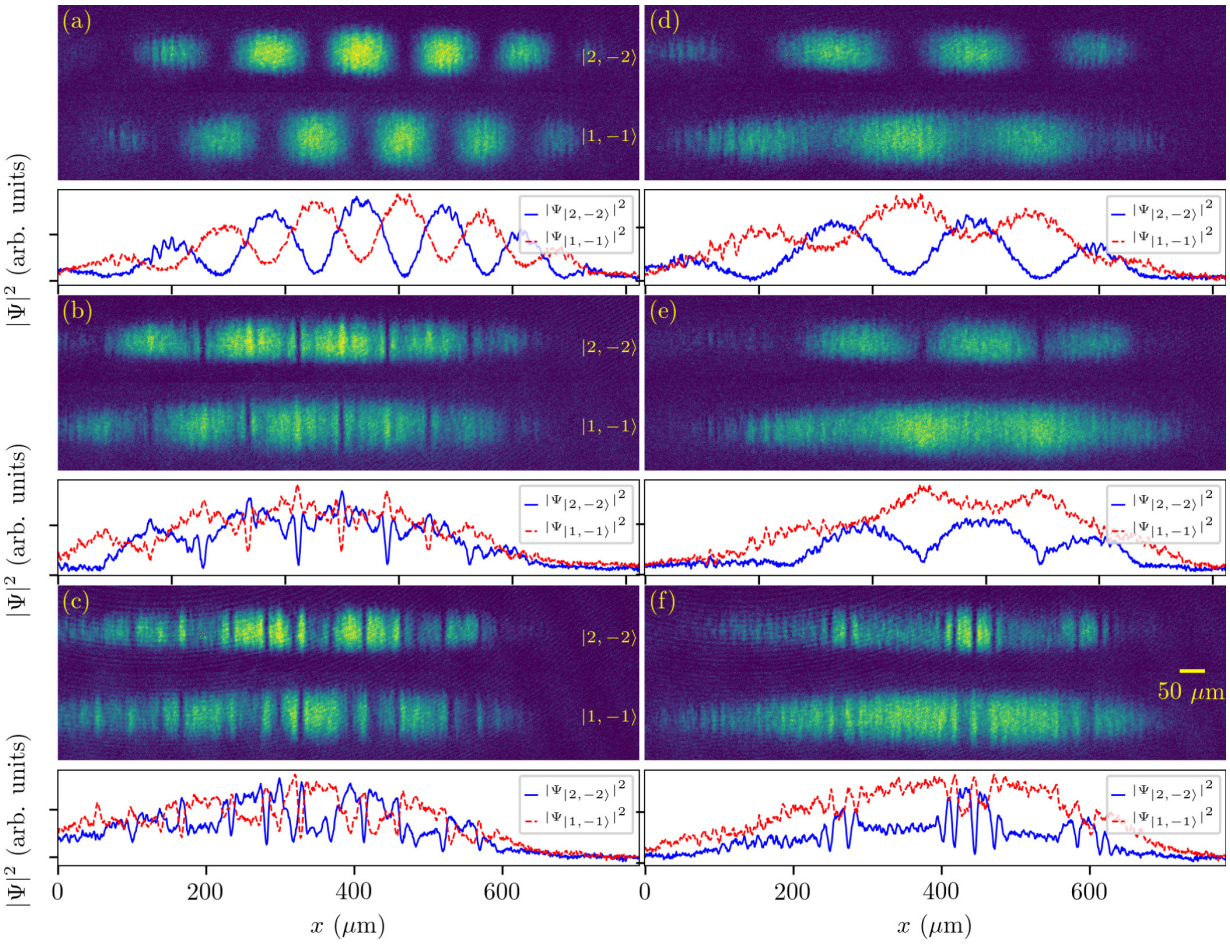

Figure 3.5.: Absorption images and corresponding integrated densities of the evolution after driving the microwave field for 15 ms. The evolution is shown for $\delta \approx 0\,\mathrm{kHz}$ [$\delta = 2\pi \times 11\,\mathrm{kHz}$] in (a)-(c) [(d)-(f)]. (a) and (d) show the respective density distribution after the microwave field is turned off. (b) and (e) show the densities after 150 ms of evolution in the trap, while (c) and (f) show the densities after a total of 410 ms of evolution. Taken from Ref. [52].

The authors investigated the formation of stable clusters between multiple ↓ solitons in detail using numerical simulations of a system comparable to the one in the experiments. They found that binary BECs in a cigar-shaped geometry support stationary states between two ↓ solitons for certain separations, $\Delta x_{\mathrm{stat}} = x_2 - x_1$, which depend on the inter-component s-wave scattering length a_{12} relative to the intra-component s-wave scattering lengths (for ^{87}Rb: $a_{11} = 100.4a_0$ and $a_{22} = 98.98a_0$). The density distributions of stationary configurations are shown Fig. 3.6 for various a_{12}. Far from the transition to the immiscible regime, Fig. 3.6(a) shows that the antidark part of the soliton is only a small peak, and Δx_{stat} is very small. Close to the transition to the immiscible regime, the density peak in

the antidark component is very large and x_{stat} is also large, as depicted in Fig. 3.6(d).

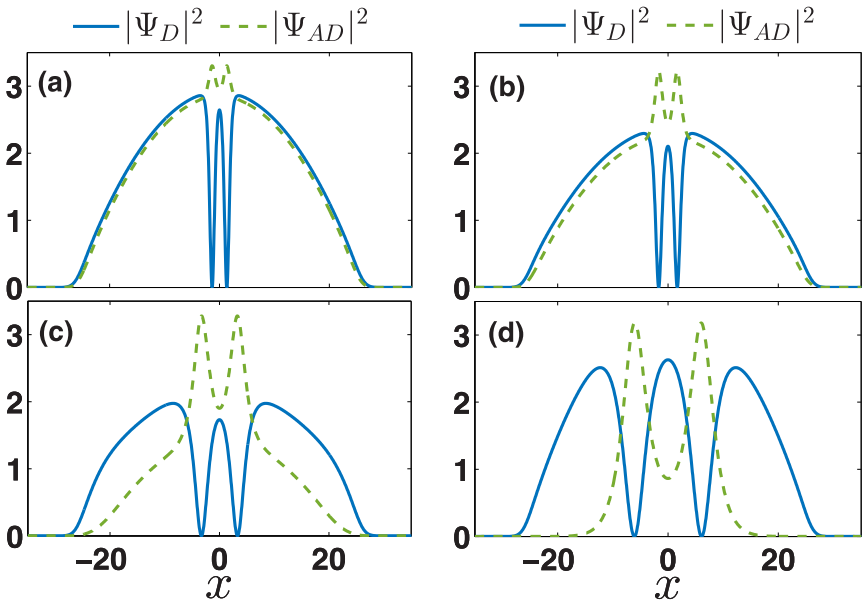

Figure 3.6.: Density profiles of stationary states of two dark-antidark solitons with equal magnetisation for the inter-component scattering lengths (a) $a_{12} = 20a_0$, (a) $a_{12} = 50a_0$, (a) $a_{12} = 90a_0$ and (d) $a_{12} = 98a_0$. The blue line shows the density of component 1 (D) with the dark part of solitons and the green dashed line shows the density of component 2 (AD) with the antidark part. The intra-component scattering lengths are $a_{11} = 100.4a_0$ and $a_{22} = 98.98a_0$. The position x and density $|\Psi_i|^2$ is shown in dimensionless units. Taken from Ref. [52].

Furthermore, the authors discovered that for certain ranges of a_{12}, instabilities existed that prevented any stationary separations (see Fig. 3 in Ref. [52]). For three or more aligned solitons, stationary configurations were also possible, but a wider range of a_{12} led to instabilities.

Finally, Katsimiga *et al.* also investigated the dynamics between solitons with opposite magnetisation. The dynamics for $a_{12} = 60a_0$ (upper two panels) and $a_{12} = 96a_0$ (lower two panels) are shown in Fig. 3.7. The first and third panels show the first component, and the second and fourth panel show the second component. Figure 3.7 shows that the solitons pass through one another and oscillate with increasing amplitude, independent of a_{12}. When the solitons reach the boundary, strong phonon excitations are produced, resulting in the loss of a soliton at $t \approx 2000$ in the $a_{12} = 60a_0$ case. The $a_{12} = 96a_0$ case, however, shows the development of a stable oscillation of the two solitons through each other for late time ($t > 2000$). This is also known as beating dark-dark solitons.

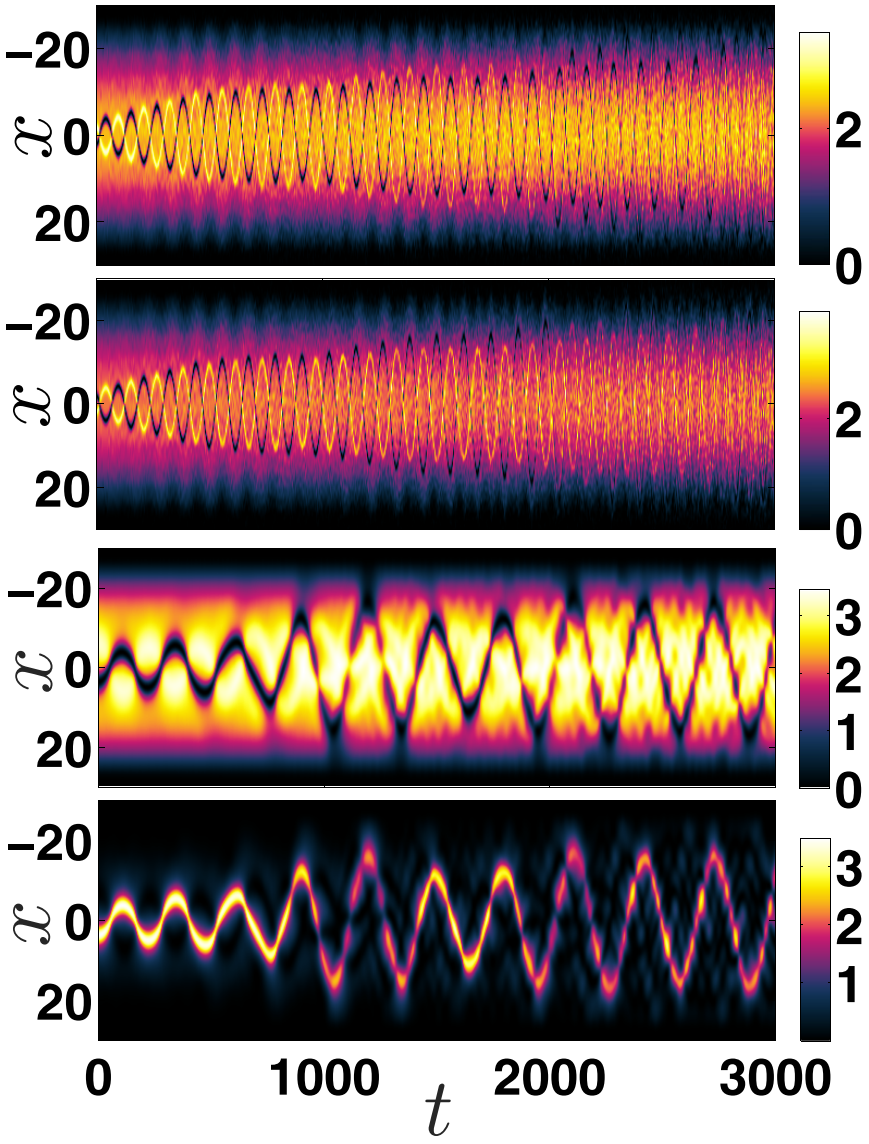

Figure 3.7.: Dynamics of two dark-antidark solitons with opposite magnetisation for $a_{12} = 60a_0$ (upper two panels) and $a_{12} = 96a_0$ (lower two panels). The first (third) panel shows the density of the first component, and the second (fourth panel) the mirrored density of the second component. The intra-component scattering lengths are $a_{11} = 100.4a_0$ and $a_{22} = 98.98a_0$. The quantities shown are in dimensionless units. Taken from Ref. [52].

3.2. Theoretical developments of dark solitons in single-component dipolar condensates

In this section, we review recent theoretical predictions for soliton bound states in single-component dipolar BECs in quasi-1D configurations.

While dark solitons repel each other in non-dipolar quasi-1D BECs, an axial trapping potential—which pushes the solitons toward the centre—can compensate for inter-soliton repulsion, allowing stationary states to form. Recent theoretical work by Pawłowski *et*

al. [34] and Bland *et al.* [35] predicted the formation of stationary states between two dark solitons in dipolar BECs, even without a trap along the tube axis.

3.2.1. Dipolar dark solitons

In Ref. [34], Pawłowski *et al.* showed that in quasi-1D BECs with dipolar atoms aligned perpendicular to the tube axis, the soliton's density dip acts as a hole, around which density modulations form due to the dipoles' head-to-tail attraction and side-by-side repulsion. These modulations induce long-range interactions between solitons, which depend on their separation and can be either attractive or repulsive. When the interaction are attractive, it can balance the repulsive local soliton-soliton interactions, allowing a bound state to form. To understand when the long-range interactions between solitons are attractive, one can examine the density profile of a single soliton. Around the soliton, density modulations (ripples) form with alternating high- and low-density regions. Introducing a second soliton into the system requires less energy in a low-density region than in a high-density one. Intriguingly, the authors found that placing the second soliton in a high-density region around the first soliton, with separations of Δx_{stat} can lead to stationary states of two dark solitons, as well as oscillatory bound states for separations close to Δx_{stat}.
Two bound states are shown in the lower panels of Fig. 3.8. The simulation A shows the dynamics of two black solitons with $\Delta x_{\mathrm{stat}}/L \approx 0.12$, where the repulsive force between the cores of the dark solitons and the attractive force due to the density modulations around the cores cancel. The two black solitons form a stationary state. Simulation B shows the same dynamics but with a larger initial separation between the two initially black solitons. The solitons accelerate towards each other until they collide and then move apart without swapping. Eventually, they reach a turning point where they are black again and then repeat the oscillation. One can measure the acceleration a_{sol} and use

$$a_{\mathrm{sol}} = F_{\mathrm{sol}}/m = -\frac{1}{m}\frac{dV_{\mathrm{sol}}}{dx}, \tag{3.3}$$

to calculate the inter-soliton potential V_{sol} by integrating over a_{sol} and choosing the integration constant such that $V_{\mathrm{sol}} \to 0$ for $\Delta x \to \infty$ [34]. The main panel of Fig. 3.8 shows such an inter-soliton potential V_{sol}. We can clearly see a minimum at position A, where we get the stationary bound state. Around this minimum we get oscillating bound states. For initially smaller separations the energy is above zero and the solitons move apart and escape the bound state [35].
Notice that in Fig. 3.8 the negative of the inter-soliton potential $-V_{\mathrm{sol}}/m$ vs the separation is plotted. This is done to account for the negative effective mass m^* of the soliton and to give an intuitive picture of a bound states oscillating around a minimum.[2]

[2] If we plot the inter-soliton potential V_{sol} without the minus sign, the solitons are oscillating around a maximum, which seems counter-intuitive. The negative effective mass m^* of the soliton causes the soliton to accelerate up the slope of the inter-soliton potential and thus towards a potential maximum. To make it more intuitive, Pawłowski *et al.* plot the inter-soliton potential $-V_{\mathrm{sol}}/m$.

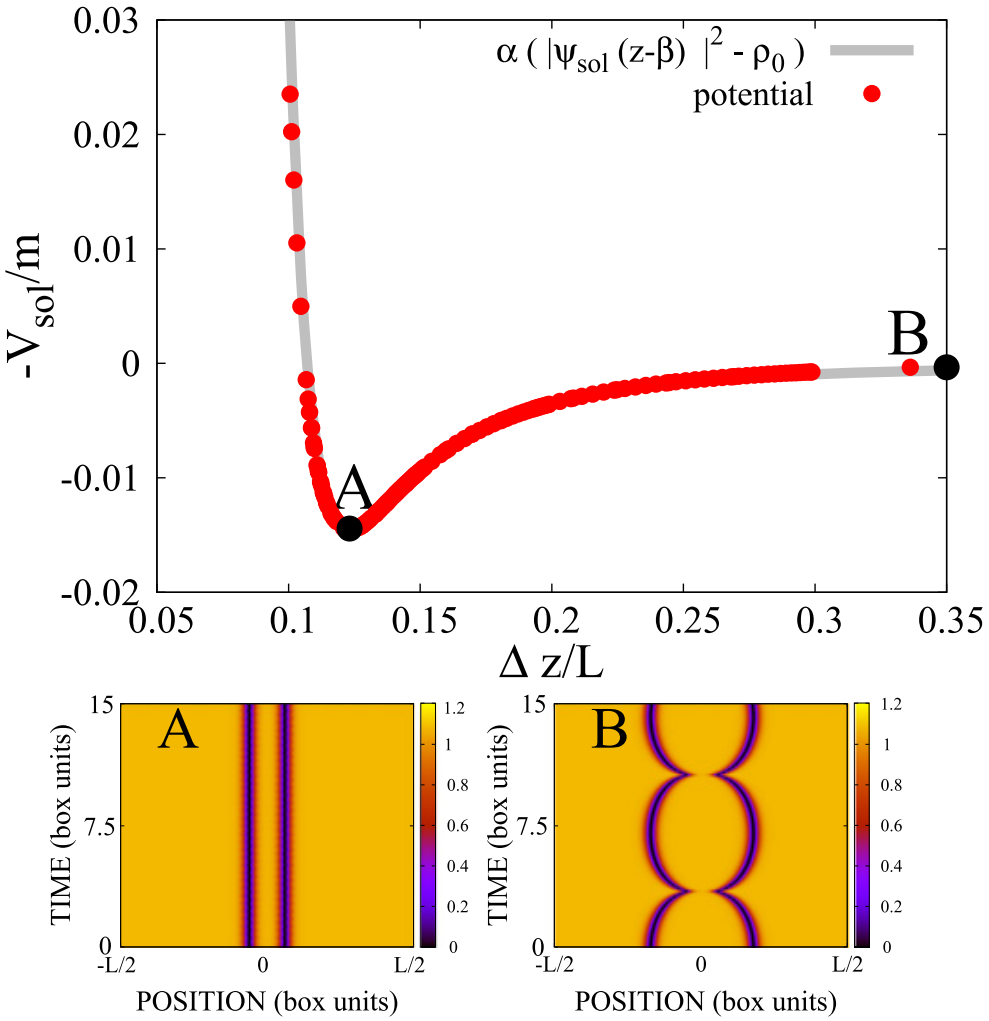

Figure 3.8.: Negative inter-soliton potential vs soliton separation in the main panel. Points A and B refer to the dynamics of two black solitons for the corresponding trajectories shown in the lower panels. Panel A shows a stationary state of two black solitons and B shows oscillatory motion of a bound state between two dark solitons. The quantities displayed are given in dimensionless units. L is the box length. Taken from [34].

3.2.2. Nonlocal interactions between dipolar dark solitons

Bland *et al.* [35] developed an alternative method for calculating the inter-soliton potential

$$V_{\mathrm{sol}}(\Delta x) = E_{\mathrm{tot}}(\Delta x) - E_0, \tag{3.4}$$

where $E_{\mathrm{tot}}(\Delta x)$ is the total energy of the system with two black solitons with separation Δx. E_0 is the energy of the system with two isolated black solitons.
Further, Bland *et al.* [35] predicted that bound states between two dark solitons behave like solitons in the sense that they can emerge unscathed from collisions with other bound states. Figure 3.9 shows collisions between two bound states moving with velocity (a) $v = 0.01c_s$ and (b) $v = 0.5c_s$, where c_s is the speed of sound. In Fig. 3.9 the bound states move slowly towards each other, while the solitons in the bound state oscillate slightly around Δx_{stat}.

The bound states collide and bounce off one another. After the collision the bound states recover their shape and dissipation is not visible. In Fig. 3.9(b) the bound states move fast and pass through one another. The outgoing bound states show no dissipation and exhibit a spatial displacement.

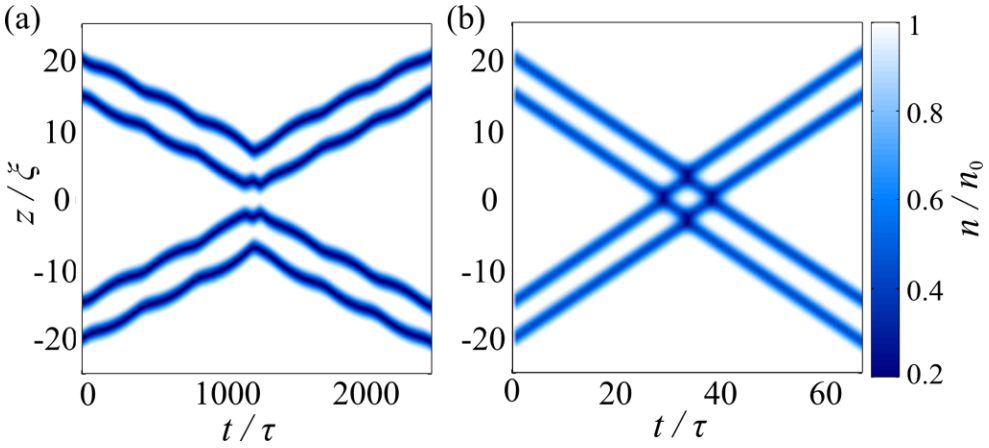

Figure 3.9.: Collisions between bound states with (a) $v = 0.01c_s$ and (b) $v = 0.5c_s$. The bound states emerge unscathed from the collisions in both cases. Taken from Ref. [35].

3.3. Motivation for thesis

The experiments [52, 59, 60], discussed in Sec. 3.1, have demonstrated the realisation of magnetic solitons and dark-antidark solitons in binary BECs with sodium and rubidium atoms. They established that these vector solitons pass through one another when colliding at high velocities, independent of their individual magnetisation. However, for slow-moving solitons with the same magnetisation, experiments were unable to verify whether they bounce off each other or pass through one another. Complementary theoretical work predicted the formation of bound states using solitons with opposite magnetisation (kink-antikink solitons [51], beating dark-dark solitons in the presence of an axial trapping potential [55, 56, 60, 83, 84] and Flemish strings [53]) and magnetic solitons with the same magnetisation (bound state between *sorted* solitons [60]).
In Sec. 3.2, we have seen that in dipolar condensates, dark solitons form density modulations around their cores, which lead to a non-trivial minimum in the inter-soliton potential. Around this minimum, dark solitons can form bound states, which themselves behave soliton-like, emerging unscathed from collisions with other bound states.
An overarching goal of this thesis is to investigate dark-antidark solitons in binary dipolar condensates and to analyse possible bound states. We first expand on existing theoretical work of dark-antidark solitons and in particular magnetic solitons in the miscible regime of non-dipolar binary condensates that are untrapped along the tube axis. This allows us to calculate the inter-soliton potential to elucidate the mechanisms and conditions for the formation of bound states. We find that solitons with opposite magnetisation attract,

while those with the same magnetisation repel. This makes bound states in binary BECs without an external potential possible only between solitons with opposite magnetisation. We analytically calculate the dissociation energy of the bound state and find that the oscillation period depends on the maximal soliton separation.
We then consider dark-antidark solitons in binary dipolar condensates, again in the miscible regime. We derive the dispersion relations for binary dipolar condensates. Intriguingly, we predict that the presence of a roton in the spin branch of the dispersion relation enables the formation of multiple bound states with distinct equilibrium separations for a given dark-antidark soliton pair. We find that some of these bound states resemble those in non-dipolar binary condensates, others resemble bound states between dark solitons in single-component dipolar condensates, while others have novel characteristics.
Finally, we consider collisions between dark-antidark solitons. We find that slow-moving dark-antidark solitons in the non-dipolar case either bounce off each other or pass through one another, depending on their relative magnetisation, while in the dipolar case, slow-moving soliton always bounce, independent of their magnetisation. For collisions between bound states, we find that they either bounce, similar to dark-antidark solitons with the same magnetisation, or collide inelastically, sometimes resulting in the decay of the initial bound states into two unbound dark-antidark solitons and a newly formed bound state.

4. Gross-Pitaevskii equations for elongated binary condensates

In this chapter, we outline the derivation of the coupled quasi-1D Gross-Pitaevskii equations (GPEs) for binary BECs in cigar-shaped geometries, incorporating dipole-dipole interactions (DDIs). This formulation provides a robust theoretical framework for analysing both dark-antidark solitons and magnetic solitons, both analytically and numerically.
We begin by introducing the order parameter, which characterises the condensate using a classical field approach. By leveraging the order parameter, we use the Hamiltonian described in Sec. 2.2 and Sec. 2.4 to derive the coupled GPEs for a binary dipolar condensates in three dimensions. Subsequently, we impose a cylindrical confinement and analytically integrate out the radial dimensions, ultimately obtaining the coupled quasi-1D GPEs.

4.1. Order parameter

The order parameter is a useful tool for describing atoms in the condensate state. The order parameter Ψ approximates the field operator with a classical field, simplifying calculations significantly. We can rewrite the field operator (2.6) as

$$\hat{\Psi}(\mathbf{r},t) = \Phi_0(\mathbf{r},t)\hat{a}_0 + \delta\hat{\Psi}(\mathbf{r},t), \tag{4.1}$$

where $\delta\hat{\Psi}(\mathbf{r},t) = \sum_{i\neq 0}\Phi_i(\mathbf{r},t)\hat{a}_i$ describes the excited states. Applying $\hat{a}_0$ on the condensate state $|N_0\rangle$ annihilates one particle, yielding

$$\hat{a}_0\,|N_0\rangle = \sqrt{N_0}\,|N_0-1\rangle\,. \tag{4.2}$$

However, for a BEC, where $N_0 \approx N \gg 1$, we find $|N_0\rangle \approx |N_0-1\rangle$, allowing the Bogoliubov approximation, $\Phi_0\hat{a}_0 \to \Psi_0$, to be made [71]. The classical field $\Psi_0(\mathbf{r},t) = |\Psi_0(\mathbf{r},t)|e^{i\phi(\mathbf{r},t)}$ is called the order parameter and is fully characterised by the absolute value $|\Psi_0(\mathbf{r},t)| = \left|\Phi_0\sqrt{N}\right|$ and the phase $\phi(\mathbf{r},t)$. Within the approximation, the field operator becomes

$$\hat{\Psi}(\mathbf{r},t) = \Psi_0(\mathbf{r},t) + \delta\hat{\Psi}(\mathbf{r},t). \tag{4.3}$$

At zero temperature and for weak interactions, the excitations can be neglected, allowing us to make the replacement $\hat{\Psi}(\mathbf{r},t) \to \Psi_0(\mathbf{r},t)$.
In the following, we omit the subscript zero from Ψ_0 for better readability.

4.2. Coupled 3D Gross-Pitaevskii equations

In the presence of the order parameter, the GPE can be extremely useful, providing a mean-field description of many-particle problems at zero temperature [9]. Here, we derive the 3D coupled GPEs for binary dipolar BECs from the Lagrangian density following Ref. [95], however, there are other methods for deriving the 3D coupled GPEs (see, *e.g.*, Refs. [9, 96, 97]).

For a binary dipolar BEC polarised along $\mathbf{e}_1$, described by the wavefunctions $\Psi_1(\mathbf{r},t)$ and $\Psi_2(\mathbf{r},t)$ with equal masses $m_1 = m_2 = m$ at zero temperature, the mean-field Lagrangian density is given by

$$\mathcal{L} = \sum_{i=1}^{2}\left[\frac{i\hbar}{2}\left(\Psi_i^*\partial_t\Psi_i - \Psi_i\partial_t\Psi_i^*\right) - \mathcal{H}_i\right], \tag{4.4}$$

where we omit the dependence on $(\mathbf{r},t)$ for all quantities for readability. The Hamiltonian density $\mathcal{H}_i$ of component i can be derived from the Hamiltonian (2.22), with the addition of the pseudo-potential term $\sum_j \Phi_{ij}^{\mathrm{3D}}(\mathbf{r})/2$ for the DDIs, using the Bogoliubov approximation, and is given by

$$\mathcal{H}_i = \frac{\hbar^2}{2m}|\nabla\Psi_i|^2 + V(\mathbf{r})|\Psi_i|^2 + \sum_{j=1}^{2}\frac{g_{ij}}{2}|\Psi_j|^2|\Psi_i|^2 + \sum_{j=1}^{2}\frac{\Phi_{ij}^{\mathrm{3D}}(\mathbf{r},t)}{2}|\Psi_i|^2, \tag{4.5}$$

where $g_{ij} = 4\pi\hbar^2 a_{ij}/m$ is the coupling constant and $V(\mathbf{r}) = \frac{m}{2}(\omega_x^2x^2 + \omega_y^2y^2 + \omega_z^2z^2)$ is the external potential, with the confinement $\omega_{x,y,z}$ in the x, y and z directions. Here, a_{ij} is the three dimensional s-wave scattering length describing interactions between particles from component i and j. The term describing the DDI is given by

$$\Phi_{ij}^{\mathrm{3D}}(\mathbf{r},t) = \int d\mathbf{r}'\frac{3g_{ij}^{dd}}{4\pi}\left[\frac{1-3\cos^2\vartheta}{|\mathbf{r}-\mathbf{r}'|^3}\right]|\Psi_j(\mathbf{r}',t)|^2, \tag{4.6}$$

where $g_{ij}^{dd} = 4\pi\hbar^2 a_{ij}^{dd}/m$ is the dipolar coupling constant and ϑ is the angle between $\mathbf{e}_1$ and $\mathbf{r}-\mathbf{r}'$. Here, $a_{ij}^{dd} = m\mu_0\mu_i\mu_j/12\pi\hbar^2$ is the dipole length describing interactions between particles from component i and j with permanent magnetic moment μ_i and μ_j, respectively. Note that in Eq. (4.5), we have assumed, that the external trap acts equally on both components.

We can derive the coupled GPEs by solving the Euler–Lagrange equations

$$\frac{\partial\mathcal{L}}{\partial\Psi_i^*} - \frac{\partial}{\partial t}\frac{\partial\mathcal{L}}{\partial(\partial_t\Psi_i^*)} - \nabla\frac{\partial\mathcal{L}}{\partial(\nabla\Psi_i^*)} = 0. \tag{4.7}$$

Inserting the Lagrangian density (4.4) into the Euler-Lagrange equations (4.7) and solving for $i = \{1,2\}$, we obtain the coupled 3D GPEs [98, 99]

$$\begin{aligned}
i\hbar\partial_t\Psi_1(\mathbf{r},t) &= \left[-\frac{\hbar^2\nabla^2}{2m} + V(\mathbf{r}) + \sum_j g_{1j}n_j^{\mathrm{3D}}(\mathbf{r},t) + \sum_j \Phi_{1j}^{\mathrm{3D}}(\mathbf{r},t)\right]\Psi_1(\mathbf{r},t),\\
i\hbar\partial_t\Psi_2(\mathbf{r},t) &= \left[-\frac{\hbar^2\nabla^2}{2m} + V(\mathbf{r}) + \sum_j g_{2j}n_j^{\mathrm{3D}}(\mathbf{r},t) + \sum_j \Phi_{2j}^{\mathrm{3D}}(\mathbf{r},t)\right]\Psi_2(\mathbf{r},t),
\end{aligned} \tag{4.8}$$

where $n_j^{3D}(\mathbf{r}) = |\Psi_j(\mathbf{r})|^2$ is the 3D density of the j-th component at position $\mathbf{r}$. We can define the 3D Gross-Pitaevskii (GP) operator for the component i as

$$\mathcal{G}_i^{3D} = \left[-\frac{\hbar^2 \nabla^2}{2m} + V(\mathbf{r}) + \sum_j g_{ij} n_j^{3D}(\mathbf{r}, t) + \sum_j \Phi_{ij}^{3D}(\mathbf{r}, t) \right], \tag{4.9}$$

and rewrite the coupled GPEs (4.8) as

$$i\hbar \partial_t \Psi_i(\mathbf{r}, t) = \mathcal{G}_i^{3D} \Psi_i(\mathbf{r}, t). \tag{4.10}$$

4.3. Coupled quasi-1D Gross-Pitaevskii equations

Since solitons are generally stable only in the quasi-1D regime, we consider elongated binary dipolar BECs that are tightly confined in the transverse (radial) plane ($y - z$) and weakly confined along the longitudinal direction. We adapt the procedure outlined in Ref. [100] for deriving the quasi-1D GPE for single-component condensates to our two-component system, incorporating the additional coupling terms between components (see also Refs. [101–103]). Since the binary dipolar condensates are tightly trapped in the $y - z$ plane, excited states in this direction are effectively frozen out. This allows us to approximate the solutions to be of separable form, $\Psi_i(\mathbf{r}, t) = \psi_i(x, t)\phi(y, z)$, where $\psi_i(x, t)$ is the wavefunction along the tube axis and $\phi(y, z)$ is the wavefunction in the radial direction, given by isotropic Gaussians

$$\phi(y, z) = \frac{\mathrm{e}^{-(y^2+z^2)/2l^2}}{\sqrt{\pi} l}. \tag{4.11}$$

Here, $l = \sqrt{\frac{\hbar}{m\omega_\rho}}$ is the characteristic length of the radial trap. Note that $\int dydz |\phi|^2 = 1$ holds.

We can reduce the dimensionality of the coupled GPEs (4.8) by analytically integrating out the transverse dimensions, yielding the quasi-1D GP operators

$$\mathcal{G}_i^{q1D} = \int dydz\, \phi^*(y, z) \mathcal{G}_i^{3D} \phi(y, z), \tag{4.12}$$

and the coupled quasi-1D GPEs

$$i\hbar \partial_t \psi_i = \mathcal{G}_i^{q1D} \psi_i. \tag{4.13}$$

Calculating $\mathcal{G}_i^{q1D}$ is, in principle straight forward, as we can integrate the terms of $\mathcal{G}_i^{3D}$ separately.[1] The first term in Eq. (4.12), the kinetic energy term, reduces to

$$\begin{aligned} -\int dydz\, \phi^*(y, z) \frac{\hbar^2 \nabla^2}{2m} \phi(y, z) &= -\frac{\hbar^2}{2m} \left(\partial_x^2 + \int dydz\, \phi^*(y, z)(\partial_y^2 + \partial_z^2)\phi(y, z) \right) \\ &= -\frac{\hbar^2}{2m} \partial_x^2 + \frac{\hbar^2}{2ml^2} \end{aligned} \tag{4.14}$$

[1] The calculations for the non-dipolar terms are presented in detail in Appendix A.1, using the general ansatz of non-isotropic Gaussians in the radial directions.

The external potential reduces to

$$\begin{aligned}\int dydz\,\phi(y,z)^* V(\mathbf{r})\phi(y,z) &= \frac{1}{2}m\left(\omega_x^2 x^2 + \int dydz\,\omega_\rho^2\left(y^2+z^2\right)|\phi(y,z)|^2\right)\\ &= \frac{1}{4}m\left[2\omega_x^2 x^2 + 2\omega_\rho l^2\right],\end{aligned} \tag{4.15}$$

and the contact interactions reduce to

$$\sum_j \int dydz\,\phi^*(y,z) g_{ij}|\phi_j(y,z)|^2|\psi_j(x,t)|^2\phi(y,z) = \sum_j \frac{g_{ij}}{2\pi l^2}|\psi(x,t)|^2. \tag{4.16}$$

Integrating over the DDI term is more challenging. We consider the integral with the DDI term in momentum space. Assuming the dipoles are aligned along the y axis, we obtain

$$\Phi_{ij}^{1\mathrm{D}}(x,t) = \int dydz\,\mathcal{F}_{\mathbf{r}}^{-1}\left\{\hat{U}_{ij}^{3\mathrm{D}}(\mathbf{k})\mathcal{F}_{k_x}\left[|\psi_j(x,t)|^2\right]\mathcal{F}_{k_y,k_z}\left[|\phi(y,z)|^2\right]\right\}, \tag{4.17}$$

where

$$\mathcal{F}_\beta\{f(\alpha)\} = \hat{f}(\beta) = \frac{1}{\sqrt{2\pi}}\int_{-\infty}^{\infty} f(\alpha)e^{-i\alpha\beta}d\alpha, \tag{4.18}$$

is the Fourier transform, and

$$\mathcal{F}_\alpha^{-1}\{\hat{f}(\beta)\} = f(\alpha) = \frac{1}{\sqrt{2\pi}}\int_{-\infty}^{\infty} \hat{f}(\beta)e^{i\alpha\beta}d\beta, \tag{4.19}$$

is the inverse Fourier transform. Note that α and β can be vectors. The term $\hat{U}_{ij}^{3\mathrm{D}}(\mathbf{k})$ is given by

$$\hat{U}_{ij}^{3\mathrm{D}}(\mathbf{k}) = \mathcal{F}_{\mathbf{k}}\left\{\frac{3g_{ij}^{dd}}{4\pi r^3}\left[1-\frac{3y^2}{r^2}\right]\right\} = g_{ij}^{dd}\left(3\frac{k_y^2}{k^2}-1\right), \tag{4.20}$$

where $r = |\mathbf{r}|$ and $k = |\mathbf{k}|$. Inserting the Gaussian ansatz (4.11) into Eq. (4.17) yields

$$\Phi_{ij}^{1\mathrm{D}}(x,t) = \mathcal{F}_x^{-1}\left\{\hat{U}_{ij}(k_x)\mathcal{F}_{k_x}\left[|\psi_j(x,t)|^2\right]\right\}, \tag{4.21}$$

where

$$\hat{U}_{ij}(k_x) = \frac{g_{ij}^{dd}}{4\pi l^2}\left[1-3Q^2e^{Q^2}\mathrm{E}_1(Q^2)\right], \tag{4.22}$$

with $Q^2 = \frac{1}{2}k_x^2 l^2$ for dipoles polarised radial to the tube axis. Here, E_1 is the exponential integral defined for real non-zero values by

$$\mathrm{E}_1(x) = \int_x^\infty \frac{e^{-t}}{t}dt. \tag{4.23}$$

Collecting terms, we find

$$\mathcal{G}_i^{\mathrm{q1D}} = -\frac{\hbar^2}{2m}\partial_x^2 + \frac{1}{2}m\omega_x^2 x^2 + \sum_j \frac{g_{ij}n_j^{1\mathrm{D}}(x,t)}{2\pi l^2} + \sum_j \Phi_{ij}^{1\mathrm{D}}(x,t) + \mathcal{E}_i, \tag{4.24}$$

where $n_{ij}^{\mathrm{1D}}(x,t) = |\psi_j(x,t)|^2$ and

$$\mathcal{E}_i = \frac{\hbar^2}{2ml^2} + \frac{1}{4}ml^2\left(\omega_y^2 + \omega_z^2\right), \tag{4.25}$$

is a constant energy shift due to the radial confinement. In this work, we assume no trapping along the x axis ($\omega_x \to 0$) and omit all 1D superscripts and (x,t), when the context is clear, for readability. Further, we omit $\mathcal{E}_i$, as we are only interested in relative energies upon which $\mathcal{E}_i$ has no influence.
Inserting Eq. (4.24) into Eq. (4.13), gives the coupled quasi-1D GPEs

$$i\hbar\partial_t\psi_i = \left(-\frac{\hbar^2}{2m}\partial_x^2 + \sum_j \frac{g_{ij}n_j}{2\pi l^2} + \sum_j \Phi_{ij}\right)\psi_i. \tag{4.26}$$

For stationary states, the time evolution for ψ_i is governed by the chemical potential μ_i^s, and Eq. (4.26) reduces to

$$\mu_i^s\psi_i = \left(-\frac{\hbar^2}{2m}\partial_x^2 + \sum_j \frac{g_{ij}n_j}{2\pi l^2} + \sum_j \Phi_{ij}\right)\psi_i., \tag{4.27}$$

where μ_i^s corresponds to an eigenvalue of $\mathcal{G}_i^{\mathrm{q1D}}$. The chemical potential can be evaluated as

$$\mu_i^s = \frac{\int dx \psi_i^\dagger \mathcal{G}_i^{\mathrm{q1D}}\psi_i}{\int dx |\psi_i|^2}, \tag{4.28}$$

which yields

$$\mu_{i,0}^s = \frac{1}{2\pi l^2}\sum_j g_{ij}n_0^{(j)} + \frac{1}{4\pi l^2}\sum_j g_{ij}^{dd}n_0^{(j)}. \tag{4.29}$$

for a homogeneous density ($n_0^{(i)} = \left|\psi_0^{(i)}\right|^2 = N_i/L$).
The total energy of the system is given by the energy functional

$$E = \sum_i \int dx \psi_i^\dagger \left(-\frac{\hbar^2}{2m}\partial_x^2 + \frac{1}{2}\sum_j \frac{g_{ij}n_j}{2\pi l^2} + \frac{1}{2}\sum_j \Phi_{ij}\right)\psi_i. \tag{4.30}$$

5. Numerical methods

In this chapter, we consider the numerical methods we use to find stationary states and analyse dynamics. First, we transform the coupled Gross-Pitaevskii equations (4.26) from real to computational units, which reduce numerical errors during simulations. Then, we discuss the numerical methods for imprinting and evolving pairs of dark-antidark solitons.

5.1. Solving the coupled Gross-Pitaevskii equations

This section reviews the numerical methods we use to solve the coupled GPEs (4.26). For more information, the interested reader is referred to, *e.g.*, Ref. [104].
For numerical implementation, it is convenient to write the coupled GPEs (4.26) in dimensionless units of length $x_0 = \sqrt{\hbar/m\omega_0}$ and energy $E_0 = \hbar\omega_0$, and normalising the wavefunctions ψ_1 and ψ_2 to $\int dx|\psi_i|^2 = 1$. We multiply the coupled GPEs (4.26) by $\frac{\sqrt{x_0}}{E_0\sqrt{N_i}}$, yielding

$$i\partial_{\tilde{t}}\tilde{\psi}_i = \left(\frac{1}{2}\partial_{\tilde{x}}^2 + \sum_j \tilde{c_{ij}}\tilde{n}_j + \sum_j \tilde{\Phi}_{ij}\right)\tilde{\psi}_i, \tag{5.1}$$

where we introduce the dimensionless time $\tilde{t} = t\omega_0$, space $\tilde{x} = x/x_0$, wavefunctions $\tilde{\psi}_i = \psi_i\sqrt{x_0/N_i}$, density $\tilde{n}_j = \left|\tilde{\psi}_j\right|^2$, contact coupling constant

$$\tilde{c}_{ij} = \frac{2a_{ij}x_0N_j}{l^2} \tag{5.2}$$

and the DDI term

$$\tilde{\Phi}_{ij}(\tilde{x}) = \mathcal{F}_{\tilde{x}}^{-1}\left\{\tilde{U}_{ij}(k_{\tilde{x}})\mathcal{F}_{\tilde{x}}\left[\tilde{n}_j\right]\right\} \tag{5.3}$$

with

$$\tilde{U}_{ij}(k_{\tilde{x}}) = \frac{a_{ij}^{dd}x_0N_j}{l^2}\left[1 - 3Q^2e^{Q^2}\mathrm{E}_1(Q^2)\right]. \tag{5.4}$$

The energy in dimensionless units is given by

$$\tilde{E} = \frac{E}{E_0} = \int dx\tilde{\psi}^\dagger\left(\frac{1}{2}\partial_{\tilde{x}}^2 + \frac{1}{2}\sum_j \tilde{c}_{ij}\tilde{n}_j + \frac{1}{2}\sum_j \tilde{\Phi}_{ij}\right)\tilde{\psi}_i. \tag{5.5}$$

We numerically solve the dimensionless coupled GPEs (5.1) using a fourth-order Runge-Kutta method in a system of length L with periodic boundary conditions. The fourth-order Runge-Kutta method is a well-known iterative technique for approximating solutions to initial value problems involving non-linear equations. We obtain the ground state and stationary state solutions via imaginary time evolution and investigate the dynamics through real-time evolution.

5.2. Generating magnetic solitons and dark-antidark solitons

The phase and density profiles of isolated magnetic solitons are given in Eqs. (2.41) and (2.42). However, in the following chapter, we focus on the dynamics between finitely separated magnetic solitons and dark-antidark solitons, where their density profiles can vary significantly from Eq. (2.41).
In this section, we describe the methods used to generate finitely separated magnetic and dark-antidark solitons. We begin by introducing the imprinting method for stationary magnetic soliton pairs (SMSPs), which allows us to study soliton interactions and bound states. Next, we introduce Son-Stephanov phase domain walls (PDWs) and their imprinting method, which also enables the investigation of soliton interactions and bound states. Finally, we outline the method for creating finitely separated moving solitons to examine collisions between single solitons, and between bound states. Both the SMSP method and the method for creating moving magnetic solitons can also be used to create dark-antidark solitons.

5.2.1. Stationary magnetic soliton pairs (SMSPs)

Imprinting stationary magnetic soliton pairs onto the condensates, generates two stationary magnetic solitons with separation $\Delta x = x_2 - x_1$. We imprint a phase jump of π at position x_1 in the first component and a phase-jump of π at x_2 in either the first or second component, depending on whether we are considering the dynamics between magnetic solitons with the same or opposite magnetisation. This process is repeated at each time step of the imaginary time evolution. The phase jump at x_1 creates a density dip in the first component, while the second component develops a density maximum at the same position. Simultaneously, the same occurs at x_2, although the components can be flipped if the magnetisation of the second soliton is opposite to that of the first. Eventually, the density profile stabilises, resulting in two initially stationary solitons. We have confirmed that this method can also produce time stationary-state solutions. For example, when two solitons are positioned at their preferred bound-state separations, we find that such states remain unchanged during real-time evolution.
An advantage of this method is that it allows convergence to the target state with arbitrary precision. However, this method is only feasible for stationary magnetic solitons, since $v \neq 0$ solitons would require a non-trivial phase profile to be printed at every time step. During imaginary time evolution, the stationary solitons remain fixed. However, in Sec. 6.1, we show that, in real time, the initially stationary solitons interact in a finite-sized system and may begin to move. This method works also for producing initially stationary dark-antidark solitons in non-dipolar and binary dipolar BECs.

5.2.2. Son-Stephanov phase domain walls (PDWs)

This subsection reviews some general features of Son-Stephanov phase domain walls in binary BECs. For more information, the interested reader is referred to, *e.g.*, Ref. [86, 105]. In a two-component non-dipolar system with two different hyperfine spin states and a small coupling drive between them with Rabi frequency Ω, the states can exhibit a phenomenon known as a Son-Stephanov phase domain wall, or simply a phase domain wall (PDW). The relative phase ϕ_A [see Eq. (2.38)] of a PDW changes by 2π and is given by

$$\phi_A = 4 \arctan e^{x/b}, \tag{5.6}$$

where b is the characteristic width of the relative phase domain wall, which depends on Ω. The energy of a single PDW is

$$E_{PDW} = 2n\hbar c_s \xi_s / b, \tag{5.7}$$

where c_s is the spin speed of sound and ξ_s is the spin healing length (see Sec. 2.3.2). PDWs can be meta-stable states for $0 < \Omega < \Omega_c$, where Ω_c is the critical Rabi frequency below which the 2π phase jump forms a minimum in the energy of the system.
In non-dipolar binary BECs without coupling ($\Omega = 0$), PDWs with width b are unstable and decay into two magnetic solitons with opposite magnetisation, moving in opposite directions. The total energy of both moving solitons is given by Eq. (5.7). This method for creating solitons is analogous to the imprinting methods used in Refs. [59, 60] for generating magnetic solitons (see also Sec. 3.1).

Imprinting PDWs

The method of imprinting PDWs creates two moving magnetic solitons positioned on top of each other. Since we evolve the system with Eq. (5.1), it is practical to imprint Eq. (5.6) divided by 2 on the first component and the negative of this on the second component. This creates a phase profile as shown in Fig. 3.1. This imprinting method assumes a constant total density. To soften this assumption, we allow for imaginary time evolution, during which a density dip can form in both components at the centre of the PDW. Without the imaginary time evolution, the PDW method produces strong phonon excitations for small widths $b \ll \xi_s$ during real time evolution. The advantage of the PDW method compared to the SMSP method is that it allows us to cover a wider range of total energies.

Semi-analytic PDWs

Instead of evolving the PDW with the GPE, we can also consider the coupled differential equations (2.40) and solve them for an initial phase distribution of a PDW with width b. For the evolution, we use a simple forward Euler method, which is the first-order Runge-Kutta method. Similar to the evolution with the GPE, the PDW produces two counter-propagating magnetic solitons with opposite magnetisation, initially positioned on top of each other.

5.2.3. Moving magnetic solitons

We generate moving magnetic solitons by imprinting an almost stationary magnetic soliton and then applying imaginary time evolution until the soliton reaches the desired magnetisation s. We can find the velocity of the magnetic soliton via Eq. (3.1). This method also works for generating moving dark-antidark solitons in both non-dipolar and dipolar binary BECs.

6. Results: Dynamics and bound states of solitons in binary BECs

In this chapter, we analyse the interactions between magnetic solitons in non-dipolar binary BECs, and dark-antidark solitons in binary dipolar condensates.
In Sec. 6.1, we consider magnetic solitons and find a non-trivial interaction between them, which is either attractive or repulsive depending on their relative magnetisation. We calculate the inter-soliton potentials and find that magnetic solitons with opposite magnetisation can form bound states, whereas those with the same magnetisation do not. We analytically calculate the dissociation energy of the bound states and numerically determine their oscillation period. Furthermore, we extend our investigation to dark-antidark solitons in non-dipolar binary BECs with imbalanced components, finding that their interactions are qualitatively similar to those of magnetic solitons.
In Sec. 6.2, we consider dark-antidark solitons in dipolar-nondipolar condensate mixtures. We derive the dispersion relations of elementary excitations in dipolar-nondipolar condensate mixtures and find that, in the presence of a spin roton, dark-antidark solitons exhibit strong spin-density modulations around their core structure. We again calculate the inter-soliton potential and find that these density modulations create energetically (un)favourable separations. As a result, we identify multiple bound states with distinct equilibrium separations for a given dark-antidark soliton pair.
In Sec. 6.3, we consider the collision between magnetic solitons in non-dipolar binary BECs, and dark-antidark solitons in dipolar-nondipolar condensate mixtures. We find that slowly moving magnetic solitons with the same magnetisation bounce off each other, whereas those with opposite magnetisation pass through one another. In the case of binary dipolar BECs, we see that slowly moving dark-antidark solitons bounce, independent of their magnetisation. Furthermore, we consider collisions between magnetic soliton bound states and find that they can collide elastically, behaving soliton-like, or inelastically, where sometimes only a single bound state remains. The elasticity of the collision is determined primarily by the relative oscillation phase between the bound states.
In the following, we omit the terms magnetic solitons and dark-antidark solitons, referring to them simply as solitons whenever the context is clear.

6.1. Magnetic soliton bound states in binary BECs with contact interactions

In this section, we explore the dynamics of magnetic solitons in non-dipolar binary BECs with balanced components ($n_0^{(1)} = n_0^{(2)} = n_0 = N/L$ and $g_{11} = g_{22}$). At the end of this section, we extend the results to dark-antidark solitons in non-dipolar binary BECs with imbalanced components.

6.1.1. Dynamics of initially stationary magnetic soliton pairs

To consider dynamics between multiple solitons, it is useful to introduce the reduced spin density (magnetisation distribution)

$$s(x) = \frac{n_1(x)}{n_{1,\,\mathrm{max}}} - \frac{n_2(x)}{n_{2,\,\mathrm{max}}}. \tag{6.1}$$

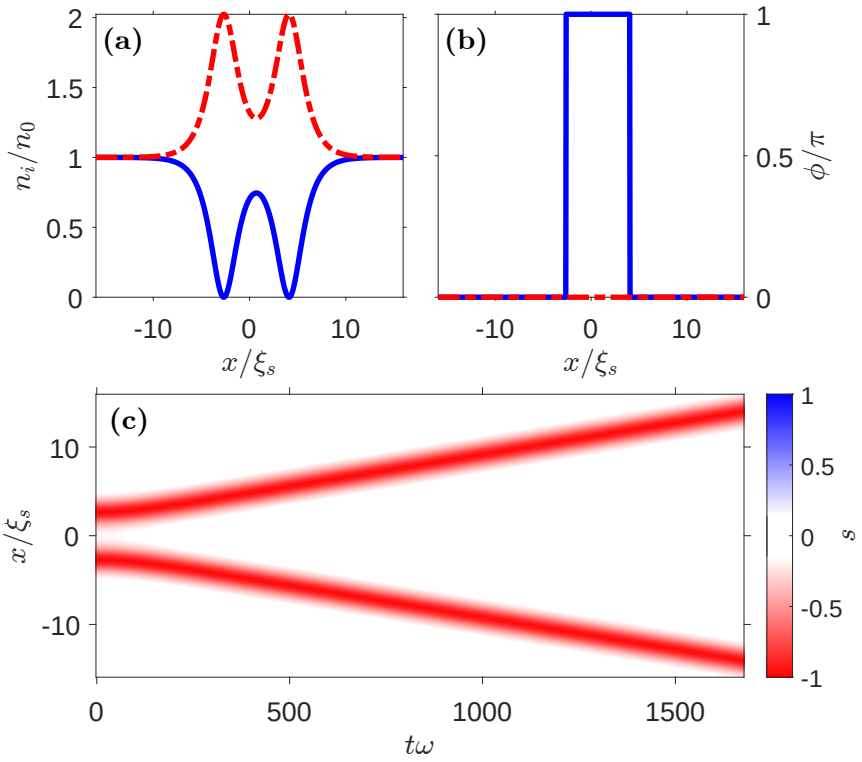

Figure 6.1.: Dynamics of two $s_{1,2} = -1$ solitons imprinted at $x_1 = -2.68\xi_s$ and $x_2 = 2.68\xi_s$. (a) The density profile, normalised to the average 1D density n_0 with component 1 (2) shown as blue (red), and (b) phase profile of the two solitons at $t = 0$. (c) Real time evolution of the reduced spin density [see Eq. (6.1)]. It shows the two solitons moving apart. Parameters: average integrated density per component $n_0 = N/2L = 50\,\mu\mathrm{m}^{-1}$; total particle number $N = 3000$; interactions $\{a_{11}, a_{12}, a_{22}\} = \{100, 95, 100\}\,a_0$; radial confinement $\omega = 2\pi \times 2667\,\mathrm{Hz}$; and spin healing length $\xi_s = 0.4703\,\mu\mathrm{m}$.

First, we consider the dynamics of two initially stationary solitons with the same magnetisation $s_{1,2} = -1$ [see Eq. (2.43)]. Note that the dynamics of two $s_{1,2} = 1$ solitons are identical due to the presence of balanced components. Figure 6.1(a) shows the initial density distribution of the $s_{1,2} = -1$ solitons with initial separation $\Delta x = 5.36\xi_s$. Figure 6.1(b) shows that both solitons exhibit a phase jump of π in the first component across each soliton's centre, while the phase of the second component remains constant. Without any interaction between the solitons, we would expect them to remain stationary. However, the dynamics in Fig. 6.1(c) show that the solitons repel each other. Once the solitons move, the phase gradient of the solitons becomes less sharp in the first component and a small phase gradient appears in the second component (not shown). The two solitons eventually move apart at a constant velocity.

On the other hand, we consider the dynamics of two solitons with opposite magnetisation. Figure 6.2(a) shows the initial density profile of these solitons, with the initial separation between the two solitons equal to that in Fig. 6.1. The phase profile in 6.2(b) shows a phase jump of π in each component. The dynamics in Fig. 6.2(c) show the solitons initially accelerating towards each other, passing through one another, and then decelerating. The solitons reach a turning point, where the density profiles resemble those in Fig. 6.2(a) but with mirrored magnetisations. The solitons continue to oscillate through each other, forming an excited bound state.

The interactions between the solitons that we see in this section are for initially stationary solitons. However, for initially moving solitons, the dynamics can be quite different. We explore this further in Sec. 6.3.

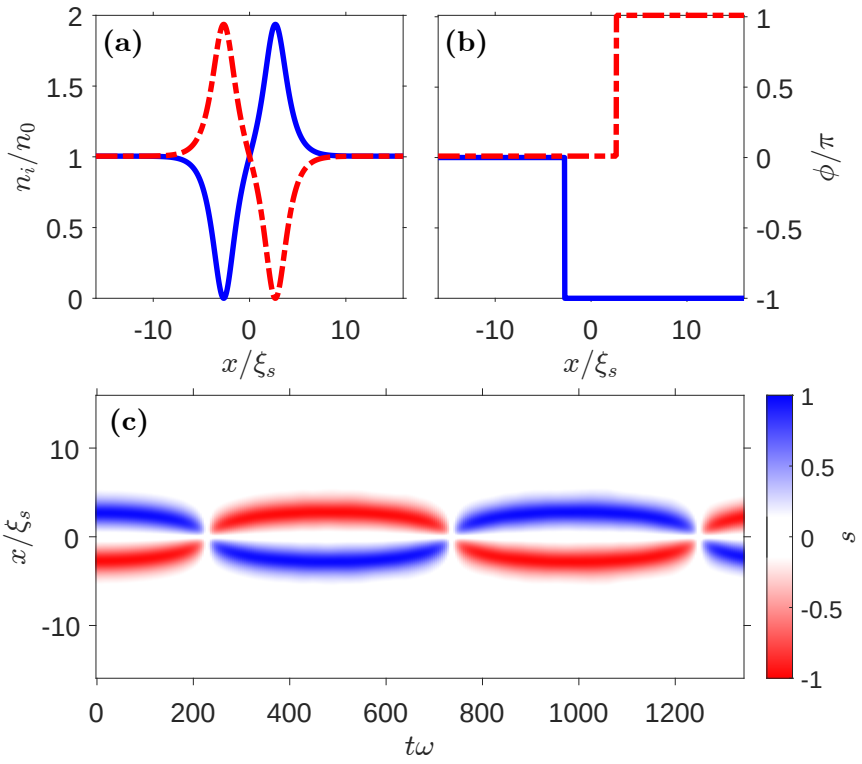

Figure 6.2.: Dynamics of a $s_1 = -1$ and a $s_2 = 1$ soliton imprinted at $x_1 = -2.68\xi_s$ and $x_2 = 2.68\xi_s$. (a) The density profile, normalised to the average 1D density n_0 with component 1 (2) shown as blue (red), and (b) phase profile of the two solitons at $t = 0$. (c) Real time evolution of the reduced spin density [see Eq. (6.1)]. It shows the two solitons oscillating through each other. Same parameters as in Fig. 6.1.

6.1.2. Inter-soliton potential

To determine whether the interactions between the solitons are attractive or repulsive, we consider the inter-soliton potential V_ν.The potential between solitons can be determined as

$$V_\nu = E_\nu(\Delta x) - E_{\text{2MS}}, \tag{6.2}$$

where $E_\nu(\Delta x)$ is the total energy of the system with two solitons at position x_1 and x_2, $\Delta x = x_2 - x_1$ is the separation of the solitons, and E_{2MS} is the energy of the system with two isolated solitons, which is independent of the relative magnetisations of the solitons. The relative magnetisation is defined as

$$\nu = s_1 s_2, \tag{6.3}$$

where s_i is the magnetisation of the i-th soliton [see Eq. (2.43)]. The relative magnetisation between two stationary solitons is given by $\nu = 1$ for two solitons with the same magnetisation and $\nu = -1$ for those with opposite magnetisation.
Figure 6.3(a) shows the inter-soliton potential V_1. The graph shows a minimum for $\Delta x = 0$

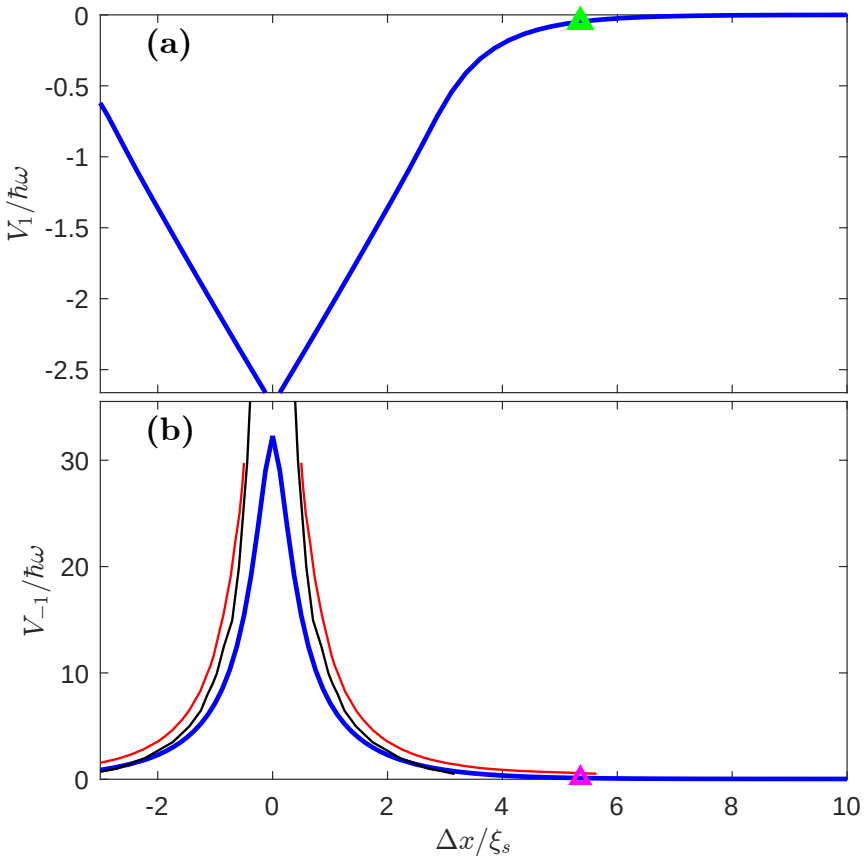

Figure 6.3.: Inter-soliton potential versus the soliton separation for two solitons with (a) the same magnetisation ($\nu = 1$) and (b) opposite magnetisation ($\nu = -1$). The potential exhibits a minimum (maximum) for $\nu = 1$ ($\nu = -1$) at $\Delta x = 0$, where the solitons are superimposed. The initial states for the dynamics shown in Fig. 6.1 and Fig. 6.2, with $\Delta x = 5.36\xi_s$, are marked as green and pink triangles in (a) and (b) respectively. The blue curves in (a) and (b) are generated by the SMSP method. The red curve in (b) represents the potential generated by the PDW method, and the black line corresponds to the semi-analytic PDW method (see main text). Same parameters as in Fig. 6.1.

and asymptotes to zero for the isolated case, $\Delta x \gg \xi_s$. The inter-soliton potential governs the force F and, accordingly, the acceleration a exerted on the solitons, given by $F = m^* a = -\frac{dV}{dx}$. Rearranging to

$$a = -\frac{1}{m^*}\frac{dV}{dx} \tag{6.4}$$

and noting that $m^* < 0$ for these solitons [see Eq. (2.46)], one can see that the solitons are accelerated towards a potential maximum, which does not occur at finite Δx (in the thermodynimic limit) in the case of two solitons with the same magnetisation. Thus, two solitons with $\nu = 1$ cannot form a bound state. This may seem counter-intuitive at first, since the solitons move in the opposite direction of the applied force. However, this behaviour of the negative effective masses is analogous to electron holes in a metal where the electrons hop along in one direction, and the holes effectively move in the opposite direction.[1]

The inter-soliton potential V_{-1} is shown in Fig. 6.3(b). The blue line is generated by imprinting stationary magnetic soliton pairs (SMSPs), which we have used exclusively until now. V_{-1} reaches a maximum when the solitons are superimposed ($\Delta x = 0$). In this case, there is a π phase jump in both components. To minimise energy the density in both components drops to zero at the soliton centres. We find the solution to be reminiscent of two black solitons in two components that have no inter-species interactions. The potential falls quickly for small separations Δx and then asymptotes to the isolated configuration. We find that the configuration of two initially stationary solitons with opposite magnetisation always leads to bound oscillatory states if Δx is not too large. This can be explained by the maximum in the potential towards which the solitons are accelerated.

Another way to generate the inter-soliton potential V_{-1} is by imprinting phase domain walls (PDWs) [see Sec. 5.2.2]. A PDW creates two solitons with opposite magnetisation moving in opposite direction with initial velocity v_{init}. Depending on the width b of the PDW [see Eq. (5.6)], these two solitons either travel faster than some escape velocity v_{esc} or when they are slower, ($v_{\text{init}} < v_{\text{esc}}$), they reach a turning point, and form an oscillatory bound state. This bound state is equivalent to the one formed using the SMSP approach, but it starts at a different phase of the oscillation. The representative dynamics of such a bound state are shown later in the inset of Fig. 6.4, marked with a green inverse triangle. We measure the maximum soliton separation Δx of the solitons and obtain the red line in Fig. 6.3(b). It is slightly above the blue line for $\Delta x \gg \xi_s$ and diverges for $\Delta x \ll \xi_s$. This is to be expected, as for this method, we imprint the PDW on a homogeneous density and use only a small amount of imaginary time. This is a good approximation for large separation where the solitons are almost isolated. For short separations, however, the SMSP approach shows that the antidark component of the solitons becomes suppressed, a behaviour not adequately captured by the small imaginary-time evolution. Accordingly, the total density should decrease across the solitons, making the approximation increasingly inaccurate and

[1] In Sec. 3.2, we saw that Refs. [34,35] plot $-V_{\text{sol}}$ to account for the negative effective mass of the solitons. Here, we chose to plot V_ν to emphasize that the solitons possess negative effective mass.

causing the PDW method to produce strong phonon excitations.[2]
We can compare the two approaches, *i.e.*, SMSP and PDW, solved with the GPE, with a semi-analytical approach, where we solve the coupled differential equations (2.40) using the Euler method for a phase domain wall with width b (semi-analytic PDW method, see Sec. 5.2.2). From the simulation, we extract the maximum separations between the solitons. We can calculate the inter-soliton potential energy from the energy of a PDW (5.7) by subtracting the energy of two isolated stationary solitons $E_{\mathrm{MS}}(v=0) = n\hbar c_s$ [see Eq. (2.45)], which gives

$$E(b) = E_{PDW} - 2E_{\mathrm{MS}}(v=0) = 2n\hbar c_s \left(\frac{\xi_s}{b} - 1\right). \tag{6.5}$$

The results are shown in Fig. 6.3(b) as the black line. Note that for large separations, $\Delta x \gg \xi_s$, boundary effects cause the simulations to break down before the turning point is reached, which is why we have no data for $\Delta x \gg \xi_s$. Because the coupled differential equations (2.40) enforce the total density to be constant, the energy unphysically diverges for small widths, $b \ll \xi_s$. All methods produce results in good qualitative agreement and, in some cases, quantitative agreement.

6.1.3. Dissociation energy of bound states

As shown in Sec. 6.1.2, the advantage of the PDW method is that it can produce both bound and unbound states with energy E_{PDW}. Considering the transition from unbound to bound states allows us to calculate the dissociation energy E_{dis} of a bound state and the critical width b_{crit} of the corresponding PDW. The solitons generated by the PDW method decelerate as they move apart due to the attractive force between them. If the solitons have $v/c_s > 0$ for $\Delta x \gg \xi_s$, they are unbound. However, if they become stationary for finite Δx, they form a bound state. The boundary between bound and unbound states corresponds exactly to the situation of two isolated stationary solitons. The energy of a single stationary soliton is $E_{\mathrm{MS}}(v=0) = n\hbar c_s$ and we hence find the dissociation energy to be [see also Eq. (6.5)]

$$E_{\mathrm{dis}} = 2n\hbar c_s, \tag{6.6}$$

which gives the critical domain wall width for dissociation

$$b_{\mathrm{crit}} = \xi_s. \tag{6.7}$$

This analytic result tells us that a relative 2π phase winding across both components results in a bound state of two solitons if the winding has a width that is smaller than the characteristic spin healing length ξ_s [recall Eq. (5.6)].
In Fig. 6.4, we show the inter-soliton potential energy [see Eq. (6.5)] of solitons pairs with

[2] Using longer imaginary time evolution only marginally improves the red curve in Fig. 6.3. During imaginary time evolution, the energy decreases, and the width b of the PDW broadens, resulting in a larger Δx. Both effects combine in such a way that points nearly follow the red curve in Fig. 6.3.

opposite magnetisation versus the inverse width b^{-1}, and compare the critical widths from the GPE simulations (SMSP and PDW methods) to the analytic critical width (6.7). The black dashed and solid lines show the analytic energy (6.5). Red solid squares and circles show the data for the PDW method for unbound and bound states, respectively. During the initial imaginary time evolution, the width b changes. We fit the phase profile after the imaginary time evolution to Eq. (5.6) for different fitting ranges to obtain multiple values of b_{fit}. The mean value of these fitted b_{fit} is taken to determine the width b' of the PDW after imaginary time evolution. The error bars are given by one standard deviation of the mean value b'. The detailed description of the fitting procedure can be found in the Appendix A.4. The blue crosses show the data generated with the SMSP method. Here we find the width b by performing real-time evolution until the solitons overlap, at which point we fit the phase profile to Eq. (5.6), as we do for the PDW.

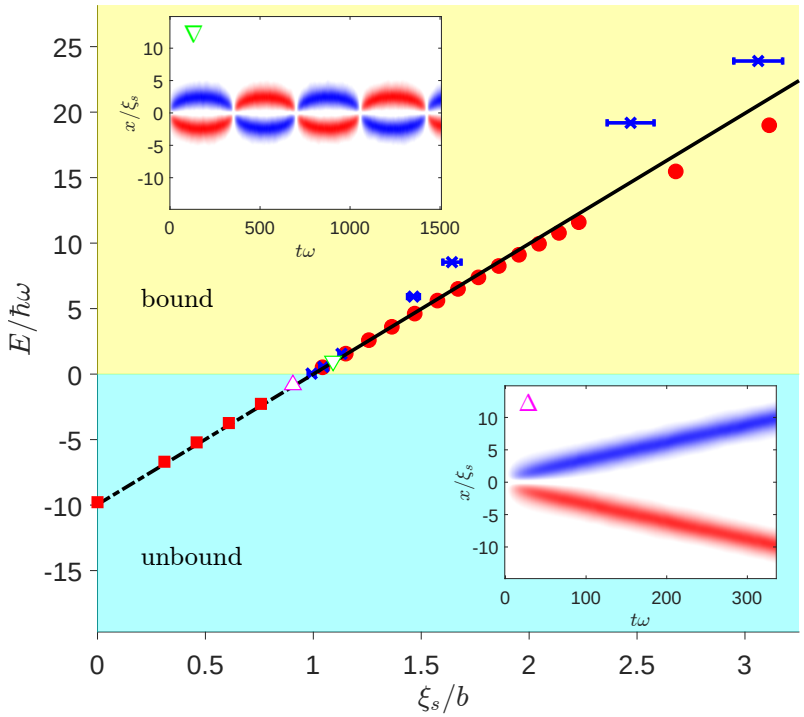

Figure 6.4.: Energy of soliton pairs with opposite magnetisation versus inverse width. The black solid (dashed) line shows the analytic energy of phase domain walls in the bound (unbound) regime [Eq. (6.5)]. The red circles (squares) show the data for the PDW method in the bound (unbound) regime. The data points have errorbars even though they might be smaller than the marker size. Blue crosses show the data for the SMSP method. The insets show real time evolutions of a bound state initially with $b^{-1} = 1.1$ (green inverse triangle) and an unbound state initially with $b^{-1} = 0.9$ (magenta triangle). Same parameters as in Fig. 6.1.

The inset, marked by the magenta triangle in Fig. 6.4, is produced with the PDW method, depicting representative dynamics of the unbound regime ($b^{-1} < 1/\xi_s$). In this regime, the data from the PDW method agrees well with the analytical result. The simulations indicate that the assumption of a constant total density n holds well. We estimate the

point of critical width from the numerics using

$$b_{\mathrm{dis,PDW}} = \frac{\min\left(b_{\mathrm{unbound}}\right) + \max\left(b_{\mathrm{bound}}\right)}{2}, \tag{6.8}$$

where b_{bound} (b_{unbound}) are all widths for which the PDW method produces a bound (unbound) state. This gives a critical width of $b_{\mathrm{dis,PDW}} = 1.03(7)\xi_s$, where the uncertainty accounts for the entire regime in which it is unclear whether the state is bound or unbound. This width agrees well with the analytic prediction $b_{\mathrm{crit}} = \xi_s$. The inset, marked by the green inverse triangle in Fig. 6.4, depicts representative dynamics of the bound regime ($b^{-1} > 1/\xi_s$). In this regime, the PDW method agrees well with the analytic result for widths close to b_{crit}. However, for $b^{-1} \gg 1/\xi_s$, a discrepancy develops, which can be traced to the formation of a density dip during the imaginary time evolution of the PDW method. We find that for $b^{-1} \gg 1/\xi_s$, the assumption of a constant total density in the analytic model becomes increasingly inaccurate, as observed in the previous section.
The SMSP method produces in principle only bound states. However, in a finite system, numerical noise and dissipation can lead to unbound solitons. We find a largest width $b_{\mathrm{SMSP}} = 1.01(2)\xi_s$ of a bound state, which agrees well with $b_{\mathrm{crit}} = \xi_s$. Close to the critical width b_{crit}, the SMSP method agrees well with the analytical result, while for $b^{-1} \gg 1/\xi_s$, the SMSP method yields a higher energy for the same width b than the analytic result. This is surprising, as the assumption of a constant total density in the analytic model overestimates the energy of the physical system. Therefore, one might expect the SMSP method to produce bound states with lower energy, as observed in Fig. 6.3(b). However, during real-time evolution, the SMSP method produces strong phonons for small separations Δx during the quarter period before the solitons overlap, where b can be extracted from a fit.[3] These phonons have an energy that is difficult to isolate, which leads to an increase in the apparent energy of the solitons for a given b. This effect becomes particularly significant for $b^{-1} \gg 1/\xi_s$, causing the energy of the solitons to exceed the analytical result. In contrast, this issue does not arise in the PDW method, as b can be extracted without relying on real-time evolution.

6.1.4. Oscillation period of excited bound states

The inter-soliton potential V_{-1} in Fig. 6.3(b) shows an anharmonic potential for moderate separations. Consequently, the oscillation period of the bound states depends on the maximum soliton separation Δx of the two solitons. We find the period T for a given Δx by imprinting SMSPs and using real-time evolution until the solitons overlap, then multiplying by 4 to obtain T. The results are shown in Fig. 6.5, where we can see a rapid growth consistent with exponential behaviour of T with Δx. When the solitons created with the SMSP method are superimposed ($\Delta x = 0$ at $t = 0$), they form a stationary state. The bound state shown in Fig. 6.2(c) with initial $\Delta x = 5.36\xi_s$ yields a period of $T \approx 916\omega^{-1}$.

[3] We suspect that this is because Eq. 2.34 is not integrable in the regime considered ($a_{12} \neq a_{ii}$), and the solitons are not true solitons, producing phonons upon collisions.

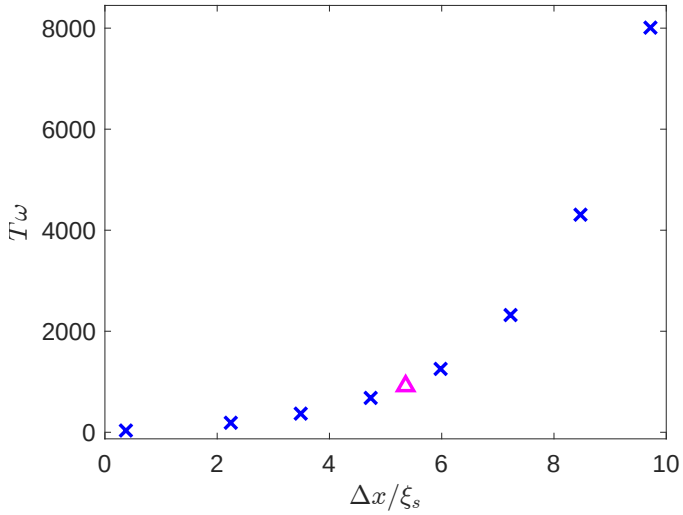

Figure 6.5.: Oscillation period versus maximum soliton separation of bound states. The magenta triangle marks the amplitude $\Delta x = 5.36\xi_s$ of the dynamics shown in Fig. 6.2(c). Same parameters as in Fig. 6.1.

6.1.5. Dark-antidark soliton bound states

The results presented in this section for magnetic solitons, can be expanded to dark-antidark solitons (DADs), *i.e.*, moving to interaction combinations further from the miscible-to-immiscible transition. We refrain from quantitatively investigating all aspects and only focus on the inter-soliton potential created with the SMSP method, which is also relevant for the next section.

Imbalances between the components and variations in a_{12} result in imbalances between the dark and antidark parts of the DAD, leading to a total density that is not uniform across the DAD. This has effects on the interactions between DADs. We compare in Fig. 6.6 the inter-soliton potential V_{-1} of magnetic solitons (solid blue line), and DADs in imbalanced components, which are close to the immiscibility transition (dot dashed green line) and far away from the transition (dashed red line). The inter-soliton potentials of the DADs exhibit qualitatively similar features to those of magnetic solitons: a maximum for $\Delta x = 0$ and $V_{-1} \to 0$ for $\Delta x \gg \xi_s$. However, far from the immiscibility transition, DADs exhibit a lower peak than magnetic solitons, whereas close to the transition, they exhibit a higher peak. The shape of the inter-soliton potential affects the strength of the attractive force between the solitons and influences the formation and stability of the oscillatory bound states in the presence of numerical noise and dissipation. DADs, far from the transition, form stable bound states only for small initial separations, while DADs, close to the transition, in a mixture with imbalanced components, behave similarly to magnetic solitons and can form bound states even for large initial separations, $\Delta x \gg \xi_s$ (not shown).

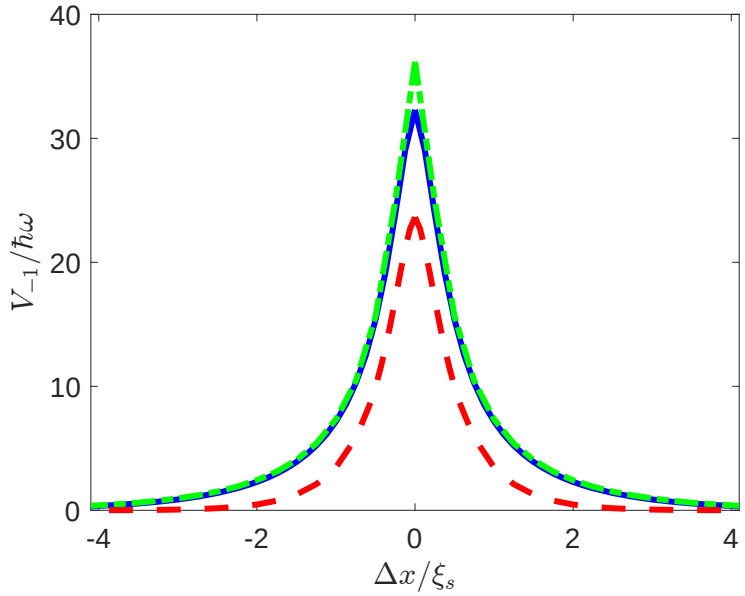

Figure 6.6.: Inter-soliton potential versus separation between DADs with opposite magnetisation in different regimes. The solid blue line shows the potential for magnetic solitons with the s-wave scattering lengths $a_{11} = a_{22} = 100\,a_0$ and $a_{12} = 95\,a_0$ (previously shown in Fig. 6.3). The dashed red line shows V_{-1} for DADs with $a_{11} = 140\,a_0$, $a_{22} = 100\,a_0$, and $a_{12} = 95\,a_0$. The dash-dotted green line shows V_{-1} for DADs with $a_{11} = 140\,a_0$, $a_{22} = 100\,a_0$ and $a_{12} = 114\,a_0$. The parameters for the dash-dotted green line and blue line are both close to the immiscible regime, whereas the system for the red line is far from it. Parameters: average integrated density per component $n_0 = N/2L = 50\,\mu\text{m}^{-1}$; total particle number $N = 3000$; radial confinement $\omega = 2\pi \times 2667\,\text{Hz}$; and spin healing length $\xi_s = 0.4703\,\mu\text{m}$.

6.2. Dark-antidark soliton bound states in dipolar-nondipolar condensate mixtures

In this section, we extend the results of the previous section by considering dipolar-nondipolar condensate mixtures, where the dipoles are oriented perpendicular to the tube axis. Since the components are now unbalanced, we consider dark-antidark solitons instead of magnetic solitons. We begin by deriving the Bogoliubov dispersion relations for a homogeneous density, providing important insights into the effects of the anisotropic DDIs, which give rise to the formation of density modulations around the solitons. These modulations lead to energetically (un)favourable separations between the solitons, giving rise to new regimes of bound states between solitons with opposite as well as equal magnetisation. Additionally, dipole–dipole interactions cause solitons to generate phonon and roton excitations during collisions, which can lead to their escape from the bound state. In this section, we use only the SMSP method to create solitons.

6.2.1. Bogoliubov theory

To get an idea of how the system responds to excitations, we derive the Bogoliubov dispersion relations for elementary excitations in binary dipolar BECs.[4]
We consider solutions to the coupled quasi-1D GPEs (4.26) of the form

$$\psi_i(x,t) = \left(\sqrt{n_0^{(i)}} + \lambda\left[u_i(x)e^{-i\epsilon t/\hbar} - v_i^*(x)e^{i\epsilon^* t/\hbar}\right]\right)e^{-i\mu_i t/\hbar}, \tag{6.9}$$

where the component i is perturbed via a small parameter λ around the uniform density $n_0^{(i)} = \left|\psi_0^{(i)}\right|^2$ with $\psi_0^{(i)} = \sqrt{N_i/L}$. We describe the perturbation with the Bogoliubov amplitudes u_i and v_i and quasiparticle mode energies ϵ. Inserting the ansatz (6.9) into the coupled quasi-1D GPEs (4.26), keeping only terms up to linear order in λ, collecting terms evolving in time with either $e^{-i\epsilon t/\hbar}$ or $e^{i\epsilon^* t/\hbar}$, and using the chemical potential for a homogeneous condensate $\mu_{i,0}$ [see Eq. (4.29)], gives the coupled equations

$$\begin{aligned}\epsilon u_i(x) =& -\frac{\hbar^2}{2m}\partial_x^2 u_i(x) + \frac{\sqrt{n_0^{(i)}}}{2\pi l^2}\sum_j g_{ij}\sqrt{n_0^{(j)}}\Big[u_j(x) - v_j(x)\Big] + \\ & \sqrt{n_0^{(i)}}\sum_j \sqrt{n_0^{(j)}}\mathcal{F}_x^{-1}\Big\{U_{ij}(k_x)\mathcal{F}_{k_x}\Big[u_j(x) - v_j(x)\Big]\Big\},\end{aligned} \tag{6.10}$$

$$\begin{aligned}\epsilon v_i(x) =& \frac{\hbar^2}{2m}\partial_x^2 v_i(x) + \frac{\sqrt{n_0^{(i)}}}{2\pi l^2}\sum_j g_{ij}\sqrt{n_0^{(j)}}\Big[u_j(x) - v_j(x)\Big] + \\ & \sqrt{n_0^{(i)}}\sum_j \sqrt{n_0^{(j)}}\mathcal{F}_x^{-1}\Big\{\hat{U}_{ij}(k_x)\mathcal{F}_{k_x}\Big[u_j(x) - v_j(x)\Big]\Big\}.\end{aligned} \tag{6.11}$$

Omitting the subscript of k_x and moving to momentum space $\Big(\mathcal{F}_k[a(x)] = \hat{a}(k)\Big)$ yields

$$\begin{aligned}\epsilon\hat{u}_i(k) =& \frac{\hbar^2 k^2}{2m}\hat{u}_i(k) + \frac{\sqrt{n_0^{(i)}}}{2\pi l^2}\sum_j g_{ij}\sqrt{n_0^{(j)}}\Big[\hat{u}_j(k) - \hat{v}_j(k)\Big] + \sqrt{n_0^{(i)}}\sum_j \hat{U}_{ij}(k)\sqrt{n_0^{(j)}}\Big[\hat{u}_j(k) - \hat{v}_j(k)\Big], \\ \epsilon\hat{v}_i(k) =& -\frac{\hbar^2 k^2}{2m}\hat{v}_i(k) + \frac{\sqrt{n_0^{(i)}}}{2\pi l^2}\sum_j g_{ij}\sqrt{n_0^{(j)}}\Big[\hat{u}_j(k) - \hat{v}_j(k)\Big] + \sqrt{n_0^{(i)}}\sum_j \hat{U}_{ij}(k)\sqrt{n_0^{(j)}}\Big[\hat{u}_j(k) - \hat{v}_j(k)\Big].\end{aligned} \tag{6.12}$$

The coupled equations can be written in a 4x4 matrix equation of the form $\epsilon\mathbf{w} = M\mathbf{w}$, where $\mathbf{w} = \{\hat{u}_1, \hat{u}_2, \hat{v}_1, \hat{v}_2\}$. The positive eigenvalues $\epsilon_\pm$ corresponds to the Bogoliubov dispersion relations of elementary excitations and are determined by

$$\epsilon_\pm^2(k) = \frac{\epsilon_1^2 + \epsilon_2^2}{2} \pm \frac{1}{2}\sqrt{(\epsilon_1^2 - \epsilon_2^2)^2 + 4G_{12}G_{12}\frac{\hbar^4 k^4}{m^2}}, \tag{6.13}$$

[4]The full derivation can be found in Appendix A.2 and is similar to the derivation of the excitations spectrum in binary antidipolar condensates in Ref. [98].

where the single-component energies are

$$\epsilon_i^2(k) = \frac{\hbar^2 k^2}{2m}\left(\frac{\hbar^2 k^2}{2m} + 2G_{ii}(k)\right), \tag{6.14}$$

and

$$G_{ij}(k) = \sqrt{n_0^{(i)} n_0^{(j)}}\,\frac{g_{ij}}{2\pi l^2} + \sqrt{n_0^{(i)} n_0^{(j)}}\,\frac{g_{ij}^{dd}}{4\pi l^2}\left[1 - 3Q^2 e^{Q^2}\mathrm{E}_1(Q^2)\right]. \tag{6.15}$$

We show the dispersion relations (6.13) in Fig. 6.7(a) for a dipolar-nondipolar condensate mixture. The black dashed line shows the dispersion relation for free particles as a reference, while the yellow line shows the dispersion relation for in-phase excitations (ϵ_+), called the density branch, and the green line shows the dispersion relation for out-of-phase excitations (ϵ_-), called the spin branch. The spin branch exhibits a spin roton, which is a local minimum in the dispersion relation and describes quasiparticles with non-zero momenta. The presence of a spin roton indicates that the system has a preferred wavelength for certain excitations. In the next subsection, we discuss the effects of the spin roton on spin excitations, such as dark-antidark solitons.

6.2.2. Dark-antidark solitons in the presence of dipolar interactions

Before studying the dynamics and interactions between dark-antidark solitons, we consider the density profile of a single soliton in a dipolar-nondipolar condensate mixture. In the following, the dipoles are aligned perpendicular to the tube axis by a magnetic field B.
Figure 6.7(b) shows a soliton for the same parameters as the dispersion relation shown in Fig. 6.7(a). The density branch (yellow line) is not directly relevant for solitons as they are spin excitations. We can see that the spin branch (green line) crosses the free-particle dispersion relation (black dashed line) and forms a roton-minimum at $k_{\mathrm{rot}} \approx 4.5/l$. This corresponds to a roton wavelength of $\lambda_{\mathrm{rot}} \approx 1.4\,l$. The crossing of the free-particle line indicates a transition from repulsive to attractive interactions for the spin excitations. Therefore, in response to perturbations, the system easily generates spin-density modulations (ripples) with a wavelength corresponding to λ_{rot}. This can be seen in Fig. 6.7(b), where ripples with a wavelength equal to λ_{rot} form around a soliton.
Another way to understand the formation of ripples around the solitons is to consider the arrangement of the dipoles around the density trough created by the soliton in the dark component and then examine its influence on the antidark component. Due to their head-to-tail attraction, dipoles tend to align and stack along the magnetic field direction. However, due to the radial confinement, there can only be a limited number of dipoles stacked on top of each other. The repulsive contact interactions and quantum pressure prevent the condensate from imploding. The side-by-side repulsion causes the dipole stacks to maximise their separation. Thus when imprinting a soliton, it is energetically favourable to form dipole stacks or rather density peaks around the central density dip. Next to

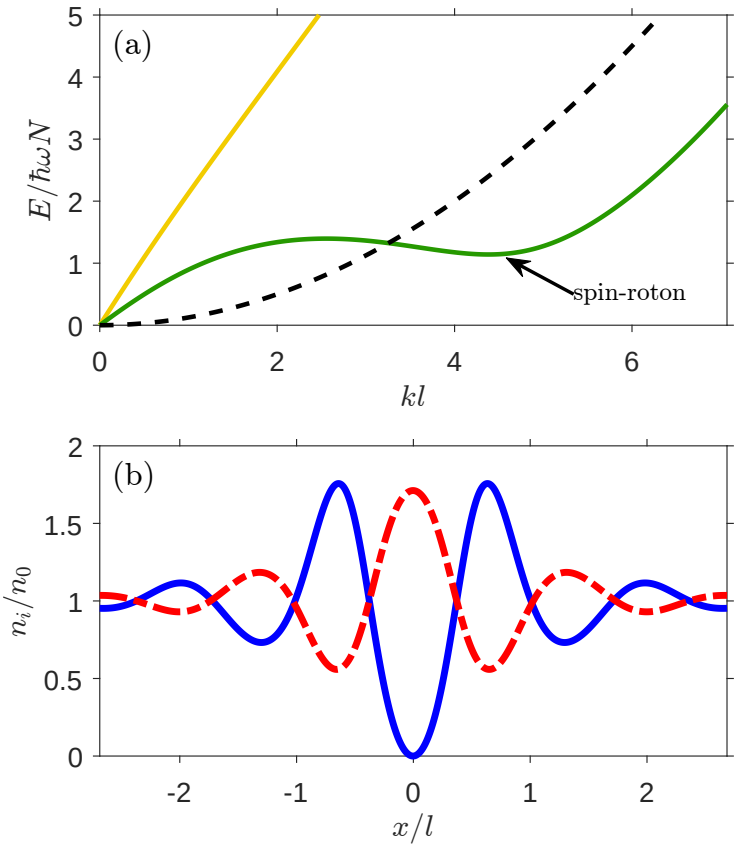

Figure 6.7.: (a) Dispersion relation of a homogenous dipolar-nondipolar condensate mixture. There is a roton-minimum with $k_{\mathrm{rot}}l \approx 4.5$ in the spin branch ϵ_- (green line). The yellow line shows the density branch ϵ_+ and the black dashed line shows the free-particle dispersion relation as a reference ($\hbar^2k^2/2m$). (b) Density profile of a dark-antidark soliton. The blue (red) line shows the density n_1 (n_2) of the first (second) component. Parameters: average integrated density per component $n_0 = N/2L = 667$ ^{162}Dy atoms $\mu\mathrm{m}^{-1}$; total particle number $N = 40000$; interactions parameters are $\{a_{11}, a_{12}, a_{22}\} = \{140, 105, 140\}\, a_0$, $\mu\mathrm{m}^{-1}$, $\{\mu_1, \mu_2\} = \{9.93, 0\}\, \mu_{\mathrm{B}}$; radial confinement $\omega = 2\pi \times 500\,\mathrm{Hz}$. The dipoles are aligned perpendicular to the tube axis.

these stacks of dipoles the density forms dips again to maximise the separation between the density peaks. This results in a spatially alternating pattern of density peaks and troughs similar to the ripples a dark soliton forms in a single-component dipolar condensate (see Sec. 2.4.1). These peaks and troughs become less pronounced as we move away from the soliton, as we are below the roton instability, after which a binary supersolid would form [106–108]. As shown in Fig. 6.7(b), the antidark component mirrors the density modulations in the dark component, forming a density peak where the dark component has a trough. This leads to modulations in the spin density, defined as $n_s(x) = n_1(x) - n_2(x)$, with alternating signs around the dark-antidark soliton.

6.2.3. Inter-soliton potential

The density ripples surrounding the soliton signify a modified inter-soliton potential V_ν (6.2) compared to the non-dipolar case. The modified potential V_{-1} is shown in Fig. 6.8, which shows maxima at $\Delta x_{\text{max}}^{(1,2,3)} = [0,\, 1.36,\, 2.72]\, l$ and minima at $\Delta x_{\text{min}}^{(1,2,3)} = [0.68,\, 2.04,\, 3.4]\, l$. We can understand these modifications by considering the density profile of the $s_1 = -1$ soliton in Fig. 6.7(b). We can foresee energetically favourable separations for imprinting a second $s_2 = 1$ soliton, which are $\Delta x_{\text{min}}^{(1,2,3)} = [0.68,\, 2.04]\, l$.[5] At these separations, $n_s(\Delta x_{\text{min}}^{(1,2)}) > 0$ has the same sign as the magnetisation of the $s_2 = 1$ soliton, reducing the energy required to form the soliton compared to introducing an $s_2 = 1$ soliton to a homogeneous density. An example of such a situation is displayed in Fig. 6.8(i), where we imprint an $s_1 = -1$ soliton at $x_1 = 0$ and an $s_2 = 1$ soliton at $x_2 = 0.68\, l$. This corresponds to the local minimum at $\Delta x_{\text{min}}^{(1)} = 0.68\, l$ in V_{-1}. On the other hand, it costs more energy to place an $s_2 = 1$ soliton at $x_2 = 1.36\, l$ where the $s_1 = -1$ soliton at $x_1 = 0$ creates a modulation with $n_s(x = 1.36\, l) < 0$. This is shown in Fig. 6.8(ii), resulting in the local maximum at $\Delta x_{\text{max}}^{(2)} = 1.36\, l$ in V_{-1}. As the sign of $n_s(x)$ alternates, so too does the inter-soliton potential, resulting in alternating regions where the inter-soliton potential exhibits local maxima and minima, which are attractive or repulsive potentials, respectively, due to the negative effective mass of the solitons. As the ripples fade far from the soliton, so too do the local maxima and minima of the inter-soliton potential.

Since V_{-1} has multiple separations $\Delta x_{\text{max}}^{(1,2,3)}$ that result in maxima, we observe multiple regions of bound states, each surrounded by local minima. The solitons forming bound states around $\Delta x_{\text{max}}^{(i)}$ undergo oscillatory motion, not passing through one another, but oscillating around $\Delta x_{\text{max}}^{(i)}$. Representative dynamics are shown later in Fig. 6.9(ii) and Fig. 6.9(iii) for bound states oscillating around $\Delta x_{\text{max}}^{(2)}$ and $\Delta x_{\text{max}}^{(3)}$, respectively. These bound states are reminiscent of dark solitons forming oscillatory bound states in single component dipolar BECs (see Sec. 3.2).

The minima at $\Delta x_{\text{min}}^{(i)}$ surrounding the maxima act as potential barriers, separating the regions of bound states. We consider the first minimum of V_{-1} at $\Delta x_{\text{min}}^{(1)}$ in Fig. 6.8. Imprinting two solitons with $\Delta x_{\text{min}}^{(1)}$ yields, in principle, a stationary solution. However, small perturbations cause the solitons to accelerate either towards each other or apart. When accelerating towards each other, the solitons undergo the same swapping dynamics observed in the non-dipolar case (see, *e.g.*, Fig. 6.2). However, in the presence of DDIs, solitons emit phonon and roton excitations during collisions, leading to energy loss and acceleration of the solitons. Eventually, they exceed the escape velocity and move apart indefinitely. On the other hand, if the solitons initially get accelerated apart, the second minimum, $\Delta x_{\text{min}} = 2.04\, l$, is too shallow to contain the solitons, causing them to move apart. No bound state is formed. From the different depths of the minima, we obtain different escape velocities $v_{\text{esc}}^{(1)} > v_{\text{esc}}^{(2)} > v_{\text{esc}}^{(3)}$ for the three regions of bound states, $\left|\Delta x_{\text{bound}}^{(1)}\right| < 0.68\, l$, $0.68\, l < \left|\Delta x_{\text{bound}}^{(2)}\right| < 2.04\, l$, $2.04\, l < \left|\Delta x_{\text{bound}}^{(3)}\right| < 3.4\, l$.

[5] The energetically favourable separation $\Delta x_{\text{min}}^{(3)} = 3.4\, l$ is not shown in Fig. 6.7(b).

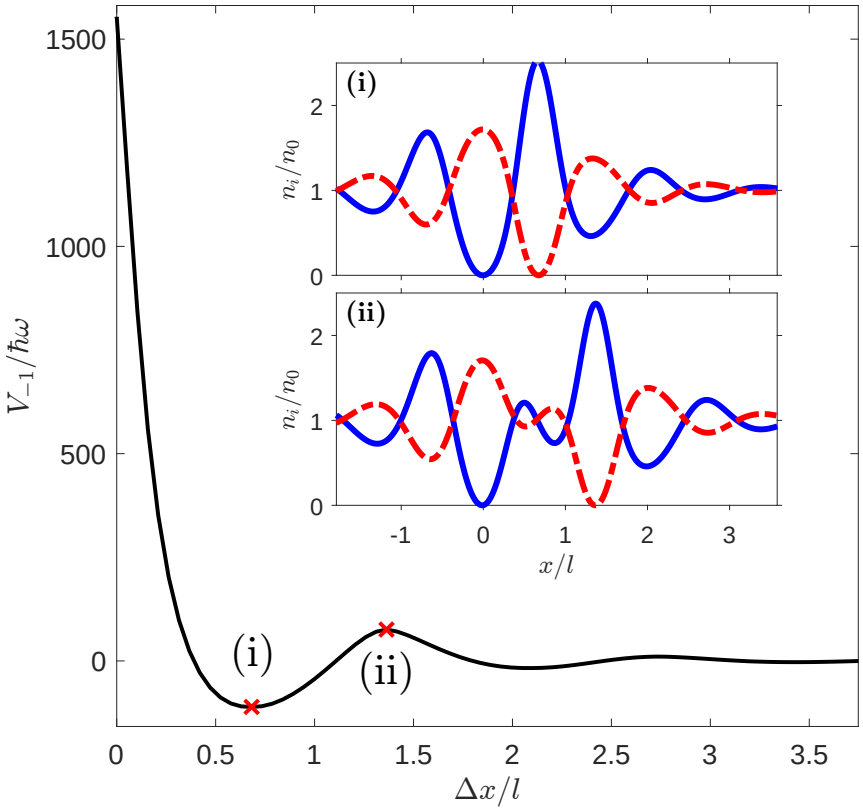

Figure 6.8.: Inter-soliton potential versus soliton separation for two solitons of opposite polarisation in the presence of dipolar interactions. Here we find three maxima, $\Delta x_{\mathrm{max}}^{(1,2,3)} = [0,\, 1.36,\, 2.72]\, l$, around which three distinct regions of bound states are possible. The insets show the density distribution of two solitons with a separation (i) $\Delta x_{\mathrm{min}}^{(1)} = 0.68\, l$ and (ii) $\Delta x_{\mathrm{max}}^{(2)} = 1.36\, l$, which correspond to a minimum and maximum of the inter-soliton potential V_{-1}, respectively. The blue line shows component 1 and the red dashed line shows component 2. Interaction parameters as in Fig. 6.7.

With increasing depth of the spin roton, the ripples around the solitons become more pronounced. Consequently, the peaks and troughs of the inter-soliton potential V_{-1} also grow more pronounced, with the maxima rising and the minima deepening. To examine the effects of the depth of the minima relative to the maxima on the bound states, we consider V_{-1} for different roton depths, which we control by changing the inter-component contact interaction a_{12}. Figure 6.9 shows the inter-soliton potential $V_{-1}(\Delta x,\, a_{12})$ over a wide range of a_{12}. To highlight the small minima and maxima relative to the maximum at $\Delta x = 0$, we show the data with the symmetric log transformation

$$\mathrm{slog}(x) = \mathrm{sign(x)log}\left(\sqrt{x^2+1}\right), \tag{6.16}$$

which transforms positive and negative values symmetrically around zero. We plot $V_{-1}(\Delta x,\, a_{12})$ for $20\, a_0 < a_{12} < 108.8\, a_0$, which is almost up to the roton instability ($a_{12}^{\mathrm{crit}} \approx 108.82\, a_0$).
Figure 6.9 shows that, for a fixed a_{12}, at least three local maxima (red circles) are present

in V_{-1}. We observe that the first maximum, at $\Delta x^{(1)}_{\max} = 0$, is present for all a_{12}. The second maximum, at $\Delta x^{(2)}_{\max}(a_{12} \approx 45\,a_0) \approx 1.52\,l$, emerges for $a_{12} \geq 45\,a_0$, while the third maximum, at $\Delta x^{(3)}_{\max}(a_{12} \approx 85\,a_0) \approx 2.88\,l$, appears for $a_{12} \geq 85\,a_0$. Close to the roton instability, the modulations of V_{-1} grow more pronounced, and additional maxima may form further out (not shown). Along the a_{12} axis, we observe that the maxima form three distinct ridges $V_{-1}(\Delta x^{(i)}_{\max}, a_{12})$. For the first ridge, we find that $\Delta x^{(1)}_{\max} = 0$ for all values of a_{12} considered. In contrast, for the second ridge, $\Delta x^{(2)}_{\max}$ decreases monotonically from approximately $1.52\,l$ at $a_{12} \approx 45\,a_0$ to about $1.31\,l$ at $a_{12} \approx 85\,a_0$, and then increases monotonically to approximately $1.36\,l$ at $a_{12} \approx 108.8\,a_0$. The third ridge shows a similar trend: $\Delta x^{(3)}_{\max}$ decreases monotonically from approximately $2.88\,l$ at $a_{12} \approx 85\,a_0$ to $2.72\,l$ at $a_{12} \approx 100\,a_0$, and then increases to approximately $2.78\,l$ at $a_{12} \approx 108.8\,a_0$. Considering V_{-1} along each ridge, we find that the first ridge, $V_{-1}(\Delta x^{(1)}_{\max}, a_{12})$, increases monotonically as the system approaches the roton instability. The second ridge, $V_{-1}(\Delta x^{(2)}_{\max}, a_{12})$, initially decreases before reaching a saddle point at $a_{12} \approx 60\,a_0$, after which it rises rapidly as a_{12} increases. The third ridge $V_{-1}(\Delta x^{(3)}_{\max}, a_{12})$ exhibits similar behaviour with a saddle point at $a_{12} \approx 95\,a_0$.

As shown previously, for each $\Delta x^{(i)}_{\max}(a_{12})$, there exists a bound state region $\Delta x^{(i)}_{\text{bound}}(a_{12})$ around it. Dynamic simulations of long-lived bound states are shown in Fig. 6.9(i), Fig. 6.9(ii) and Fig. 6.9(iii) for three different bound state regions $\Delta x^{(1)}_{\text{bound}}(a_{12} = 95\,a_0)$, $\Delta x^{(2)}_{\text{bound}}(a_{12} = 70\,a_0)$ and $\Delta x^{(3)}_{\text{bound}}(a_{12} = 95\,a_0)$, respectively. The bound state in Fig. 6.9(i) has a survival time of $t_{\text{bound}} \approx 60\omega^{-1}$, after which the bound state decays into two unbound solitons. We consider the survival times of bound states $t_{\text{bound}}(\Delta x, a_{12})$ and find that the longest-lived bound states with $\Delta x \neq \Delta x^{(i)}_{\max}$ occur at around $a^{(1)}_{12,ll} \approx 95\,a_0$ for $\Delta x^{(1)}_{\text{bound}}$, $a^{(2)}_{12,ll} \approx 60\,a_0$ for $\Delta x^{(2)}_{\text{bound}}$, and $a^{(3)}_{12,ll} \approx 95\,a_0$ for $\Delta x^{(3)}_{\text{bound}}$. Intriguingly, the values of $a^{(2,3)}_{12,ll}$ coincide with the saddle points of the ridges $V_{-1}(\Delta x^{(2,3)}_{\max}, a_{12})$. For a_{12} far from $a^{(i)}_{12,ll}$, bound states in their respective regions typically decay within a few oscillations (not shown).

We suspect that two underlying mechanisms play the most significant role in determining the survival times $t_{\text{bound}}(\Delta x, a_{12})$ of the bound states. The first mechanism arises from both the height of the maximum and the depth of the adjacent minima. The height of the maximum increases as we approach the roton instability, resulting in stronger binding between the solitons, making them less likely to become unbound (see Sec. 6.1.5). With dipoles present, minima also form, causing the difference from peak to trough to be larger than the nondipolar case. This effectively increases the binding between the solitons. Therefore, one might expect bound states to survive longer as the system approaches the roton instability. However, the second mechanism is that, as shown previously, solitons lose energy due to the production of phonon and roton excitations during collisions in binary dipolar BECs. As the system approaches the roton instability, the production of phonons and rotons during collisions increases, resulting in a more rapid acceleration of solitons and the subsequent decay of bound states. These two mechanisms scale differently with a_{12}, resulting in a distinct value of a_{12} for each bound state ridge $\Delta x^{(i)}_{\text{bound}}$, at which $t_{\text{bound}}(\Delta x, a_{12})$ reaches a maximum. A more thorough analysis of $t_{\text{bound}}(\Delta x, a_{12})$ would

require an analytical model capturing both mechanisms. Such a model could potentially also explain the variation of $\Delta_{\mathrm{max}}^{(2,3)}$ for increasing a_{12}, and whether this variation influences $t_{\mathrm{bound}}(\Delta x,\, a_{12})$. However, this analysis exceeds the scope of this thesis.

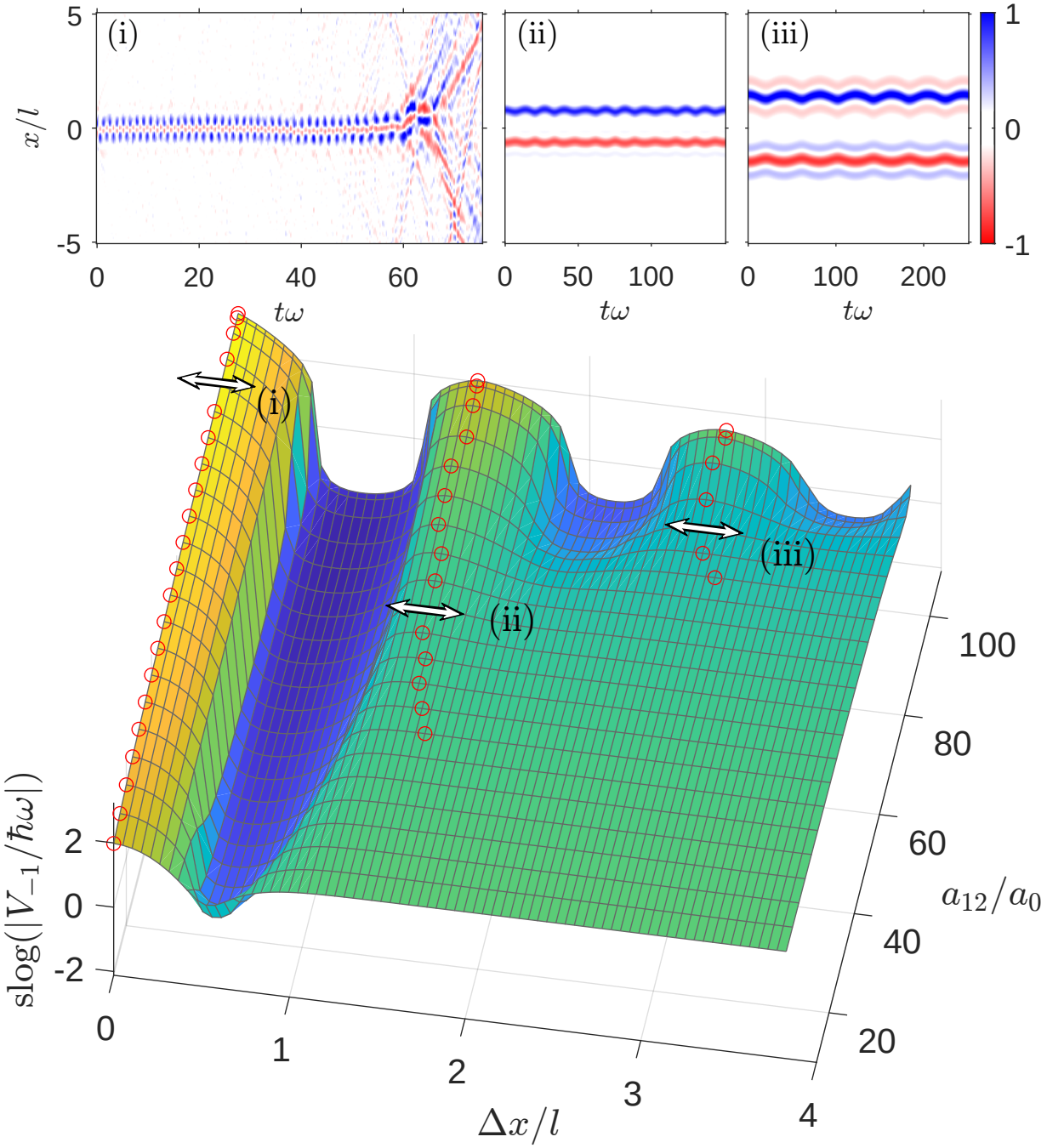

Figure 6.9.: Logarithmic inter-soliton potential versus separation of two solitons with opposite magnetisation, evaluated over a wide range of inter-component interactions in the presence of dipolar interactions. The inter-soliton potential develops ridges for higher a_{12}. We use the symmetric log transformation $\mathrm{slog}(x) = \mathrm{sign(x)log}\left(\sqrt{x^2+1}\right)$. The circles indicate local maxima for fixed a_{12}. There are three regions of local maxima at $x_{\mathrm{max}}^{(1,2,3)}(a_{12})$ (for specific values see main text), whereas the second (third) maxima appear only for $a_{12} \geq 45\,a_0$ ($a_{12} \geq 85\,a_0$). The insets show dynamics around the first maximum (i) for $a_{12} = 95\,a_0$, the second maximum (ii) for $a_{12} = 70\,a_0$ and the third maximum (iii) for $a_{12} = 95\,a_0$. The insets show the magnetisation s and have the same colourmap as in Fig 6.1. The first bound state (i) decays after $t \approx 60\,\omega^{-1}$. Unstated parameters are the same as in Fig. 6.7.

6.3. Collisions between dark-antidark solitons

In this section, we explore the behaviour of solitons and bound states colliding with each other. We use the insights acquired in Sec. 6.1 and Sec. 6.2 to explore and understand when solitons pass through one another and when they bounce off each other, for both non-dipolar and dipolar binary BECs. Furthermore, we investigate the collisions between bound states.
In the following, we refer to solitons with $s_i < 0$ as $\downarrow$ solitons and to solitons with $s_i > 0$ as $\uparrow$ solitons [see Eq. (2.35)]. We refer to collisions between solitons with $\nu < 0$ [see Eq. (6.3)] as $\uparrow\downarrow$ or $\downarrow\uparrow$, and to collisions between solitons with $\nu > 0$ as $\uparrow\uparrow$ or $\downarrow\downarrow$. The same applies for bound states. The sequence of arrows corresponds to the spatial order of the solitons, progressing from negative to positive x.

6.3.1. Non-dipolar

We consider collisions between slow-moving magnetic solitons in non-dipolar binary condensates. Examples of collisions are shown in Fig. 6.10, where we imprint two $\downarrow$ solitons ($s = -0.98$) at $x = [0,\ 31.89]\xi_s$ with $v_1 = \pm 0.199 c_s$ and two $\uparrow$ solitons ($s = 1$) at $x = [-7.97,\ 7.97]\xi_s$ with $v_2 = 0$ and consider the dynamics. We see that solitons pass through one another for $\uparrow\downarrow$ and $\downarrow\uparrow$ collisions, and bounce off each other for $\downarrow\downarrow$ collisions (see, *e.g.*, $t\omega \approx 1500$). This behaviour can be explained by the forces the solitons exert on each other according to the inter-soliton potential V_ν (6.2), as shown in Sec. 6.1.2. Accordingly, solitons propagating towards each other with $\uparrow\downarrow$ or $\downarrow\uparrow$ see a potential peak, which corresponds to an potential well due to the negative effective mass of the solitons. The solitons pass through one another and, if sufficiently fast, continue propagating indefinitely apart (see, *e.g.*, $200 < t\omega < 1000$); otherwise they may form a bound state (not shown). On the other hand, solitons propagating towards each other with $\uparrow\uparrow$ or $\downarrow\downarrow$ see a potential trough which corresponds to an potential barrier. Slow-moving solitons bounce off each other (see $t\omega \approx [1550, 4500]$), while sufficiently fast solitons that overcome the barrier pass through one another (see Sec. 3.1.2).
As this is a relatively small system for four solitons, the solitons are not fully isolated initially and interact slightly. We observe this for the upper $\uparrow$ soliton starting at $x = 7.97\xi_s$, which is attracted by the $\downarrow$ soliton at $x = 0$ and accelerates downwards until $t \approx 400\omega^{-1}$, where the $\downarrow$ soliton collides with the lower $\uparrow$ soliton. Then the two $\uparrow$ solitons repel until $t \approx 2600\omega^{-1}$. After multiple collisions, we observe that the $\uparrow$ solitons acquire a non-trivial velocity. We speculate that this results from the repulsive interactions between the $\uparrow$ solitons and slightly inelastic collisions. A more careful study would need to consider collisions of a single $\downarrow$ soliton with a single $\uparrow$ soliton, determining whether the non-moving soliton recovers its zero velocity after the collision. This, however, goes beyond the scope of this thesis.

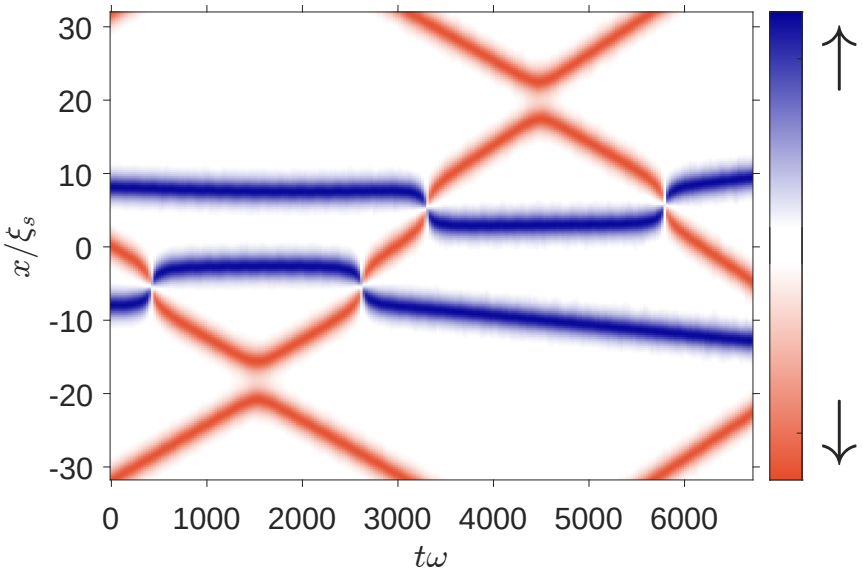

Figure 6.10.: Unbound dynamics between two stationary (blue) and two moving (red) magnetic solitons in non-dipolar binary BECs. Parameters: average integrated density per component $n_0 = N/2L = 50\,\mu\text{m}^{-1}$; total particle number $N = 3000$; interactions $\{a_{11}, a_{12}, a_{22}\} = \{100, 95, 100\}\,a_0$; radial confinement $\omega = 2\pi \times 2667\,\text{Hz}$; and spin healing length $\xi_s = 0.4703\,\mu\text{m}$.

6.3.2. Bound states

In the following, we consider collisions between bound states of magnetic solitons in non-dipolar binary BECs. Section 6.1 shows that initially stationary magnetic solitons move apart for $\nu > 0$ (same magnetisation) or move towards and through each other for $\nu < 0$ (opposite magnetisation). In the latter case, they can form a bound state if their maximum velocity is below the escape velocity. The solitons then oscillate periodically through the centre-of-mass position x_{com}, which is fixed. The bound state periodically switches its configuration from $\uparrow\downarrow$ to $\downarrow\uparrow$.

To generate bound states with non-zero centre-of-mass velocity ($v_{\text{com}} \neq 0$), we imprint two solitons with opposite magnetisations adjacent to each other, propagating in the same direction with a velocity of v_{com}. The solitons undergo two separate motions. The first corresponds to the movement of the centre of the bound state, while the second describes the motion of the two solitons around $x_{\text{com}}(t)$. The resulting dynamics cause the leading soliton to decelerate while the trailing soliton accelerates, until they pass through one another and switch positions. In the case of magnetisations $|s| \lesssim 1$, the leading soliton decelerates until it stops propagating and then accelerates in the other direction, which can be seen in Fig. 6.11(a). For $|s| \ll 1$ the solitons never become stationary (not shown). We consider collisions between slow-moving bound states in Fig. 6.11. In Fig. 6.11(a), we imprint two $\downarrow$ solitons ($s = -0.998$) at $x = [0,\ -31.9]\xi_s$ and two $\uparrow$ solitons ($s = 0.998$) at $x = [-4,\ -27.9]\xi_s$. This creates a bound state at $x^{(1)}_{\text{com}} = -2\xi_s$ with initial configuration $\uparrow\downarrow$ and a bound state at $x^{(2)}_{\text{com}} = -29\xi_s$ with initial configuration $\downarrow\uparrow$. The bound states have the same oscillation period, which means that the sequence of the bound states is

mirrored at all times. The bound states move towards each other and collide, emerging unscathed and retaining $|v_{\mathrm{com}}|$ without any visible dissipation. This soliton-like behaviour of the bound states is quite striking but not unexpected, as the underlying dynamics during collisions are governed by one soliton of one bound state interacting with one soliton of the other. The colliding solitons have the same magnetisation and bounce off each other, causing the two bound states to bounce as well.

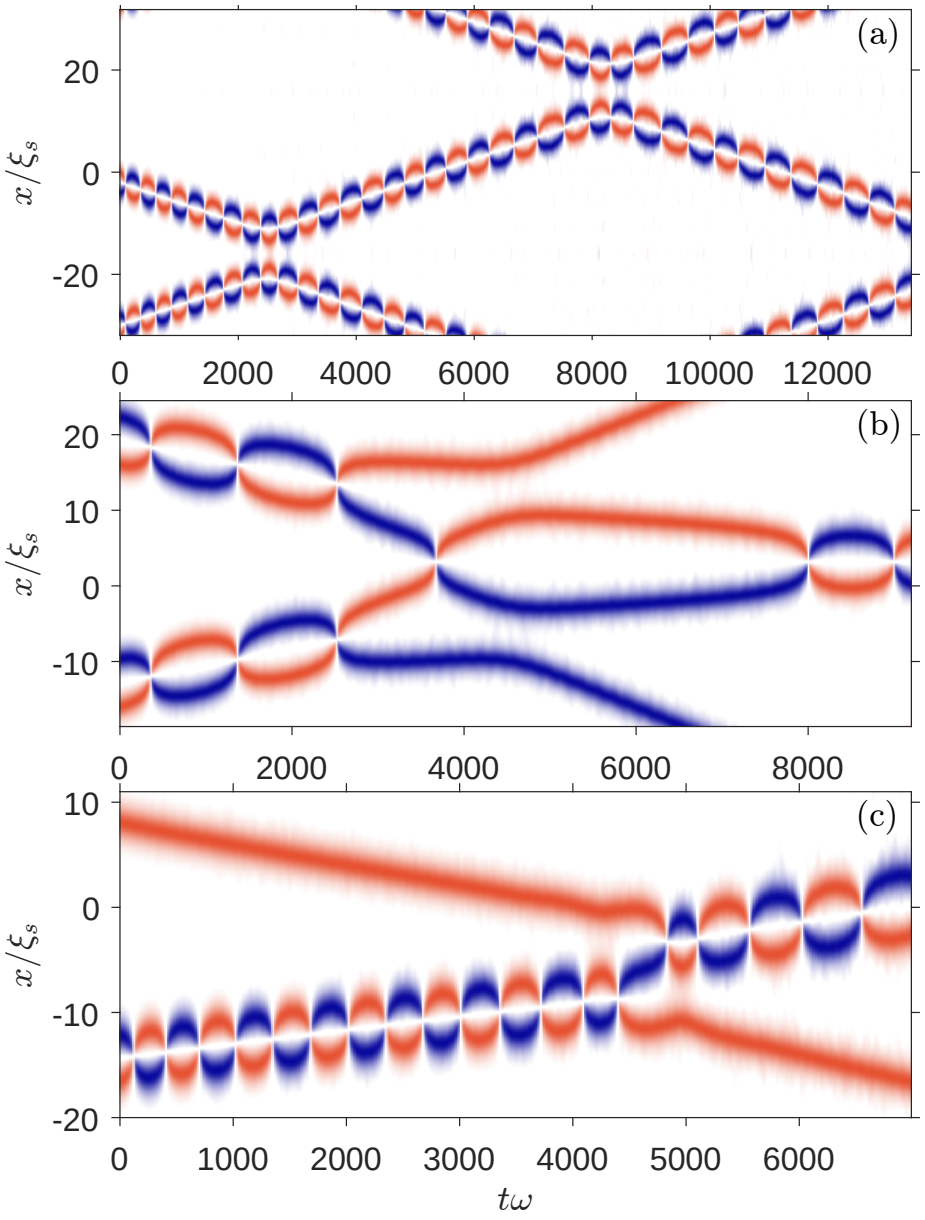

Figure 6.11.: Collisions between bound states. (a) Dynamics of two bound states with mirrored configurations, initially ↓↑ and ↑↓. The bound states bounce elastically. (b) Two bound states with identical initial configurations, ↓↑ and ↓↑. They collide inelastically, resulting in the formation of a new bound state and two unbound solitons. (c) Collision between a ↓ soliton and a bound state. Parameter and colourmap as in Fig 6.10.

In Fig. 6.11(b), we consider collisions between bound states with an identical sequence, such that they are ↓↑ and ↓↑ or ↑↓ and ↑↓ at a given time. We imprint two ↓ solitons ($s = -0.998$) at $x = [-15.9,\ 15.9]\xi_s$ and two ↑ solitons ($s = 0.998$) at $x = [-9.5,\ 22.3]\xi_s$, which creates two bound states at $x_{\mathrm{com}}^{(1)} = -12.7\xi_s$ and $x_{\mathrm{com}}^{(2)} = 19.6\xi_s$ with initial configuration ↓↑ and same oscillation period. The bound states collide in such a manner that the colliding solitons exhibit opposite magnetisation. They attract and extract one another from their respective bound states, subsequently passing through one another and then bounce off the solitons that remain from the original bound states. The inner two solitons form a new bound state, whereas the outer solitons become unbound and move away from the collision region. Ultimately, the two initial bound states decay into a single new bound state and two unbound solitons. The centre-of-mass motion of the new bound state is an average of the centre-of-mass motion of the initial bound states and is zero in the case of Fig. 6.11(b). In Fig. 6.11(c), we show the collision of a single soliton with a bound state. When the ↓ soliton collides with the bound state, we see that the ↑ soliton gets attracted by it, while the other ↓ soliton gets repelled. A switch between the roles of ↓ solitons occurs. The ↓ soliton, which was initially unbound, becomes bound, and vice versa. Following the switch, the bound state continues to propagate with approximately its original characteristics, exhibiting only a slight change in the oscillation period and a shift in the centre-of-mass trajectory. This shows that bound states can emerge unscathed from collisions with single solitons and that it is possible to exchange the participants of the bound state.

6.3.3. Dipolar

In a dipolar-nondipolar condensate mixture, as discussed in Sec. 6.2.3, solitons can interact both attractively and repulsively, independent of their relative magnetisation, as shown by the maxima and minima in the inter-soliton potential (see Fig. 6.9). For collision between soliton, the minima in the inter-soliton potential act as potential barriers, causing the solitons to repel. Accordingly, slow-moving solitons bounce off each other even in collisions between solitons with opposite magnetisation. This is shown in Fig. 6.12, where we imprint two propagating ↓ solitons ($s = -0.9$) at $x = [0,\ 13.4249]\, l$ and two stationary ↑ solitons ($s = 1$) at $x = [-3.36,\ 3.36]\, l$. A moving ↓ soliton almost stops after the collision at $t\omega \approx 25$ and transfer its momentum to a stationary ↑ soliton, causing it to start propagating. This is reminiscent of an elastic collision between a moving and a non-moving hard sphere. Collisions between two moving solitons with opposite magnetisation show that they bounce almost elastically (see, *e.g.*, $t\omega \approx 55$). Fast solitons can overcome the potential barrier and move through solitons with opposite magnetisation (not shown). However, these collisions are inelastic and produce a lot of phonons and rotons, which can lead to the decay of the solitons.

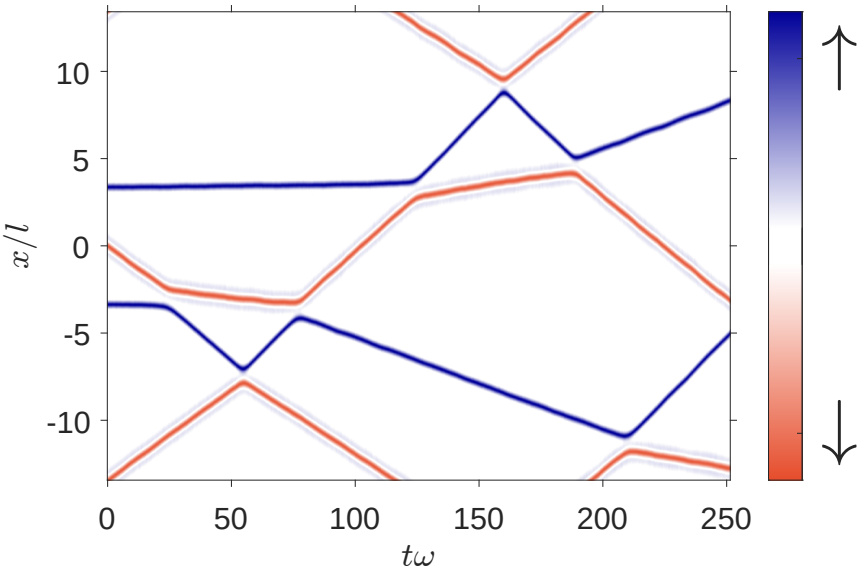

Figure 6.12.: Unbound dynamics between two initially stationary (blue) and two initially slow-moving (red) magnetic solitons in binary dipolar BECs. Parameters: average integrated density per component $n_0 = N/2L = 667$ ^{162}Dy atoms $\mu\mathrm{m}^{-1}$; total particle number $N = 40000$; interactions parameters are $\{a_{11}, a_{12}, a_{22}\} = \{140, 20, 140\}\, a_0$, $\mu\mathrm{m}^{-1}$, $\{\mu_1, \mu_2\} = \{9.93, 0\}\, \mu_\mathrm{B}$; radial confinement $\omega = 2\pi \times 500\,\mathrm{Hz}$. The dipoles are aligned perpendicular to the tube axis.

7. Conclusion and outlook

This thesis aimed to deepen our understanding of the formation of bound states between magnetic solitons and dark-antidark solitons, and to expand the findings to dark-antidark solitons in binary dipolar BECs. In this chapter, we briefly summarise the various results presented in this thesis and provide an outlook, proposing future research directions to follow up on these results.

7.1. Results

We considered the soliton-soliton interactions in quasi-1D binary BECs between two initially stationary solitons for both cases of same magnetisation and opposite magnetisation. We found that, in non-dipolar binary BECs, magnetic solitons repel each other when they have the same magnetisation and attract when they have opposite magnetisation. We calculated the inter-soliton potential, revealing a potential minimum (maximum) when two magnetic solitons are superimposed with the same (opposite) magnetisation. We found that, due to the negative effective mass of the soliton, the solitons are accelerated towards a potential maximum. As a result, solitons with opposite magnetisation can form bound states. By considering phase domain walls that decay into two counter-propagating magnetic solitons with opposite magnetisation, we were able to calculate the dissociation energy of the bound states between magnetic solitons analytically, and found good agreement with numerical simulations. An analysis of the dynamics of the bound states revealed that the oscillation period of the bound states is dependant on the maximum soliton separation Δx and diverges as $\Delta x \to \infty$. Furthermore, we extended our findings to dark-antidark solitons, observing that their behaviour is qualitatively similar to that of magnetic solitons.
We then considered dark-antidark solitons in dipolar-nondipolar condensate mixtures. We derived the Bogoliubov dispersion relations for binary condensates with polarised dipoles. We found that the presence of a spin roton with wavelength λ_{rot} causes spin density modulations to form around the main feature of a dark-antidark soliton. These modulations, in turn, lead to a spatial dependence of the magnitude and sign of the inter-soliton potential. The inter-soliton potential forms modulations with wavelength $\lambda = \lambda_{\text{rot}}$, resulting in additional maxima and minima. Accordingly, we identified additional stable separations around which bound states between dark-antidark solitons, with either the same or opposite magnetisation, can form. We investigated the emergence of additional bound states between dark-antidark solitons with opposite magnetisation as a function of the interspecies scattering length, and found that, far from the roton instability, only

the maximum at $\Delta x = 0$ survives, whereas close to the roton instability, multiple maxima emerge which can support long-lived bound states. Because dark-antidark solitons collide inelastically, producing phonons and rotons, we found that bound states eventually decay into two unbound dark-antidark solitons. We hypothesised that the stability of the bound states arises from the competing factors of phonon and roton production during oscillations, which increases with the depth of the spin roton, and the proximity to the transition to the immiscible regime, where bound states in non-dipolar binary BECs exhibit the widest spatial range of stable configurations.
We then considered the collisions between slow-moving magnetic solitons in the non-dipolar case, where we found that the collision behaviour depends on the relative magnetisation between the two magnetic solitons. We demonstrated the possibility of exchanging a single soliton from a bound state with an unbound one by colliding the latter with the bound state. Further, we found that bound states can collide either elastically, similar to magnetic solitons, or inelastically, depending on the relative polarisation between the bound states. In the inelastic case, two bound states may decay into a single bound state and two unbound magnetic solitons. In dipolar-nondipolar condensate mixtures, we found that slow-moving dark-antidark solitons always bounce off each other, independent of the relative magnetisation, in contrast to non-dipolar mixtures.

7.2. Outlook

Dark-antidark solitons in non-dipolar binary condensates are well understood and have been experimentally realised. However, the formation of bound states between these solitons has not yet been observed in experiments. Furthermore, to the best of our knowledge, no analytical model currently exists to describe magnetic solitons forming bound states without assuming a constant total density. Such a model could provide an accurate description of the energy and oscillation period, even for small maximum soliton separations.
Dark-antidark solitons in binary dipolar condensates have yet to be realised experimentally. The potential for additional bound states between dark-antidark solitons is intriguing, and could offer new insights into the non-locality of quasi particles in binary dipolar BECs. An obvious extension to the analysis done in Sec. 6.2 would be to consider the inter-soliton potential between two magnetic solitons with the same magnetisation. This analysis would likely reveal the existence of equilibrium separations around which bound states may form, in contrast to the non-dipolar case. Furthermore, an analytical model describing dark–antidark solitons in binary dipolar condensates could elucidate the regimes in which bound states between magnetic solitons with the same and opposite magnetisations are long-lived, and provide both a qualitative and quantitative explanation of their decay processes.
Full 3D simulations should supplement the findings of this thesis and extend the analysis beyond the quasi-1D case at high densities. This would also enable investigations of the stability of bound states in relation to that of dark-antidark solitons in two and three

dimensions.

Exploring bound states in finite-temperature systems could reveal regimes where bound states are experimentally accessible. Future directions will involve finding experimental protocols to generate dark-antidark solitons and bound states in dipolar-nondipolar mixtures. A method of creating bound states in experiments could involve ramping a binary BEC that is far from the immiscibility transition, bringing a_{12} closer to the transition. In this method, two dark-antidark solitons with opposite magnetisation would be imprinted in a binary BEC far from the immiscibility transition. The dark-antidark solitons would then move towards each other, and when they are sufficiently close, the binary BEC would be ramped close to the transition. This increases the maximum of the inter-soliton potential, effectively deepening the potential well between the dark-antidark solitons, which results in the dark-antidark solitons becoming trapped in the bound state. Although intriguing, a more realistic approach would be to imprint two dark–antidark solitons with an equilibrium separation directly onto the condensate, or to use evaporative cooling to potentially create dark-antidark solitons from the temperature ramp [109], similar to the Kibble–Zurek solitons in Ref. [110]. However, it is crucial to ensure that the system is genuinely one-dimensional, as the solitons in Ref. [110] were later identified as solitonic vortices [111], since the system was not sufficiently one-dimensional.

A. Appendix

A.1. Derivation of the coupled quasi-1D Gross-Pitaevskii equations

In this appendix, we derive the coupled quasi-1D GPE from the coupled 3D GPE (4.8) in detail for the non-dipolar terms, using the ansatz of non-isotropic Gaussians in the radial direction.
We start with the two-component 3D GPE

$$i\hbar\partial_t\Psi_i(\mathbf{r}) = \mathcal{G}_i^{3\mathrm{D}}\Psi_i(\mathbf{r}) = \left[-\frac{\hbar^2\nabla^2}{2m_i} + V_i(\mathbf{r}) + \sum_j g_{ij}n_j^{3\mathrm{D}}(\mathbf{r}) + \sum_j \Phi_{ij}(\mathbf{r})\right]\Psi_i(\mathbf{r}), \tag{A.1}$$

with $n_j^{3\mathrm{D}}(\mathbf{r}) = |\Psi_j(\mathbf{r})|^2$, $g_{ij} = 2\pi\hbar^2 a_{ij}(m_i + m_j)/(m_i m_j)$ and external potential $V_i(\mathbf{r}) = 1/2m_i(\omega_{xi}^2x^2 + \omega_{yi}^2y^2 + \omega_{zi}^2z^2)$ and dipole-dipole interaction

$$\Phi_{ij}(\mathbf{r}) = \int d\mathbf{r}' U(\mathbf{r}-\mathbf{r}')|\Psi(\mathbf{r}')|^2, \tag{A.2}$$

where $U(\mathbf{r}) = \frac{3g_{dd}}{4\pi r^3}\left(1 - 3\frac{y^2}{r^2}\right)$. The quantities are defined as in Sec. 4.2, except that the particle mass and trapping parameters may differ between components.
We approximate solutions in an elongated trap to be of separable form $\Psi(\mathbf{r}) = \psi(x)\phi_i(y,z)$, which lets us integrate out the transverse dimensions via:

$$\mathcal{G}_i^{\mathrm{q1D}} = \int dydz\, \phi^*(y,z)\mathcal{G}_i^{3\mathrm{D}}\phi(y,z), \tag{A.3}$$

We approximate the azimuthal part of the wavefunction as an anisotropic Gaussian[1]

$$\phi_i(y,z) = \frac{\mathrm{e}^{-(\eta_i y^2 + z^2/\eta_i)/2l^2}}{\sqrt{\pi}l}, \tag{A.4}$$

with $\int dydz|\phi_i|^2 = 1$, $\eta_i = \frac{l_{zi}}{l_{yi}}$ and $l_i = \sqrt{l_{yi}l_{zi}}$.
Inserting Eq. (A.4) into Eq. (A.3) yields

$$\mathcal{L}_{1D} = \int dydz\phi_i^*\left[-\frac{\hbar^2\nabla^2}{2m_i} + V_i(\mathbf{r}) + \sum_j g_{ij}n_j^{3\mathrm{D}}(\mathbf{r}) + \sum_j \Phi_{ij}(\mathbf{r})\right]\phi_i \tag{A.5}$$

[1] In main text we use an isotropic Gaussian.

To calculate the integral the following expressions are useful.

$$\partial_y^2 \phi_i = \left(\frac{\eta_i^2 y^2}{l_i^4} - \frac{\eta_i}{l_i^2} \right) \phi_i \tag{A.6}$$

$$\partial_z^2 \phi_i = \left(\frac{z^2}{\eta_i^2 l_i^4} - \frac{1}{\eta_i l_i^2} \right) \phi_i \tag{A.7}$$

$$\int_{-\infty}^{\infty} dx \mathrm{e}^{-ax^2} = \frac{\sqrt{\pi}}{\sqrt{a}} \tag{A.8}$$

$$\int_{-\infty}^{\infty} dx x^2 \mathrm{e}^{-ax^2} = \frac{\sqrt{\pi}}{2a^{\frac{3}{2}}} \tag{A.9}$$

$$\int_{-\infty}^{\infty} dy dz y^2 \frac{\mathrm{e}^{-(\eta_i y^2 + z^2/\eta_i)/l_i^2}}{\pi l_i^2} = \frac{l_i^2}{2\eta_i} \tag{A.10}$$

$$\int_{-\infty}^{\infty} dy dz z^2 \frac{\mathrm{e}^{-(\eta_i y^2 + z^2/\eta_i)/l_i^2}}{\pi l_i^2} = \frac{\eta_i l_i^2}{2} \tag{A.11}$$

$$\int_{-\infty}^{\infty} dy dz \frac{\mathrm{e}^{-(\eta_i y^2 + z^2/\eta_i)/l_i^2}}{\pi l_i^2} \frac{\mathrm{e}^{-(\eta_j y^2 + z^2/\eta_j)/l_j^2}}{\pi l_j^2} = \int_{-\infty}^{\infty} dz \frac{\mathrm{e}^{-\frac{\left(\eta_j l_j^2 + \eta_i l_i^2\right) z^2}{\eta_i \eta_j l_i^2 l_j^2}}}{\pi^{\frac{3}{2}} l_i l_j \sqrt{\eta_i l_j^2 + \eta_j l_i^2}} \tag{A.12}$$

$$= \sqrt{\frac{\eta_i \eta_j l_i^2 l_j^2}{\left(\eta_j l_j^2 + \eta_i l_i^2\right)}} \frac{1}{\pi l_i l_j \sqrt{\eta_i l_j^2 + \eta_j l_i^2}} = \frac{1}{2\pi \sqrt{(l_i^2 \eta_i + l_j^2 \eta_j)(l_i^2/\eta_i + l_j^2/\eta_j)}} = \frac{1}{2\pi l_{ij}^2} \tag{A.13}$$

$$\text{with} \quad l_{ij}^2 = \frac{\sqrt{(l_i^2 \eta_i + l_j^2 \eta_j)(l_i^2/\eta_i + l_j^2/\eta_j)}}{2}.$$

$$\int dy dz \phi_i^* \partial_y^2 \phi_i = \int dy dz \left(\frac{\eta_i^2 y^2}{l_i^4} - \frac{\eta_i}{l_i^2} \right) |\phi_i|^2 \tag{A.14}$$

$$= -\frac{\eta_i}{l_i^2} + \int_{-\infty}^{\infty} dz \frac{\sqrt{\eta_i}\, \mathrm{e}^{-\frac{z^2}{\eta_i l_i^2}}}{2\sqrt{\pi}\, l_i^3} = -\frac{\eta_i}{l_i^2} + \frac{\eta_i}{2l_i^2} = \frac{\eta_i}{2l_i^2} \tag{A.15}$$

$$\int dy dz \phi_i^* \partial_z^2 \phi_i = \int dy dz \left(\frac{z^2}{\eta_i^2 l_i^4} - \frac{1}{\eta_i l_i^2} \right) |\phi_i|^2 \tag{A.16}$$

$$= -\frac{1}{\eta_i l_i^2} + \int_{-\infty}^{\infty} dy \frac{\mathrm{e}^{-\frac{\eta_i y^2}{l_i^2}}}{2\sqrt{\pi}\sqrt{\eta_i}\, l_i^3} = -\frac{1}{\eta_i l_i^2} + \frac{1}{2\eta_i l_i^2} = -\frac{1}{2\eta_i l_i^2} \tag{A.17}$$

We split this integral (A.5) into three separate integrals to have a better overview.

$$-\int dydz\phi_i^*\frac{\hbar^2\nabla^2}{2m_i}\phi_i = -\frac{\hbar^2}{2m_i}\left(\partial_x^2 + \int dydz\phi_i^*(\partial_y^2+\partial_z^2)\phi_i\right) = -\frac{\hbar^2}{2m_i}\partial_x^2 + \frac{\hbar^2}{4m_i l_i^2}\left(\eta_i + \frac{1}{\eta_i}\right) \tag{A.18}$$

$$\begin{aligned}\int dydz\phi_i^* V_i(\mathbf{r})\phi_i &= \frac{1}{2}m_i\left(\omega_{xi}^2x^2 + \int dydz\left(\omega_{yi}^2y^2+\omega_{zi}^2z^2\right)|\phi_i|^2\right)\\ &= \frac{1}{4}m_i\left[2\omega_{xi}^2x^2 + l_i^2\left(\frac{\omega_{yi}^2}{\eta_i}+\omega_{zi}^2\eta_i\right)\right]\end{aligned} \tag{A.19}$$

$$\int dydz|\phi_i|^2|\phi_j|^2 g_{ij}|\psi_j(x)|^2 = \frac{g_{ij}}{2\pi l_{ij}^2}|\psi_j(x)|^2. \tag{A.20}$$

Notice that the derivation of the DDI part is missing. More information on that derivation can be found in [103].
Finally we get

$$i\hbar\partial_t\psi_i = \left(-\frac{\hbar^2}{2m_i}\partial_x^2 + \sum_j\frac{g_{ij}n_j}{2\pi l^2} + \sum_j\Phi_{ij}(x)\right)\psi_i, \tag{A.21}$$

or rather

$$\mathcal{G}_i^{1D}\psi_i = \left(-\frac{\hbar^2}{2m_i}\partial_x^2 + \sum_j\frac{g_{ij}n_j}{2\pi l^2} + \frac{1}{2}m_i\omega_{xi}^2x^2 + \sum_j\Phi_{ij}(x) + \mathcal{E}_i\right)\psi_i, \tag{A.22}$$

with

$$\mathcal{E}_i = \frac{\hbar^2}{4m_i l^2}\left(\eta_i+\frac{1}{\eta_i}\right) + \frac{1}{4}m_i l^2\left(\frac{\omega_{yi}^2}{\eta_i}+\eta_i\omega_{zi}^2\right) \tag{A.23}$$

and

$$\Phi_{ij}(x) = \mathcal{F}_x^{-1}\left\{U_{ij}(k_x)\mathcal{F}_x\left[|\psi_j|^2\right]\right\}, \tag{A.24}$$

where

$$U_{ij}(k_x) = \frac{g_{ij}^{dd}}{2\pi l^2}U_\alpha(0)\left[1+3Q_\alpha^2\exp\left\{Q_\alpha^2\right\}\mathrm{Ei}(-Q_\alpha^2)\right], \tag{A.25}$$

with $U_\alpha(0) = (1-3\cos^2(\alpha))/2$, $Q^2(\alpha=\pi/2) = \frac{1}{2}k_x^2l^2$. Notice that

$$\mathrm{Ei}(-Q_\alpha^2) = -\mathrm{E}_1(Q_\alpha^2), \tag{A.26}$$

and with that we get

$$U_{ij}(k_x) = \frac{g_{ij}^{dd}}{2\pi l^2}U_\alpha(0)\left[1-3Q_\alpha^2\exp\left\{Q_\alpha^2\right\}\mathrm{E}_1(Q_\alpha^2)\right]. \tag{A.27}$$

A.2. Derivation of the Bogoliubov dispersion relations for binary dipolar quasi-1D BECs

In this appendix, we derive the Bogoliubov dispersion relations (6.13) described in the main text in detail. We consider solutions to the two-component quasi-1D GPE with a small density perturbation around a uniform background density. Substituting this ansatz into the GPE and retaining only terms up to linear order results in a 4×4 matrix equation. The positive eigenvalues of this matrix correspond to the dispersion relations.
We start with the two component quasi-1D GPE

$$i\hbar\frac{\partial\psi_i}{\partial t} = \left(H_0 + \sum_j \frac{g_{ij}|\psi_j|^2}{2\pi l^2} + \sum_j \Phi_{ij}(x)\right)\psi_i, \tag{A.28}$$

with

$$H_0 = -\frac{\hbar^2}{2m_i}\partial_x^2 + \frac{1}{2}m_i\omega_{xi}^2 x^2 + \mathcal{E}_i \tag{A.29}$$

and

$$\mathcal{E}_i = \frac{\hbar^2}{4m_i l^2}\left(\eta_i + \frac{1}{\eta_i}\right) + \frac{1}{4}m_i l^2\left(\frac{\omega_{yi}^2}{\eta_i} + \eta_i\omega_{zi}^2\right) \tag{A.30}$$

and

$$\Phi_{ij}(x) = \mathcal{F}_x^{-1}\left\{U_{ij}(k_x)\mathcal{F}_x\left[|\psi_j|^2\right]\right\}, \tag{A.31}$$

where

$$U_{ij}(k_x) = \frac{g_{ij}^{dd}}{2\pi l^2}U_\alpha(0)\left[1 + 3Q_\alpha^2\exp\left\{Q_\alpha^2\right\}\mathrm{Ei}(-Q_\alpha^2)\right], \tag{A.32}$$

with $U_\alpha(0) = (1 - 3\cos^2(\alpha))/2$, $Q^2(\alpha = \pi/2) = \frac{1}{2}k_x^2 l^2$. The quantities are defined as in Sec. 6.2, except that the particle mass and trapping parameters may differ between components..
We look at solutions of the form:

$$\psi_i(x,t) = \left(\sqrt{n_0^{(i)}} + \lambda\left[u_i(x)e^{-i\epsilon t/\hbar} - v_i^*(x)e^{i\epsilon^* t/\hbar}\right]\right)e^{-i\mu_i t/\hbar}, \tag{A.33}$$

where the condensate is perturbed via a small parameter λ around the average density $n_0^{(i)} = \left|\psi_0^{(i)}\right|^2$ with $\psi_0^{(i)} = \sqrt{N_i/L}$. We describe the perturbation in form of the Bogoliubov amplitudes u_i and v_i. Expanding the contact interaction term

$$\frac{1}{2\pi l^2}\sum_j g_{ij}|\psi_j|^2 \tag{A.34}$$

$$= \frac{1}{2\pi l^2}\sum_j g_{ij}\left(\sqrt{n_0^{(j)}} + \lambda\left[u_j(x)e^{-i\epsilon t/\hbar} - v_j^*(x)e^{i\epsilon t/\hbar}\right]\right)\left(\sqrt{n_0^{(j)}} + \lambda\left[u_j^*(x)e^{i\epsilon^* t/\hbar} - v_j(x)e^{-i\epsilon t/\hbar}\right]\right) \tag{A.35}$$

keeping only terms up to linear order in λ

$$\frac{1}{2\pi l^2}\sum_j g_{ij}|\psi_j|^2 \tag{A.36}$$

$$=\frac{1}{2\pi l^2}\sum_j g_{ij}\left(n_0^{(j)}+\lambda\sqrt{n_0^{(j)}}\left[u_j(x)e^{-i\epsilon t/\hbar}-v_j^*(x)e^{i\epsilon t/\hbar}\right]+\lambda\sqrt{n_0^{(j)}}\left[u_j^*(x)e^{i\epsilon^* t/\hbar}-v_j(x)e^{-i\epsilon t/\hbar}\right]\right). \tag{A.37}$$

We then multiply the contact interaction term by ψ_i from the right. Keeping only terms linear in λ gives

$$\frac{1}{2\pi l^2}\sum_j g_{ij}|\psi_j|^2\psi_i \tag{A.38}$$

$$=\frac{1}{2\pi l^2}\sum_j g_{ij}\left(n_0^{(j)}+\lambda\sqrt{n_0^{(j)}}\left[u_j(x)e^{-i\epsilon t/\hbar}-v_j^*(x)e^{i\epsilon t/\hbar}\right]+\lambda\sqrt{n_0^{(j)}}\left[u_j^*(x)e^{i\epsilon^* t/\hbar}-v_j(x)e^{-i\epsilon t/\hbar}\right]\right)\psi_i \tag{A.39}$$

$$=\frac{1}{2\pi l^2}\sum_j g_{ij}\Big(n_0^{(j)}\sqrt{n_0^{(i)}}+\lambda\sqrt{n_0^{(j)}}\sqrt{n_0^{(i)}}\left[u_j(x)e^{-i\epsilon t/\hbar}-v_j^*(x)e^{i\epsilon t/\hbar}\right] \tag{A.40}$$

$$+\lambda\sqrt{n_0^{(j)}}\sqrt{n_0^{(i)}}\left[u_j^*(x)e^{i\epsilon^* t/\hbar}-v_j(x)e^{-i\epsilon t/\hbar}\right]+\lambda n_0^{(j)}\left[u_i(x)e^{-i\epsilon t/\hbar}-v_i^*(x)e^{i\epsilon t/\hbar}\right]\Big)e^{-i\mu t/\hbar}. \tag{A.41}$$

Expanding the Dipol-Dipol interaction term

$$\Phi_{ij}(x)=\mathcal{F}_x^{-1}\left\{\tilde{U}_{ij}(k_x)\mathcal{F}_x\left[|\psi_j|^2\right]\right\} \tag{A.42}$$

$$=\mathcal{F}_x^{-1}\left\{\tilde{U}_{ij}(k_x)\mathcal{F}_x\left[\left(\sqrt{n_0^{(j)}}+\lambda\left[u_j(x)e^{-i\epsilon t/\hbar}-v_j^*(x)e^{i\epsilon t/\hbar}\right]\right)\left(\sqrt{n_0^{(j)}}+\lambda\left[u_j^*(x)e^{i\epsilon^* t/\hbar}-v_j(x)e^{-i\epsilon t/\hbar}\right]\right)\right]\right\} \tag{A.43}$$

keeping only terms up to linear order in λ

$$\Phi_{ij}(x)=\mathcal{F}_x^{-1}\left\{\tilde{U}_{ij}(k_x)\mathcal{F}_x\left[|\psi_j|^2\right]\right\} \tag{A.44}$$

$$=\mathcal{F}_x^{-1}\left\{\tilde{U}_{ij}(k_x)\mathcal{F}_x\left[\left(n_0^{(j)}+\lambda\sqrt{n_0^{(j)}}\left[u_j(x)e^{-i\epsilon t/\hbar}-v_j^*(x)e^{i\epsilon t/\hbar}\right]+\lambda\sqrt{n_0^{(j)}}\left[u_j^*(x)e^{i\epsilon^* t/\hbar}-v_j(x)e^{-i\epsilon t/\hbar}\right]\right)\right]\right\} \tag{A.45}$$

We then multiply the dipole-dipole interaction term by ψ_i from the right. Keeping only terms linear in λ gives

$$\Phi_{ij}(x)=\mathcal{F}_x^{-1}\left\{\tilde{U}_{ij}(k_x)\mathcal{F}_x\left[|\psi_j|^2\right]\right\}\psi_i \tag{A.46}$$

$$=\mathcal{F}_x^{-1}\left\{\tilde{U}_{ij}(k_x)\mathcal{F}_x\left[\left(n_0^{(j)}+\lambda\sqrt{n_0^{(j)}}\left[u_j(x)e^{-i\epsilon t/\hbar}-v_j^*(x)e^{i\epsilon t/\hbar}\right]+\lambda\sqrt{n_0^{(j)}}\left[u_j^*(x)e^{i\epsilon^* t/\hbar}-v_j(x)e^{-i\epsilon t/\hbar}\right]\right)\right]\right\}\psi_i \tag{A.47}$$

$$=\mathcal{F}_x^{-1}\left\{\tilde{U}_{ij}(k_x)\mathcal{F}_x\left[n_0^{(j)}\right]\right\}(\sqrt{n_0^{(i)}}+\lambda\left[u_i(x)e^{-i\epsilon t/\hbar}-v_i^*(x)e^{i\epsilon t/\hbar}\right])e^{-i\mu t/\hbar}+ \tag{A.48}$$

$$\mathcal{F}_x^{-1}\left\{\tilde{U}_{ij}(k_x)\mathcal{F}_x\left[\left(\lambda\sqrt{n_0^{(j)}}\left[u_j(x)e^{-i\epsilon t/\hbar}-v_j^*(x)e^{i\epsilon t/\hbar}\right]+\lambda\sqrt{n_0^{(j)}}\left[u_j^*(x)e^{i\epsilon^* t/\hbar}-v_j(x)e^{-i\epsilon t/\hbar}\right]\right)\right]\right\} \tag{A.49}$$

$$\times\sqrt{n_0^{(i)}}e^{-i\mu t/\hbar} \tag{A.50}$$

The time derivative of the 1D GPE is

$$i\hbar\frac{\partial\psi_i(x,t)}{\partial t} = \left\{\mu_i\sqrt{n_0^{(i)}} + \lambda\left[(\epsilon+\mu_i)u_i e^{-i\epsilon t/\hbar} + (\epsilon^*-\mu_i)v_i^* e^{i\epsilon^* t/\hbar}\right]\right\} e^{-i\mu t/\hbar}. \tag{A.51}$$

Now inserting everything into the 1D GPE gives

$$\begin{aligned}
&\left\{\mu_i\sqrt{n_0^{(i)}} + \lambda\left[(\epsilon+\mu_i)u_i e^{-i\epsilon t/\hbar} + (\epsilon^*-\mu_i)v_i^* e^{i\epsilon^* t/\hbar}\right]\right\} e^{-i\mu t/\hbar}\\
=&H_0\left(\sqrt{n_0^{(i)}} + \lambda\left[u_i e^{-i\epsilon t/\hbar} - v_i^* e^{i\epsilon^* t/\hbar}\right]\right) e^{-i\mu_i t/\hbar} +\\
&\frac{1}{2\pi l^2}\sum_j g_{ij}\Big(n_0^{(j)}\sqrt{n_0^{(i)}} + \lambda\sqrt{n_0^{(j)}}\sqrt{n_0^{(i)}}\left[u_j e^{-i\epsilon t/\hbar} - v_j^* e^{i\epsilon t/\hbar}\right] +\\
&\lambda\sqrt{n_0^{(j)}}\sqrt{n_0^{(i)}}\left[u_j^* e^{i\epsilon^* t/\hbar} - v_j e^{-i\epsilon t/\hbar}\right] + \lambda n_0^{(j)}\left[u_i e^{-i\epsilon t/\hbar} - v_i^* e^{i\epsilon t/\hbar}\right]\Big) e^{-i\mu t/\hbar} +\\
&\sum_j \mathcal{F}_x^{-1}\left\{\tilde{U}_{ij}(k_x)\mathcal{F}_x\left[n_0^{(j)}\right]\right\}\left(\sqrt{n_0^{(i)}} + \lambda\left[u_i e^{-i\epsilon t/\hbar} - v_i^* e^{i\epsilon t/\hbar}\right]\right) e^{-i\mu t/\hbar} +\\
&\sum_j \mathcal{F}_x^{-1}\left\{\tilde{U}_{ij}(k_x)\mathcal{F}_x\left[\left(\lambda\sqrt{n_0^{(j)}}\left[u_j e^{-i\epsilon t/\hbar} - v_j^* e^{i\epsilon t/\hbar}\right] + \lambda\sqrt{n_0^{(j)}}\left[u_j^* e^{i\epsilon^* t/\hbar} - v_j e^{-i\epsilon t/\hbar}\right]\right)\right]\right\}\sqrt{n_0^{(i)}} e^{-i\mu t/\hbar}
\end{aligned} \tag{A.52}$$

The terms without λ fall away (they give a 1D GPE for $\psi_i = \sqrt{n_0^{(i)}}e^{-i\mu t/\hbar}$. Dividing both sides by $e^{-i\mu t/\hbar}$ gives

$$\begin{aligned}
&\lambda\left[(\epsilon+\mu_i)u_i e^{-i\epsilon t/\hbar} + (\epsilon^*-\mu_i)v_i^* e^{i\epsilon^* t/\hbar}\right] = H_0\lambda\left[u_i e^{-i\epsilon t/\hbar} - v_i^* e^{i\epsilon^* t/\hbar}\right] +\\
&\frac{1}{2\pi l^2}\sum_j g_{ij}\Big(\lambda\sqrt{n_0^{(j)}}\sqrt{n_0^{(i)}}\left[u_j e^{-i\epsilon t/\hbar} - v_j^* e^{i\epsilon t/\hbar}\right] +\\
&\lambda\sqrt{n_0^{(j)}}\sqrt{n_0^{(i)}}\left[u_j^* e^{i\epsilon^* t/\hbar} - v_j e^{-i\epsilon t/\hbar}\right] + \lambda n_0^{(j)}\left[u_i e^{-i\epsilon t/\hbar} - v_i^* e^{i\epsilon t/\hbar}\right]\Big) +\\
&\sum_j \mathcal{F}_x^{-1}\left\{\tilde{U}_{ij}(k_x)\mathcal{F}_x\left[n_0^{(j)}\right]\right\}\lambda\left[u_i e^{-i\epsilon t/\hbar} - v_i^* e^{i\epsilon t/\hbar}\right] +\\
&\sum_j \mathcal{F}_x^{-1}\left\{\tilde{U}_{ij}(k_x)\mathcal{F}_x\left[\left(\lambda\sqrt{n_0^{(j)}}\left[u_j e^{-i\epsilon t/\hbar} - v_j^* e^{i\epsilon t/\hbar}\right] + \lambda\sqrt{n_0^{(j)}}\left[u_j^* e^{i\epsilon^* t/\hbar} - v_j e^{-i\epsilon t/\hbar}\right]\right)\right]\right\}\sqrt{n_0^{(i)}}
\end{aligned} \tag{A.53}$$

Collecting terms evolving in time with $e^{-i\epsilon t/\hbar}$ and $e^{i\epsilon^* t/\hbar}$ gives the coupled equations

$$\begin{aligned}
&(\epsilon+\mu_i)u_i(x) = H_0 u_i(x) + \frac{1}{2\pi l^2}\sum_j g_{ij}\left(\sqrt{n_0^{(i)}}\sqrt{n_0^{(j)}}u_j(x) - \sqrt{n_0^{(i)}}\sqrt{n_0^{(j)}}v_j(x) + n_j u_i(x)\right) +\\
&\sum_j \mathcal{F}_x^{-1}\left\{\tilde{U}_{ij}(k_x)\mathcal{F}_x\left[\left(\sqrt{n_0^{(j)}}u_j(x) - \sqrt{n_0^{(j)}}v_j(x)\right)\right]\right\}\sqrt{n_0^{(i)}} + \sum_j \mathcal{F}_x^{-1}\left\{\tilde{U}_{ij}(k_x)\mathcal{F}_x\left[n_0^{(j)}\right]\right\}u_i(x)
\end{aligned} \tag{A.54}$$

and

$$(\epsilon^* - \mu_i)v_i^*(x) = -H_0 v_i^*(x) + \frac{1}{2\pi l^2}\sum_j g_{ij}\left(\sqrt{n_0^{(i)}}\sqrt{n_0^{(j)}}u_j^*(x) - \sqrt{n_0^{(i)}}\sqrt{n_0^{(j)}}v_j^*(x) - n_j v_i^*(x)\right) + \sum_j \mathcal{F}_x^{-1}\left\{\tilde{U}_{ij}(k_x)\mathcal{F}_x\left[\left(\sqrt{n_0^{(j)}}u_j^*(x) - \sqrt{n_0^{(j)}}v_j^*(x)\right)\right]\right\}\sqrt{n_0^{(i)}} - \sum_j \mathcal{F}_x^{-1}\left\{\tilde{U}_{ij}(k_x)\mathcal{F}_x\left[n_0^{(j)}\right]\right\}v_i^*(x) \tag{A.55}$$

We take the c.c of the second equation and assume that μ_i is real

$$(\epsilon - \mu_i)v_i(x) = -H_0 v_i(x) + \frac{1}{2\pi l^2}\sum_j g_{ij}\left(\sqrt{n_0^{(i)}}\sqrt{n_0^{(j)}}u_j(x) - \sqrt{n_0^{(i)}}\sqrt{n_0^{(j)}}v_j(x) - n_j v_i(x)\right) + \sum_j \mathcal{F}_x^{-1}\left\{\tilde{U}_{ij}(k_x)\mathcal{F}_x\left[\left(\sqrt{n_0^{(j)}}u_j(x) - \sqrt{n_0^{(j)}}v_j(x)\right)\right]\right\}\sqrt{n_0^{(i)}} - \sum_j \mathcal{F}_x^{-1}\left\{\tilde{U}_{ij}(k_x)\mathcal{F}_x\left[n_0^{(j)}\right]\right\}v_i(x) \tag{A.56}$$

Rewriting and using Eq. (4.29) gives us for the coupled equations

$$\begin{aligned}\epsilon u_i(x) = H_0 u_i(x) + \frac{\sqrt{n_0^{(i)}}}{2\pi l^2}\sum_j g_{ij}\sqrt{n_0^{(j)}}\left[u_j(x) - v_j(x)+\right] + \\ \sqrt{n_0^{(i)}}\sum_j \sqrt{n_0^{(j)}}\mathcal{F}_x^{-1}\left\{\tilde{U}_{ij}(k_x)\mathcal{F}_x\left[u_j(x) - v_j(x)\right]\right\}\end{aligned} \tag{A.57}$$

and

$$\begin{aligned}\epsilon v_i(x) = -H_0 v_i(x) + \frac{\sqrt{n_0^{(i)}}}{2\pi l^2}\sum_j g_{ij}\sqrt{n_0^{(j)}}\left[u_j(x) - v_j(x)\right] + \\ \sqrt{n_0^{(i)}}\sum_j \sqrt{n_0^{(j)}}\mathcal{F}_x^{-1}\left\{\tilde{U}_{ij}(k_x)\mathcal{F}_x\left[u_j(x) - v_j(x)\right]\right\}\end{aligned} \tag{A.58}$$

Moving to momentum space $\left(\mathcal{F}_x[a(x)] = \tilde{a}(k)\right)$ gives

$$\epsilon\tilde{u}_i(k) = \frac{\hbar^2 k^2}{2m}\tilde{u}_i(k) + \frac{\sqrt{n_0^{(i)}}}{2\pi l^2}\sum_j g_{ij}\sqrt{n_0^{(j)}}\left[\tilde{u}_j(k) - \tilde{v}_j(k)\right] + \sqrt{n_0^{(i)}}\sum_j \tilde{U}_{ij}(k)\sqrt{n_0^{(j)}}\left[\tilde{u}_j(k) - \tilde{v}_j(k)\right] \tag{A.59}$$

and

$$\epsilon\tilde{v}_i(k) = -\frac{\hbar^2 k^2}{2m}\tilde{v}_i(k) + \frac{\sqrt{n_0^{(i)}}}{2\pi l^2}\sum_j g_{ij}\sqrt{n_0^{(j)}}\left[\tilde{u}_j(k) - \tilde{v}_j(k)\right] + \sqrt{n_0^{(i)}}\sum_j \tilde{U}_{ij}(k)\sqrt{n_0^{(j)}}\left[\tilde{u}_j(k) - \tilde{v}_j(k)\right], \tag{A.60}$$

where we have used the convolution theorem and assumed that $\omega_x = 0$ and $\mathcal{E}_i = 0$. The coupled equations can be written in 4x4 matrix equation of the form $\epsilon\mathbf{w} = M\mathbf{w}$, where

$\mathbf{w} = \{\tilde{u}_1, \tilde{u}_2, \tilde{v}_1, \tilde{v}_2\}$ and $M =$

$$\begin{pmatrix} \frac{\hbar^2k^2}{2m} + \frac{n_1}{2\pi l^2}g_{11} + n_1U_{11} & \frac{\sqrt{n_1n_2}}{2\pi l^2}g_{12} + \sqrt{n_1n_2}U_{12} & -\frac{n_1}{2\pi l^2}g_{11} - n_1U_{11} & -\frac{\sqrt{n_1n_2}}{2\pi l^2}g_{12} - \sqrt{n_1n_2}U_{12} \\ \frac{\sqrt{n_1n_2}}{2\pi l^2}g_{12} + \sqrt{n_1n_2}U_{12} & \frac{\hbar^2k^2}{2m} + \frac{n_2}{2\pi l^2}g_{22} + n_2U_{22} & -\frac{\sqrt{n_1n_2}}{2\pi l^2}g_{12} - \sqrt{n_1n_2}U_{12} & -\frac{n_2}{2\pi l^2}g_{22} - n_2U_{22} \\ \frac{n_1}{2\pi l^2}g_{11} + n_1U_{11} & \frac{\sqrt{n_1n_2}}{2\pi l^2}g_{12} + \sqrt{n_1n_2}U_{12} & -\frac{\hbar^2k^2}{2m} - \frac{n_1}{2\pi l^2}g_{11} - n_1U_{11} & -\frac{\sqrt{n_1n_2}}{2\pi l^2}g_{12} - \sqrt{n_1n_2}U_{12} \\ \frac{\sqrt{n_1n_2}}{2\pi l^2}g_{12} + \sqrt{n_1n_2}U_{12} & \frac{n_2}{2\pi l^2}g_{22} + n_2U_{22} & -\frac{\sqrt{n_1n_2}}{2\pi l^2}g_{12} - \sqrt{n_1n_2}U_{12} & -\frac{\hbar^2k^2}{2m} - \frac{n_2}{2\pi l^2}g_{22} - n_2U_{22} \end{pmatrix} \tag{A.61}$$

where $g_{12} = g_{21}$ and $U_{12} = U_{21}$.
The matrix can be diagonalised and one gets the four eigenvalues $\{\epsilon_+, \epsilon_-, -\epsilon_-, -\epsilon_+\}$. However we disregard the negative solutions in the following.
The eigenvalues are determined by

$$\epsilon_\pm^2(k) = \frac{\epsilon_1^2 + \epsilon_2^2}{2} \pm \frac{1}{2}\sqrt{(\epsilon_1^2 - \epsilon_2^2)^2 + 4G_{12}G_{12}\frac{\hbar^4k^4}{m_im_j}}, \tag{A.62}$$

where the quasiparticle mode energies are

$$\epsilon_i^2(k) = \frac{\hbar^2k^2}{2m_i}\left(\frac{\hbar^2k^2}{2m_i} + 2G_{ii}(k)\right), \tag{A.63}$$

with

$$G_{ij}(k) = \sqrt{n_in_j}\frac{g_{ij}}{2\pi l^2} + \sqrt{n_in_j}\tilde{U}_{ij} \tag{A.64}$$

To get to dimensionless units we devide Eq. (A.62) by $\hbar^2\omega_0^2$ and get

$$\tilde{\epsilon}_\pm^2(k) = \frac{\tilde{\epsilon}_1^2 + \tilde{\epsilon}_2^2}{2} \pm \frac{1}{2}\sqrt{(\tilde{\epsilon}_1^2 - \tilde{\epsilon}_2^2)^2 + 4\tilde{G}_{12}\tilde{G}_{12}\tilde{k}^4}, \tag{A.65}$$

where

$$\tilde{\epsilon}_i^2 = \frac{\tilde{k}^2}{2}\left(\frac{\tilde{k}^2}{2} + 2\tilde{G}_{ii}\right), \tag{A.66}$$

$$\tilde{G}_{ij}(k) = \sqrt{\tilde{n}_i\tilde{n}_j}\frac{\tilde{g}_{ij}}{\tilde{l}^2} + \sqrt{\tilde{n}_i\tilde{n}_j}\frac{\tilde{g}_{ij}^{dd}}{\tilde{l}^2}\tilde{U}_0(k), \tag{A.67}$$

$$k = \tilde{k}k_0, \quad k_0 = \sqrt{\frac{m\omega_0}{\hbar}} = \frac{1}{x_0}, \quad \tilde{n}_i = \frac{N_ix_0}{L_x10^{-6}}, \tag{A.68}$$

$$\tilde{U}_0(k) = U_\alpha(0)\left[1 - 3Q_\alpha^2\exp\left\{Q_\alpha^2\right\}\mathrm{E}_1(Q_\alpha^2)\right]. \tag{A.69}$$

where L_x is the grid size in μm and $U_\alpha(0) = (1 - 3\cos^2(\alpha))/2$, $Q(\alpha = \pi/2) = \frac{1}{2}k_x^2l^2$.

A.3. Interplay between SI-units and computational-units

For numerical simulations, we divide our key equations (4.26, 6.13) by an in principle arbitrary ω_0 to get dimensionless units for those equations. Usually one takes ω_0 to be equal

to the trap frequency that is affecting the timescale of the dynamics the most. For us that would be the radial trap. However, with a different choice of ω_0 all computational units change and thus also the numerical solutions, but they correspond to the same numerical results, only everything is rescaled. Transforming back with the same ω_0 to SI-units results in the same numerical solutions for a given set of parameters.
On the other hand we can transform from the computational units back to SI-units with a different ω_0'. This gives us rescaled SI-units, leaving us some freedom of connecting different regimes of *e.g.* quasi-1D regime with each other.
We start with the GPE (5.1) in computational units. For a given simulation the fixed parameters are (all dimensionless) the contact interaction term c_{ij}, the tube length $\tilde{L}$, the time $\tilde{t}$ and the particle energy $\tilde{E}$. If we have dipoles present the dipole-dipole interaction d_{ij} and the parameter Q are fixed as well. The latter fixes the characteristic length $\tilde{l}$. The parameters are given by

$$\begin{aligned} c_{ij} = \frac{2a_{ij}N_j}{x_0\tilde{l}^2}, \quad \tilde{t} = t\omega_0, \quad \tilde{L} = L/x_0, \quad \tilde{E} = \frac{E}{N\hbar\omega_0} \\ \tilde{l} = \sqrt{\omega_0/\omega}, \quad d_{ij} = \frac{2a_{ij}^{dd}N_j}{x_0\tilde{l}^2}, \quad Q_\alpha^2 = \frac{1}{2}\tilde{k}_x^2\tilde{l}^2. \end{aligned} \tag{A.70}$$

In the following we want to keep a_{ij} and a_{ij}^{dd} fixed. Considering the transformation of $\omega_0 \to \omega_0'$ we get the following condition

$$\frac{N_j}{x_0\tilde{l}^2} = \frac{N_j'}{x_0'\tilde{l}'^2}, \tag{A.71}$$

to keeping a_{ij} and a_{ij}^{dd} unchanged.
We now want to consider the condition of a system being in the quasi-1D regime $n_j a_{ij} \ll 1$, which becomes

$$\implies n_j a_{ij} = \frac{N_j}{\tilde{L}x_0}\frac{c_{ij}\tilde{l}^2}{2N_j} = \frac{c_{ij}\tilde{l}^2}{2\tilde{L}} \ll 1. \tag{A.72}$$

We see that for a system with dipole-dipole interactions $a_{ij}^{dd} \neq 0$ this is invariant under a transformation of $\omega_0 \to \omega_0'$ for a given simulation. For $a_{ij}^{dd} = 0$, however, $\tilde{l}$ is a free parameter. In that case we can change the SI-units in such a way, that it changes the regime we are in. The key is to change ω_0 while keeping ω fixed or vice versa.
The transformation $\omega_0 \to \omega_0' = x\omega_0$ results in $N_j' = N\sqrt{x}$ and $n_j'a_{ij}' = \sqrt{x}n_j'a_{ij}'$, while transforming the radial trap frequency $\omega \to \omega' = x\omega$ results in $N_j' = N/x$ and $n_j'a_{ij}' = n_j'a_{ij}'/x$.
Transforming back to SI-Units we find the following behaviour under a transformation of

$\omega_0 \to \omega_0'$ and $\omega \to \omega'$

$$\begin{aligned} N' &= N\sqrt{\frac{\omega_0'}{\omega_0}}\frac{\omega}{\omega'} \\ L' &= L\sqrt{\frac{\omega_0}{\omega_0'}} \\ t' &= t\frac{\omega_0'}{\omega_0} \\ E' &= E\frac{{\omega_0'}^{3/2}}{\omega_0^{3/2}}\frac{\omega}{\omega'} \\ \Delta x' &= \Delta x\sqrt{\frac{\omega_0}{\omega_0'}} \\ a_{ij}' &= a_{ij}. \end{aligned} \tag{A.73}$$

This is possible for $a_{ij}^{dd} \neq 0$ as well but $\omega_0/\omega = \omega_0'/\omega'$ has to be fulfilled. The transinformation simplify to

$$\begin{aligned} N' &= N\sqrt{\frac{\omega_0}{\omega_0'}} \\ L' &= L\sqrt{\frac{\omega_0}{\omega_0'}} \\ t' &= t\frac{\omega_0}{\omega_0'} \\ E' &= E\frac{{\omega_0'}^{3/2}}{\omega_0^{3/2}} \\ \Delta x' &= \Delta x\sqrt{\frac{\omega_0}{\omega_0'}} \\ a_{ij}' &= a_{ij}, \quad a_{ij}^{dd'} = a_{ij}^{dd}. \end{aligned} \tag{A.74}$$

Note that we ignored the zero point energy $E = \hbar\omega$ from the radial confinement. This would fix $\omega_0/\omega = \omega_0'/\omega'$ even in the non-dipolar case. However, this is just a constant energy and can be subtracted out, because we are only interested in relative energies.

A.4. Fitting

In this appendix, we describe the fitting method used for Fig. 6.4 in detail. We fit for three different ranges of $x_1 = [-\nu, \nu]$, $x_2 = [-4\nu, 4\nu]$ and $x_3 = [-12\nu, 12\nu]$, where ν is the position where the phase S is 0.4π, and then take the average. We obtain b from SMSP and PDW by extracting the relative phase ϕ_{rel} of the components from the dynamics when the two magnetic solitons are on top of each other and then fitting ϕ_{rel} to Eq. (5.6) with three different ranges of $x_1 = [-\nu, \nu]$ $x_2 = [-4\nu, 4\nu]$and $x_3 = [-12\nu, 12\nu]$. The domain wall width b is then obtained by taking the mean value of these fits with an error, which is calculated

as the mean square of b. For the PDW it is at the start of the real time evolution. b^{-1} for the red squares generated with PDW is calculated in the same way. An example is shown in Fig. A.1. For SMSP we fit after a quarter period of the oscillation.

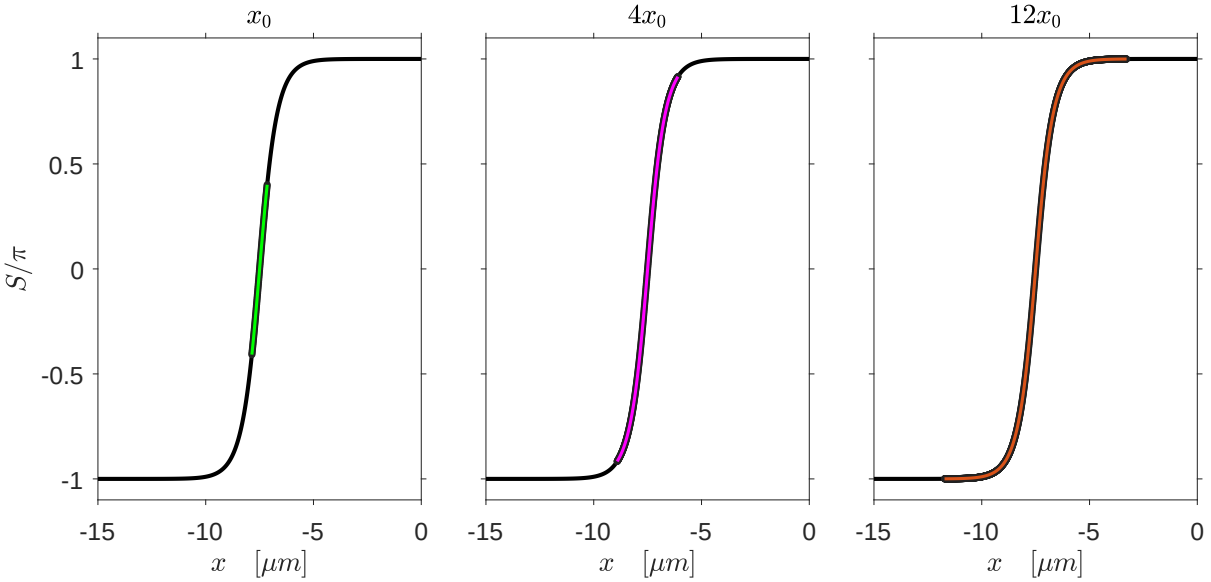

Figure A.1.: Example of the phase fitting procedure of Eq. (5.6) for a PDW with $k = 0.91$. We have the width $x_1 = x_0 = 0.7104\mu$m. The other widths correspond to $x_2 = 4x_0$ and $x_3 = 12x_0$ (see text for more informations).

Bibliography

[1] J. S. Russell, *"Report on Waves". Report of the fourteenth meeting of the British Association for the Advancement of Science, York, September 1844. London: John Murray. 311–390, Plates XLVII–LVII.* (1845). URL https://www.macs.hw.ac.uk/~chris/Scott-Russell/SR44.pdf.

[2] N. J. Zabusky und M. D. Kruskal, *Interaction of "Solitons" in a Collisionless Plasma and the Recurrence of Initial States*, Phys. Rev. Lett., **15**, 240 (1965). URL http://dx.doi.org/10.1103/PhysRevLett.15.240.

[3] C. S. Gardner, J. M. Greene, M. D. Kruskal und R. M. Miura, *Method for Solving the Korteweg-deVries Equation*, Phys. Rev. Lett., **19**, 1095 (1967). URL http://dx.doi.org/10.1103/PhysRevLett.19.1095.

[4] T. Aktosun, *Inverse Scattering Transform and the Theory of Solitons*, S. 4960–4971, Springer New York, New York, NY (2009), ISBN 978-0-387-30440-3. URL http://dx.doi.org/10.1007/978-0-387-30440-3_295.

[5] A. Hasegawa und F. Tappert, *Transmission of stationary nonlinear optical pulses in dispersive dielectric fibers. I. Anomalous dispersion*, Applied Physics Letters, **23**(3), 142 (1973). https://pubs.aip.org/aip/apl/article-pdf/23/3/142/18428001/142_1_online.pdf, URL http://dx.doi.org/10.1063/1.1654836.

[6] H. A. Haus und W. S. Wong, *Solitons in optical communications*, Rev. Mod. Phys., **68**, 423 (1996). URL http://dx.doi.org/10.1103/RevModPhys.68.423.

[7] J. P. Gordon, *Interaction forces among solitons in optical fibers*, Opt. Lett., **8**(11), 596 (1983). URL http://dx.doi.org/10.1364/OL.8.000596.

[8] S. Burger, K. Bongs, S. Dettmer, W. Ertmer, K. Sengstock, A. Sanpera, G. V. Shlyapnikov und M. Lewenstein, *Dark Solitons in Bose-Einstein Condensates*, Phys. Rev. Lett., **83**, 5198 (1999). URL http://dx.doi.org/10.1103/PhysRevLett.83.5198.

[9] L. Pitaevskii und S. Stringari, *Bose-Einstein Condensation and Superfluidity*, Oxford University Press (2016). URL http://dx.doi.org/10.1093/acprof:oso/9780198758884.001.0001.

[10] C. J. Pethick und H. Smith, *Bose–Einstein Condensation in Dilute Gases*, Cambridge University Press, 2 Aufl. (2008). URL http://dx.doi.org/10.1017/CBO9780511802850.

[11] O. Lahav, A. Itah, A. Blumkin, C. Gordon, S. Rinott, A. Zayats und J. Steinhauer, *Realization of a Sonic Black Hole Analog in a Bose-Einstein Condensate*, Phys. Rev. Lett., **105**, 240401 (2010). URL http://dx.doi.org/10.1103/PhysRevLett.105.240401.

[12] J. Steinhauer, *Observation of quantum Hawking radiation and its entanglement in an analogue black hole*, Nature Physics, **12**, 959 (2016). URL http://dx.doi.org/10.1038/nphys3863.

[13] F. Dalfovo, S. Giorgini, L. P. Pitaevskii und S. Stringari, *Theory of Bose-Einstein condensation in trapped gases*, Rev. Mod. Phys., **71**, 463 (1999). URL http://dx.doi.org/10.1103/RevModPhys.71.463.

[14] K. W. Madison, F. Chevy, V. Bretin und J. Dalibard, *Stationary States of a Rotating Bose-Einstein Condensate: Routes to Vortex Nucleation*, Phys. Rev. Lett., **86**, 4443 (2001). URL http://dx.doi.org/10.1103/PhysRevLett.86.4443.

[15] S. Donadello, S. Serafini, M. Tylutki, L. P. Pitaevskii, F. Dalfovo, G. Lamporesi und G. Ferrari, *Observation of Solitonic Vortices in Bose-Einstein Condensates*, Phys. Rev. Lett., **113**, 065302 (2014). URL http://dx.doi.org/10.1103/PhysRevLett.113.065302.

[16] S. Komineas und N. Papanicolaou, *Solitons, solitonic vortices, and vortex rings in a confined Bose-Einstein condensate*, Phys. Rev. A, **68**, 043617 (2003). URL http://dx.doi.org/10.1103/PhysRevA.68.043617.

[17] K. E. S. et. al., *Formation and propagation of matter-wave soliton trains*, Nature, **417**, 150 (2002). URL http://dx.doi.org/10.1038/nature747.

[18] B. P. Anderson, P. C. Haljan, C. A. Regal, D. L. Feder, L. A. Collins, C. W. Clark und E. A. Cornell, *Watching Dark Solitons Decay into Vortex Rings in a Bose-Einstein Condensate*, Phys. Rev. Lett., **86**, 2926 (2001). URL http://dx.doi.org/10.1103/PhysRevLett.86.2926.

[19] D. H. J. O'Dell, S. Giovanazzi und G. Kurizki, *Rotons in Gaseous Bose-Einstein Condensates Irradiated by a Laser*, Phys. Rev. Lett., **90**, 110402 (2003). URL http://dx.doi.org/10.1103/PhysRevLett.90.110402.

[20] L. Santos, G. V. Shlyapnikov und M. Lewenstein, *Roton-Maxon Spectrum and Stability of Trapped Dipolar Bose-Einstein Condensates*, Phys. Rev. Lett., **90**, 250403 (2003). URL http://dx.doi.org/10.1103/PhysRevLett.90.250403.

[21] P. B. Blakie, D. Baillie und R. N. Bisset, *Roton spectroscopy in a harmonically trapped dipolar Bose-Einstein condensate*, Phys. Rev. A, **86**, 021604 (2012). URL http://dx.doi.org/10.1103/PhysRevA.86.021604.

[22] L. Chomaz, R. van Bijnen, D. Petter, G. Faranoi, J. Becher, M. Mark, F. Wächtler, L. Santos und F. Ferlaino, *Observation of roton mode population in a dipolar quantum gas*, Nature physics, **14**(5), 442 (2018).

[23] D. Petter, G. Natale, R. M. W. van Bijnen, A. Patscheider, M. J. Mark, L. Chomaz und F. Ferlaino, *Probing the Roton Excitation Spectrum of a Stable Dipolar Bose Gas*, Phys. Rev. Lett., **122**, 183401 (2019). URL http://dx.doi.org/10.1103/PhysRevLett.122.183401.

[24] J.-N. Schmidt, J. Hertkorn, M. Guo, F. Böttcher, M. Schmidt, K. S. H. Ng, S. D. Graham, T. Langen, M. Zwierlein und T. Pfau, *Roton Excitations in an Oblate Dipolar Quantum Gas*, Phys. Rev. Lett., **126**, 193002 (2021). URL http://dx.doi.org/10.1103/PhysRevLett.126.193002.

[25] H. Kadau, M. Schmitt, M. Wenzel, C. Wink, T. Maier, I. Ferrier-Barbut und T. Pfau, *Observing the Rosensweig instability of a quantum ferrofluid*, Nature, **530**(7589), 194 (2016).

[26] F. Wächtler und L. Santos, *Quantum filaments in dipolar Bose-Einstein condensates*, Phys. Rev. A, **93**, 061603 (2016). URL http://dx.doi.org/10.1103/PhysRevA.93.061603.

[27] H. Saito, *Path-integral Monte Carlo study on a droplet of a dipolar Bose–Einstein condensate stabilized by quantum fluctuation*, Journal of the Physical Society of Japan, **85**(5), 053001 (2016).

[28] R. N. Bisset, R. M. Wilson, D. Baillie und P. B. Blakie, *Ground-state phase diagram of a dipolar condensate with quantum fluctuations*, Phys. Rev. A, **94**, 033619 (2016). URL http://dx.doi.org/10.1103/PhysRevA.94.033619.

[29] L. Chomaz, S. Baier, D. Petter, M. Mark, F. Wächtler, L. Santos und F. Ferlaino, *Quantum-fluctuation-driven crossover from a dilute Bose-Einstein condensate to a macrodroplet in a dipolar quantum fluid*, Physical Review X, **6**(4), 041039 (2016).

[30] M. Schmitt, M. Wenzel, F. Böttcher, I. Ferrier-Barbut und T. Pfau, *Self-bound droplets of a dilute magnetic quantum liquid*, Nature, **539**(7628), 259 (2016).

[31] L. Tanzi, E. Lucioni, F. Famà, J. Catani, A. Fioretti, C. Gabbanini, R. N. Bisset, L. Santos und G. Modugno, *Observation of a dipolar quantum gas with metastable supersolid properties*, Physical review letters, **122**(13), 130405 (2019).

[32] F. Böttcher, J.-N. Schmidt, M. Wenzel, J. Hertkorn, M. Guo, T. Langen und T. Pfau, *Transient supersolid properties in an array of dipolar quantum droplets*, Physical Review X, **9**(1), 011051 (2019).

[33] L. Chomaz, D. Petter, P. Ilzhöfer et al., *Long-lived and transient supersolid behaviors in dipolar quantum gases*, Physical Review X, **9**(2), 021012 (2019).

[34] K. Pawłowski und K. Rzążewski, *Dipolar dark solitons*, New Journal of Physics, **17**(10), 105006 (2015). URL http://dx.doi.org/10.1088/1367-2630/17/10/105006.

[35] T. Bland, M. J. Edmonds, N. P. Proukakis, A. M. Martin, D. H. J. O'Dell und N. G. Parker, *Controllable nonlocal interactions between dark solitons in dipolar condensates*, Phys. Rev. A, **92**, 063601 (2015). URL http://dx.doi.org/10.1103/PhysRevA.92.063601.

[36] K. Łakomy, R. Nath und L. Santos, *Soliton molecules in dipolar Bose-Einstein condensates*, Phys. Rev. A, **86**, 013610 (2012). URL http://dx.doi.org/10.1103/PhysRevA.86.013610.

[37] B. B. Baizakov, S. M. Al-Marzoug, U. A. Khawaja und H. Bahlouli, *Weakly bound solitons and two-soliton molecules in dipolar Bose–Einstein condensates*, Journal of Physics B: Atomic, Molecular and Optical Physics, **52**(9), 095301 (2019). URL http://dx.doi.org/10.1088/1361-6455/ab0e1b.

[38] M. H. Anderson, J. R. Ensher, M. R. Matthews, C. E. Wieman und E. A. Cornell, *Observation of Bose-Einstein Condensation in a Dilute Atomic Vapor*, Science, **269**(5221), 198 (1995). https://www.science.org/doi/pdf/10.1126/science.269.5221.198, URL http://dx.doi.org/10.1126/science.269.5221.198.

[39] K. B. Davis, M. O. Mewes, M. R. Andrews, N. J. van Druten, D. S. Durfee, D. M. Kurn und W. Ketterle, *Bose-Einstein Condensation in a Gas of Sodium Atoms*, Phys. Rev. Lett., **75**, 3969 (1995). URL http://dx.doi.org/10.1103/PhysRevLett.75.3969.

[40] C. J. Myatt, E. A. Burt, R. W. Ghrist, E. A. Cornell und C. E. Wieman, *Production of Two Overlapping Bose-Einstein Condensates by Sympathetic Cooling*, Phys. Rev. Lett., **78**, 586 (1997). URL http://dx.doi.org/10.1103/PhysRevLett.78.586.

[41] G. Modugno, M. Modugno, F. Riboli, G. Roati und M. Inguscio, *Two Atomic Species Superfluid*, Phys. Rev. Lett., **89**, 190404 (2002). URL http://dx.doi.org/10.1103/PhysRevLett.89.190404.

[42] M. W. Mancini, G. D. Telles, A. R. L. Caires, V. S. Bagnato und L. G. Marcassa, *Observation of Ultracold Ground-State Heteronuclear Molecules*, Phys. Rev. Lett., **92**, 133203 (2004). URL http://dx.doi.org/10.1103/PhysRevLett.92.133203.

[43] D. S. Hall, M. R. Matthews, J. R. Ensher, C. E. Wieman und E. A. Cornell, *Dynamics of Component Separation in a Binary Mixture of Bose-Einstein Condensates*, Phys. Rev. Lett., **81**, 1539 (1998). URL http://dx.doi.org/10.1103/PhysRevLett.81.1539.

[44] M. Modugno, F. Ferlaino, F. Riboli, G. Roati, G. Modugno und M. Inguscio, *Mean-field analysis of the stability of a K-Rb Fermi-Bose mixture*, Phys. Rev. A, **68**, 043626 (2003). URL http://dx.doi.org/10.1103/PhysRevA.68.043626.

[45] K. L. Lee, N. B. Jørgensen, I.-K. Liu, L. Wacker, J. J. Arlt und N. P. Proukakis, *Phase separation and dynamics of two-component Bose-Einstein condensates*, Phys. Rev. A, **94**, 013602 (2016). URL http://dx.doi.org/10.1103/PhysRevA.94.013602.

[46] J. Ruostekoski und J. R. Anglin, *Creating Vortex Rings and Three-Dimensional Skyrmions in Bose-Einstein Condensates*, Phys. Rev. Lett., **86**, 3934 (2001). URL http://dx.doi.org/10.1103/PhysRevLett.86.3934.

[47] D. S. Dantas, A. R. P. Lima, A. Chaves, C. A. S. Almeida, G. A. Farias und M. V. Milošević, *Bound vortex states and exotic lattices in multicomponent Bose-Einstein condensates: The role of vortex-vortex interaction*, Phys. Rev. A, **91**, 023630 (2015). URL http://dx.doi.org/10.1103/PhysRevA.91.023630.

[48] I. Danaila, M. A. Khamehchi, V. Gokhroo, P. Engels und P. G. Kevrekidis, *Vector dark-antidark solitary waves in multicomponent Bose-Einstein condensates*, Phys. Rev. A, **94**, 053617 (2016). URL http://dx.doi.org/10.1103/PhysRevA.94.053617.

[49] C. Qu, L. P. Pitaevskii und S. Stringari, *Magnetic Solitons in a Binary Bose-Einstein Condensate*, Phys. Rev. Lett., **116**, 160402 (2016). URL http://dx.doi.org/10.1103/PhysRevLett.116.160402.

[50] E. G. Charalampidis, W. Wang, P. G. Kevrekidis, D. J. Frantzeskakis und J. Cuevas-Maraver, *SO(2)-induced breathing patterns in multicomponent Bose-Einstein condensates*, Phys. Rev. A, **93**, 063623 (2016). URL http://dx.doi.org/10.1103/PhysRevA.93.063623.

[51] P. Öhberg und L. Santos, *Dark Solitons in a Two-Component Bose-Einstein Condensate*, Phys. Rev. Lett., **86**, 2918 (2001). URL http://dx.doi.org/10.1103/PhysRevLett.86.2918.

[52] G. C. Katsimiga, S. I. Mistakidis, T. M. Bersano, M. K. H. Ome, S. M. Mossman, K. Mukherjee, P. Schmelcher, P. Engels und P. G. Kevrekidis, *Observation and analysis of multiple dark-antidark solitons in two-component Bose-Einstein condensates*, Phys. Rev. A, **102**, 023301 (2020). URL http://dx.doi.org/10.1103/PhysRevA.102.023301.

[53] K. Fujimoto, R. Hamazaki und M. Ueda, *Flemish Strings of Magnetic Solitons and a Nonthermal Fixed Point in a One-Dimensional Antiferromagnetic Spin-1 Bose Gas*, Phys. Rev. Lett., **122**, 173001 (2019). URL http://dx.doi.org/10.1103/PhysRevLett.122.173001.

[54] C. Becker, S. Stellmer, P. Soltan-Panahi, S. Dörscher, M. Baumert, E.-M. Richter, J. Kronjäger, K. Bongs und K. Sengstock, *Oscillations and interactions of dark and dark–bright solitons in Bose–Einstein condensates*, Nature Physics, **4**(6), 496 (2008). URL http://dx.doi.org/10.1038/nphys962.

[55] M. A. Hoefer, J. J. Chang, C. Hamner und P. Engels, *Dark-dark solitons and modulational instability in miscible two-component Bose-Einstein condensates*, Phys. Rev. A, **84**, 041605 (2011). URL http://dx.doi.org/10.1103/PhysRevA.84.041605.

[56] D. Yan, J. Chang, C. Hamner, M. Hoefer, P. G. Kevrekidis, P. Engels, V. Achilleos, D. J. Frantzeskakis und J. Cuevas, *Beating dark–dark solitons in Bose–Einstein condensates*, Journal of Physics B: Atomic, Molecular and Optical Physics, **45**(11), 115301 (2012).

[57] I. Danaila, M. A. Khamehchi, V. Gokhroo, P. Engels und P. G. Kevrekidis, *Vector dark-antidark solitary waves in multicomponent Bose-Einstein condensates*, Phys. Rev. A, **94**, 053617 (2016). URL http://dx.doi.org/10.1103/PhysRevA.94.053617.

[58] S. M. Mossman, G. C. Katsimiga, S. I. Mistakidis, A. Romero-Ros, T. M. Bersano, P. Schmelcher, P. G. Kevrekidis und P. Engels, *Observation of dense collisional soliton complexes in a two-component Bose-Einstein condensate*, Communications Physics, **7**(1), 163 (2024).

[59] A. Farolfi, D. Trypogeorgos, C. Mordini, G. Lamporesi und G. Ferrari, *Observation of Magnetic Solitons in Two-Component Bose-Einstein Condensates*, Phys. Rev. Lett., **125**, 030401 (2020). URL http://dx.doi.org/10.1103/PhysRevLett.125.030401.

[60] X. Chai, D. Lao, K. Fujimoto, R. Hamazaki, M. Ueda und C. Raman, *Magnetic Solitons in a Spin-1 Bose-Einstein Condensate*, Phys. Rev. Lett., **125**, 030402 (2020). URL http://dx.doi.org/10.1103/PhysRevLett.125.030402.

[61] S. V. Manakov, *On the theory of two-dimensional stationary self-focusing of electromagnetic waves*, Soviet Physics-JETP, **38**, 248 (1974).

[62] S. N. Bose, *Plancks Gesetz und Lichtquantenhypothese*, Zeitschrift für Physik, **26**, 178 (1924). URL http://dx.doi.org/10.1007/BF01327326.

[63] Z. Yan, *General thermal wavelength and its applications*, European Journal of Physics, **21**(6), 625 (2000). URL http://dx.doi.org/10.1088/0143-0807/21/6/314.

[64] C. C. Bradley, C. A. Sackett, J. J. Tollett und R. G. Hulet, *Evidence of Bose-Einstein Condensation in an Atomic Gas with Attractive Interactions*, Phys. Rev. Lett., **75**, 1687 (1995). URL http://dx.doi.org/10.1103/PhysRevLett.75.1687.

[65] W. D. Phillips und H. Metcalf, *Laser Deceleration of an Atomic Beam*, Phys. Rev. Lett., **48**, 596 (1982). URL http://dx.doi.org/10.1103/PhysRevLett.48.596.

[66] S. Chu, L. Hollberg, J. E. Bjorkholm, A. Cable und A. Ashkin, *Three-dimensional viscous confinement and cooling of atoms by resonance radiation pressure*, Phys. Rev. Lett., **55**, 48 (1985). URL http://dx.doi.org/10.1103/PhysRevLett.55.48.

[67] A. Aspect, J. Dalibard, A. Heidmann, C. Salomon und C. Cohen-Tannoudji, *Cooling Atoms with Stimulated Emission*, Phys. Rev. Lett., **57**, 1688 (1986). URL http://dx.doi.org/10.1103/PhysRevLett.57.1688.

[68] C. S. Adams, H. J. Lee, N. Davidson, M. Kasevich und S. Chu, *Evaporative Cooling in a Crossed Dipole Trap*, Phys. Rev. Lett., **74**, 3577 (1995). URL http://dx.doi.org/10.1103/PhysRevLett.74.3577.

[69] W. Petrich, M. H. Anderson, J. R. Ensher und E. A. Cornell, *Stable, Tightly Confining Magnetic Trap for Evaporative Cooling of Neutral Atoms*, Phys. Rev. Lett., **74**, 3352 (1995). URL http://dx.doi.org/10.1103/PhysRevLett.74.3352.

[70] K. B. Davis, M.-O. Mewes, M. A. Joffe, M. R. Andrews und W. Ketterle, *Evaporative Cooling of Sodium Atoms*, Phys. Rev. Lett., **74**, 5202 (1995). URL http://dx.doi.org/10.1103/PhysRevLett.74.5202.

[71] N. Bogoliubov, *On the theory of superfluidity*, J. Phys, **11**(1), 23 (1947). URL https://ufn.ru/pdf/jphysussr/1947/11_1/3jphysussr19471101.pdf.

[72] M. Born, *Quantenmechanik der Stoßvorgänge*, Zeitschrift für Physik, **38**, 803 (1926). URL http://dx.doi.org/10.1007/BF01397184.

[73] K. E. Strecker, G. B. Partridge, A. G. Truscott und R. G. Hulet, *Formation and propagation of matter-wave soliton trains*, Nature, **417**(6885), 150 (2002).

[74] L. Khaykovich, F. Schreck, G. Ferrari, T. Bourdel, J. Cubizolles, L. D. Carr, Y. Castin und C. Salomon, *Formation of a matter-wave bright soliton*, Science, **296**(5571), 1290 (2002).

[75] E. A. Donley, N. R. Claussen, S. L. Cornish, J. L. Roberts, E. A. Cornell und C. E. Wieman, *Dynamics of collapsing and exploding Bose–Einstein condensates*, Nature, **412**, 295 (2001). URL http://dx.doi.org/10.1038/35085500.

[76] A. L. Fetter, *Theory of a dilute low-temperature trapped Bose condensate* (1998). cond-mat/9811366, URL https://arxiv.org/abs/cond-mat/9811366.

[77] T. D. Lee, K. Huang und C. N. Yang, *Eigenvalues and Eigenfunctions of a Bose System of Hard Spheres and Its Low-Temperature Properties*, Phys. Rev., **106**, 1135 (1957). URL http://dx.doi.org/10.1103/PhysRev.106.1135.

[78] P. Emplit, J. Hamaide, F. Reynaud, C. Froehly und A. Barthelemy, *Picosecond steps and dark pulses through nonlinear single mode fibers*, Optics Communications, **62**(6), 374 (1987). URL http://dx.doi.org/https://doi.org/10.1016/0030-4018(87)90003-4.

[79] D. N. Christodoulides, S. R. Singh, M. I. Carvalho und M. Segev, *Incoherently coupled soliton pairs in biased photorefractive crystals*, Applied Physics Letters, **68**(13), 1763 (1996). https://pubs.aip.org/aip/apl/article-pdf/68/13/1763/18518011/1763_1_online.pdf, URL http://dx.doi.org/10.1063/1.116659.

[80] Y. S. Kivshar und S. K. Turitsyn, *Vector dark solitons*, Opt. Lett., **18**(5), 337 (1993). URL http://dx.doi.org/10.1364/OL.18.000337.

[81] Y. S. Kivshar, *Stable vector solitons composed of bright and dark pulses*, Opt. Lett., **17**(19), 1322 (1992). URL http://dx.doi.org/10.1364/OL.17.001322.

[82] Z. Chen, M. Segev, T. H. Coskun, D. N. Christodoulides, Y. S. Kivshar und V. V. Afanasjev, *Incoherently coupled dark–bright photorefractive solitons*, Opt. Lett., **21**(22), 1821 (1996). URL http://dx.doi.org/10.1364/OL.21.001821.

[83] E. G. Charalampidis, W. Wang, P. G. Kevrekidis, D. J. Frantzeskakis und J. Cuevas-Maraver, *SO(2)-induced breathing patterns in multicomponent Bose-Einstein condensates*, Phys. Rev. A, **93**, 063623 (2016). URL http://dx.doi.org/10.1103/PhysRevA.93.063623.

[84] W. Wang, L.-C. Zhao, E. G. Charalampidis und P. G. Kevrekidis, *Dark–dark soliton breathing patterns in multi-component Bose–Einstein condensates*, Journal of Physics B: Atomic, Molecular and Optical Physics, **54**(5), 055301 (2021).

[85] T. Busch und J. R. Anglin, *Dark-Bright Solitons in Inhomogeneous Bose-Einstein Condensates*, Phys. Rev. Lett., **87**, 010401 (2001). URL http://dx.doi.org/10.1103/PhysRevLett.87.010401.

[86] C. Qu, M. Tylutki, S. Stringari und L. P. Pitaevskii, *Magnetic solitons in Rabi-coupled Bose-Einstein condensates*, Phys. Rev. A, **95**, 033614 (2017). URL http://dx.doi.org/10.1103/PhysRevA.95.033614.

[87] D. Yan, F. Tsitoura, P. G. Kevrekidis und D. J. Frantzeskakis, *Dark-bright solitons and their lattices in atomic Bose-Einstein condensates*, Phys. Rev. A, **91**, 023619 (2015). URL http://dx.doi.org/10.1103/PhysRevA.91.023619.

[88] G. C. Katsimiga, J. Stockhofe, P. G. Kevrekidis und P. Schmelcher, *Stability and Dynamics of Dark-Bright Soliton Bound States Away from the Integrable Limit*, Applied Sciences, **7**(4) (2017). URL http://dx.doi.org/10.3390/app7040388.

[89] S. Bresolin, A. Roy, G. Ferrari, A. Recati und N. Pavloff, *Oscillating Solitons and ac Josephson Effect in Ferromagnetic Bose-Bose Mixtures*, Phys. Rev. Lett., **130**, 220403 (2023). URL http://dx.doi.org/10.1103/PhysRevLett.130.220403.

[90] K. Aikawa, A. Frisch, M. Mark, S. Baier, A. Rietzler, R. Grimm und F. Ferlaino, *Bose-Einstein Condensation of Erbium*, Phys. Rev. Lett., **108**, 210401 (2012). URL http://dx.doi.org/10.1103/PhysRevLett.108.210401.

[91] M. Lu, N. Q. Burdick, S. H. Youn und B. L. Lev, *Strongly Dipolar Bose-Einstein Condensate of Dysprosium*, Phys. Rev. Lett., **107**, 190401 (2011). URL http://dx.doi.org/10.1103/PhysRevLett.107.190401.

[92] I. Stevenson, A. Z. Lam, N. Bigagli, C. Warner, W. Yuan, S. Zhang und S. Will, *Ultracold Gas of Dipolar NaCs Ground State Molecules*, Phys. Rev. Lett., **130**, 113002 (2023). URL http://dx.doi.org/10.1103/PhysRevLett.130.113002.

[93] N. Bigagli, W. Yuan, S. Zhang, B. Bulatovic, T. Karman, I. Stevenson und S. Will, *Observation of Bose–Einstein condensation of dipolar molecules*, Nature, **631**, 289 (2024). URL http://dx.doi.org/10.1038/s41586-024-07492-z.

[94] T. Lahaye, C. Menotti, L. Santos, M. Lewenstein und T. Pfau, *The physics of dipolar bosonic quantum gases*, Reports on Progress in Physics, **72**(12), 126401 (2009). URL http://dx.doi.org/10.1088/0034-4885/72/12/126401.

[95] M. Edwards, M. Krygier, H. Seddiqi, B. Benton und C. W. Clark, *Approximate mean-field equations of motion for quasi-two-dimensional Bose-Einstein-condensate systems*, Phys. Rev. E, **86**, 056710 (2012). URL http://dx.doi.org/10.1103/PhysRevE.86.056710.

[96] L. Erdős, B. Schlein und H.-T. Yau, *Rigorous Derivation of the Gross-Pitaevskii Equation*, Phys. Rev. Lett., **98**, 040404 (2007). URL http://dx.doi.org/10.1103/PhysRevLett.98.040404.

[97] P. Pickl, *Derivation of the Time Dependent Gross-Pitaevskii Equation Without Positivity Condition on the Interaction*, Journal of Statistical Physics, **140**, 76 (2010). URL http://dx.doi.org/10.1007/s10955-010-9981-0.

[98] W. Kirkby, T. Bland, F. Ferlaino und R. N. Bisset, *Spin rotons and supersolids in binary antidipolar condensates*, SciPost Phys. Core, **6**, 084 (2023). URL http://dx.doi.org/10.21468/SciPostPhysCore.6.4.084.

[99] K. Góral und L. Santos, *Ground state and elementary excitations of single and binary Bose-Einstein condensates of trapped dipolar gases*, Phys. Rev. A, **66**, 023613 (2002). URL http://dx.doi.org/10.1103/PhysRevA.66.023613.

[100] P. B. Blakie, D. Baillie und S. Pal, *Variational theory for the ground state and collective excitations of an elongated dipolar condensate*, Communications in Theoretical Physics, **72**(8), 085501 (2020). URL http://dx.doi.org/10.1088/1572-9494/ab95fa.

[101] S. Giovanazzi und D. O'Dell, *Instabilities and the roton spectrum of a quasi-1D Bose-Einstein condensed gas with dipole-dipole interactions*, The European Physical Journal D, **31**, 439 (2004). URL http://dx.doi.org/10.1140/epjd/e2004-00146-7.

[102] S. Sinha und L. Santos, *Cold Dipolar Gases in Quasi-One-Dimensional Geometries*, Phys. Rev. Lett., **99**, 140406 (2007). URL http://dx.doi.org/10.1103/PhysRevLett.99.140406.

[103] S. Pal, D. Baillie und P. B. Blakie, *Excitations and number fluctuations in an elongated dipolar Bose-Einstein condensate*, Physical Review A, **102**(4) (2020). URL http://dx.doi.org/10.1103/physreva.102.043306.

[104] W. T. V. William H. Press, Saul A. Teukolsky und B. P. Flannery, *Numerical recipes: The art of scientific computing*, Cambridge University Press (2007). URL https://www.cambridge.org/us/universitypress/subjects/mathematics/numerical-recipes/numerical-recipes-art-scientific-computing-3rd-edition?format=HB&isbn=9780521880688.

[105] D. T. Son und M. A. Stephanov, *Domain walls of relative phase in two-component Bose-Einstein condensates*, Phys. Rev. A, **65**, 063621 (2002). URL http://dx.doi.org/10.1103/PhysRevA.65.063621.

[106] T. Bland, E. Poli, L. A. P. n. Ardila, L. Santos, F. Ferlaino und R. N. Bisset, *Alternating-domain supersolids in binary dipolar condensates*, Phys. Rev. A, **106**, 053322 (2022). URL http://dx.doi.org/10.1103/PhysRevA.106.053322.

[107] S. Li, U. N. Le und H. Saito, *Long-lifetime supersolid in a two-component dipolar Bose-Einstein condensate*, Phys. Rev. A, **105**, L061302 (2022). URL http://dx.doi.org/10.1103/PhysRevA.105.L061302.

[108] W. Kirkby, A.-C. Lee, D. Baillie, T. Bland, F. Ferlaino, P. B. Blakie und R. N. Bisset, *Excitations of a Binary Dipolar Supersolid*, Phys. Rev. Lett., **133**, 103401 (2024). URL http://dx.doi.org/10.1103/PhysRevLett.133.103401.

[109] W. H. Zurek, *Causality in Condensates: Gray Solitons as Relics of BEC Formation*, Phys. Rev. Lett., **102**, 105702 (2009). URL http://dx.doi.org/10.1103/PhysRevLett.102.105702.

[110] G. Lamporesi, S. Donadello, S. Serafini, F. Dalfovo und G. Ferrari, *Spontaneous creation of Kibble–Zurek solitons in a Bose–Einstein condensate*, Nature Physics, **9**, 656 (2013). URL http://dx.doi.org/10.1038/nphys2734.

[111] S. Donadello, S. Serafini, M. Tylutki, L. P. Pitaevskii, F. Dalfovo, G. Lamporesi und G. Ferrari, *Observation of Solitonic Vortices in Bose-Einstein Condensates*, Phys. Rev. Lett., **113**, 065302 (2014). URL http://dx.doi.org/10.1103/PhysRevLett.113.065302.